Dissertation in Astronomy

submitted to the
Combined Faculties of the Natural Sciences and Mathematics
of the Ruperto-Carola-University of Heidelberg, Germany,
for the degree of
Doctor of Natural Sciences

presented by

Yu-Yen Chang
born in Taipei, Taiwan

Oral examination: December 17th, 2013

Galaxy Shapes through Cosmic Time

– Intrinsic Structure of Early-type Galaxies at High Redshift –

Referees: Prof. Dr. Hans-Walter Rix
Prof. Dr. Eva K. Grebel

Supervisors: Prof. Dr. Hans-Walter Rix
Dr. Arjen van der Wel

Abstract

In this thesis, we measure for the first time the projected shapes of large samples of distant early-type galaxies in deep near-infrared surveys from the ground and with the Hubble Space Telescope, and reconstruct their intrinsic, three-dimensional shape distribution assuming random viewing angles. We find that the most massive early-type galaxies are roundest at all redshifts $0 < z < 2.5$, indicating that at any cosmic time mergers dominate the growth of the most massive galaxies. However, early-type galaxies were on average more disk-like at earlier times, indicating that star formation in their progenitors occurred in disks, and that merging is the dominant evolutionary channel after star formation ceases. Together with the recent finding that typical early-type galaxy sizes increase dramatically between $z \sim 2$ and the present, the increased 'roundness' suggests that classical elliptical galaxies emerge through gradual merging and accretion of satellites. Moreover, the observed increase in number density over the same time span suggests that new early-type galaxies form continuously, also at late cosmic times. Our findings suggest that these newly formed early types are generally disk-like at all redshifts, and subsequently become larger and rounder through merging. In addition, we provide a low-redshift benchmark for high-redshift galaxy studies, by deriving new stellar mass and star formation rate estimates for nearly a million galaxies drawn from Sloan Digital Sky Survey spectroscopic sample. Our novel approach combines photometry from multiple surveys that span a large range in wavelength (from 0.4 to 22 micron), and uses the latest modeling techniques to consistently incorporate the effects of extinction and emission by dust. We use these new properties to investigate the nature of the bimodality of star formation activity in the galaxy population.

Zusammenfassung

In dieser Arbeit messen wir erstmalig die projezierten Formen einer großen Auswahl von entfernten Galaxien frühen Typs, die im nahen Infraroten von bodengebundenen Teleskopen sowie vom Hubble Weltraumteleskop beobachtet wurden. Wir rekonstruieren die Verteilung der intrinsischen, dreidimensionalen Form unter Annahme eines zufälligen Abbildungswinkels. Wir finden, dass die massereichsten Galaxien frühen Typs bei allen Rotverschiebungen von $0 < z < 2{,}5$ auch die rundesten Vertreter der Gesamtpopulation sind. Das deutet darauf hin, dass Verschmelzungen von Galaxien zu allen kosmischen Zeiten das Wachstum der massereichsten Galaxien dominieren. Allerdings sind frühe Galaxientypen in ihrer jungen Evolutionsphase typischerweise flacher, was andeutet, dass Sternentstehung hauptsächlich in Scheiben stattfindet und dass die Verschmelzung von Galaxien die vorherrschende Entwicklungsform nach Ende der Sternentstehung ist. Zusammen mit der neuerlichen Entdeckung, dass die Größe von Galaxien frühen Typs sich zwischen $z \sim 2$ und heute dramatisch erhöht, deutet die erhöhte Rundheit darauf hin, dass klassische elliptische Galaxien durch schrittweise Verschmelzung und Akkretion von Satelliten entstehen. Weiterhin weist die beobachtete Erhöhung in der Anzahldichte über derselben Zeitspanne darauf hin, dass ständig neue Galaxien frühen Typs entstehen, also auch zu späten kosmischen Zeiten. Unsere Ergebnisse lassen darauf schließen, dass bei allen Rotverschiebungen diese neu entstandenen Galaxien frühen Typs hauptsächlich scheibenartig sind und durch Verschmelzungen schrittweise größer und runder werden. Zusätzlich stellen wir im Rahmen, Untersuchung von Galaxien mit geringer Rotverschiebung einen Bezugspunkt zu stark rotverschobenen Galaxien bereit, indem wir für nahezu eine Million von ihnen die Sternenmasse und Sternentstehungsrate aus einer spektroskopischen Auswahl des Katalogs vom Sloan Digital Sky Survey abschätzen. Unser neuartiges Verfahren kombiniert Photometrie, die einen großen Wellenlängenbereich abdeckt (von 0,4 bis 22 Mikrometer), und nutzt die neuesten Modellverfahren, um die Effekte der Extinktion und Emission des Staubes konsistent zu berücksichtigen. Wir verwenden diese neu ermittelten Eigenschaften, um die Bimodalität der Sternentstehungsaktivität in der Galaxienpopulation zu untersuchen.

To my Mom and Dad

Contents

1 INTRODUCTION

The story starts from the history of modern astronomy to extragalactic studies and modern cosmology. Then we proceed to the brief history of the Big Bang theory, Cosmic Microwave Background radiation and the cold dark matter model. We will start to address galaxies from the traditional classification of local galaxies, and then the internal structure of local galaxies. We will explore galaxy formation and evolution from the previous observational results, especially for the structural evolution. We will also introduce deep near-infrared surveys to provide the information we need for shape studies. Finally, a new approach to galaxy classifications and mass estimates will be introduced for lookback studies.

1.1 OUR UNIVERSE

It is natural for human beings to be curious about everything on the sky as well as in the Universe we are living. Astronomy now is a branch of natural science, but it was highly connected to religion, mystery, esoterica, politics, and philosophy in different ancient cultures. Though everyone was a potential astronomer in the past because of the cleaner sky, most of the ancient astronomers are anonymous today. Therefore, modern astronomy can only be traced back several hundred years ago. First, Nicolaus Copernicus proposed the heliocentric system in the 16th century (Copernicus 1543) and Johannes Kepler came up with laws of planetary motion in the 17th century (Kepler 1609). In the same era, Galileo Galilei used his telescope to confirm the phases of Venus, discover the four largest satellite of Jupiter, observe the ring of Saturn, and analyze sunspots (Galilei 1610, 1632). Then Isaac Newton formulated the basic laws of motion and universal gravitation (Newton 1760).

The discoveries of extragalactic objects came later. In the late 18th century, Charles Messier cataloged about 100 objects to avoid confusion with the comets he was looking for (Messier 1781). Many astronomical objects, except stars and planets, were discovered since late 19th century. For instance, the General Catalogue of Galaxies by John Herschel in 1864 (Herschel 1864), the New General Catalogue of Nebulae and Clusters of Stars (NGC) and Index Catalogues (IC) by Dreyer (1888, 1895, 1910). It was controversial whether all these objects are inside our Milky Way or some of them are "island universes" like the Milky Way. Therefore, the Great Debate invited two leading astronomers, Harlow Shapley and Heber D. Curtisto argue these two distinct ideas in 1920. Shapley assumed that the Milky Way was the entire Universe and Curtis stated that nebulae such as Andromeda were "island universes", which were close to the separate galaxies we agree upon today. At around the same time, larger telescopes were built and astronomers were able to measure the spectra and intensity of light at different wavelengths for faint objects. First, Scheiner (1899) obtained a spectrum of M31 and found a cluster of Sun-like stars. From 1912, Vesto Slipher discovered that the spectra of light of faint nebulous objects (Slipher 1913, 1915) was systematically shifted to longer wavelengths, which is known as redshift at the present. In 1922, Opik (1922) estimated the distance of M31 by the mass-to-light ratio of the central region and found a distance of 440 kpc, suggesting that it lay well outside the confines of the Milky Way. Before that, Henrietta Swan Leavitt discovered the relation between the luminosity and the period of Cepheid variables (Leavitt 1908; Leavitt & Pickering 1912) and Duncan (1922) discovered the variable stars in Spiral Nebula M33 Trianguli. In 1925, Edwin Hubble used Cepheid variables to estimated the distances to demonstrate some 'nebula' are extragalactic objects outside our Milky Way (Hubble 1925). These can be seen as the beginning of extragalactic astronomy.

Albert Einstein published his theory of general relativity in 1916 (Einstein 1916). This theory was able to construct self-consistent models for the Universe as a whole for the first time. He explored his theory and found that all the solutions require the Universe either to expand or to contract. Immediately in 1917, de Sitter (1917) derived a stable solution to Einstein's field equations for an isotropic, static, and empty expanding cosmology. From 1922 to 1927, Alexander Friedmann explored both static and expanding solutions (Friedmann 1922) and Georges Lemaître proposed the original Big Bang model from his own solutions (Lemaître 1927), which suggested an estimated value of the rate of expansion and the expanding Universe. In 1929, Edwin Hubble and Milton L. Humason showed the linear relation between the recession velocities of galaxies and the distances from observation therefore confirmed that our Universe is expanding (Hubble 1929). These discoveries opened the door to the modern cosmology.

1.2 After the Big Bang

The Big Bang model emerged around 1950s because the expending Universe implies a denser early Universe and a singular origin. In 1948, George Gamow suggested that the chemical elements may have been created by thermonuclear reactions in the early Universe (Gamow 1948). Ralph Alpher, Robert Herman, and Robert Dicke also estimated the microwave background radiation temperature around dozens of Kelvin (Alpher & Herman 1948; Dicke et al. 1946). Finally, the ~2.7K cosmic microwave background radiation (CMB) was discovered by Penzias & Wilson (1965). These established the Big Bang model as the standard model of modern cosmology.

In 1992, the anisotropy of the CMB was firstly detected by the Cosmic Background Explorer (COBE, Smoot et al. 1992). It implies that the CMB is an almost perfect black body spectrum and has tiny temperature fluctuations as shown in Figure 1.1. The discoveries of accelerating expansion from Type Ia supernovae in 1998 (Riess et al. 1998; Perlmutter et al. 1999), and the following CMB measurements, such as the BOOMERanG microwave background experiment (de Bernardis et al. 2000) and the Wilkinson Microwave Anisotropy Probe (WMAP Bennett et al. 2003; Hinshaw et al. 2009), gave the evidence that the Universe is flat and made the ΛCDM (cold dark matter model with dark energy) model generally accepted. The observational results also implies that the Universe is consistent with about 4% baryon matter, 23% dark matter, and 73% dark energy, and the anisotropy of the CMB shows the small perturbations to make structural formation in our Universe.

As mentioned above, in the standard model of modern cosmology, the Universe is almost spatially homogeneous and isotropic, and structures, such as galaxies, form from small initial perturbations. In fact, there was evidence before the CMB observations that

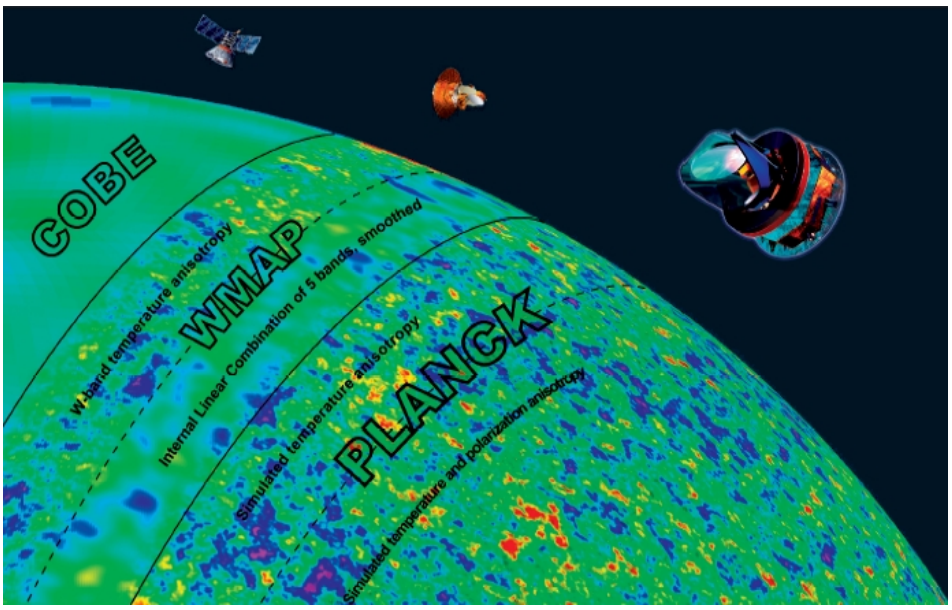

FIGURE 1.1: *The Cosmic Microwave Background Radiation (CMB) measured by the COBE, WMAP and Planck satellite experiments. The resolutions are about 7 degrees, 15 arcminutes, and 5 arcminutes, respectively. The latest Plank results are published during the thesis writing period. They provide the essential information on primary CMB temperature anisotropies, which can be seen as the baby pictures of our Universe. Credit: NASA / ESA. composite.*

galaxies and groups of galaxies are situated in the center of dark matter halo (Zwicky 1933; Bosma 1978; Rubin et al. 1978, 1980, 1985). The observations of rotation curves of spiral galaxies motivated White & Rees (1978) propose a two-stage galaxy formation for dark halos and luminous content of galaxies. First, the dark halos form from hierarchical merging (Press & Schechter 1974). Then the cooling and condensation of gas at the center of the potential wells of the dark matter halos produces the stars. Fall & Efstathiou (1980) developed a model of disk formation in dark matter halos with angular momentum. Energy is lost while the gas cool down in the center of the dark matter halo. Stars form and rotate in a disk to keep the conservation of angular momentum. However, disks can also be destroyed by hierarchical merging due to gravitational effects and form spheroids.

1.3 FROM LOCAL GALAXIES

Galaxies are dynamically bound and self-clustered systems containing stars, gas, dust, and dark matter, and can be seen as the basic component of our Universe. Therefore, galaxy formation and evolution is one of the most important ways to understand the

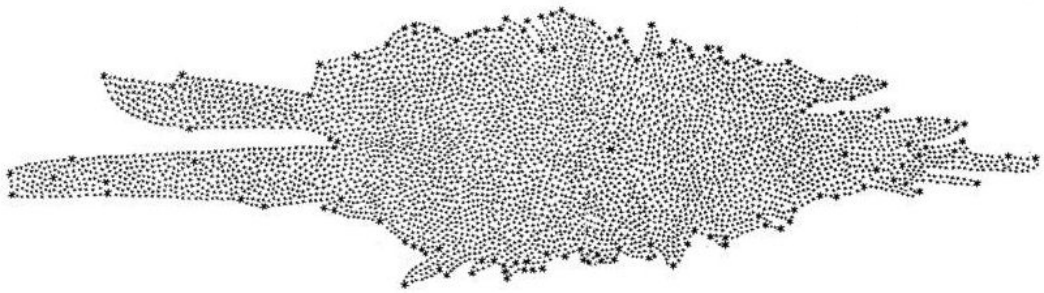

Figure 1.2: *William Herschel's model of the Milky Way. He observed the stars and concluded the shape of the Milky Way was like a flattened grindstone (Herschel 1785). He measured the distances by assuming that all stars are equally bright, and found that most of the stars are located in a circular band, suggesting that we were located in a disk-like plane in the Milky Way and the thickness of the disk was about one-tenth its diameter. The assumptions of the equal brightness of stars and the results of his distances were incorrect but the flattened shape is close to today's observation.*

history of the Universe. In general, galaxies can be classified by two types: late-type and early-type galaxies. For example, our Milky Way, the first observed galaxy (Figure 1.2), is now defined as a barred spiral galaxy, making it a late-type galaxy.

The classification can be traced back to the 1930s when Edward Hubble classified galaxies into the Hubble sequence according to their morphology (Hubble 1936). This traditional classification of early-type galaxies includes ellipticals and lenticular galaxies, and late-type galaxies include spirals and irregulars as shown in Figure 1.3. Briefly speaking, elliptical galaxies (E) are galaxies that have nearly elliptical isophotes without clearly defined structure. Hubble defined different ellipticals with an integer number followed by E from their ellipticities (ellipticity=1-projected axis ratio). Lenticular galaxies (S0) are a transition between ellipticals and spirals. They contain a bulge and a large enveloping region of relatively unstructured brightness which often appears like a disk without spiral arms. Spiral galaxies (S) are disks with spiral arm structure and a central bulge. They are divided between normal spirals (S) and barred spirals (SB). The bulge to disk ratios also classify the sequence denoted by a, b, c... from bulge dominant to disk dominant. Irregular galaxies (Irr) are galaxies with weak or no regular structure. Besides, there are other extended and revised classifications (e.g., de Vaucouleurs 1959, 1974; Kormendy 1979; Kormendy & Bender 1996) to classify galaxies by the detailed structures of bulges, disks, bars, spiral arms, rings, and lens. Even though morphological classifications are subjective and dependent on the orientation and distance of the galaxies, many intrinsic properties, such as luminosity, age and gas content, correlate strongly with morphological type. Therefore, the Hubble sequence and the extended classification is widely used until today.

In this thesis, we will focus on early-type galaxies, which have smooth elliptical isophotes

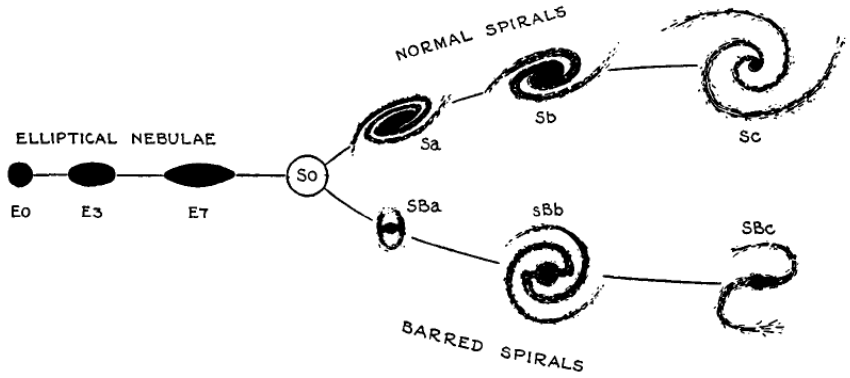

FIGURE 1.3: *The famous Hubble classification (Hubble 1936) of galaxies, which was categorized as nebula in the past and classified by projected shape in this diagram. Roughly speaking, the ellipticals (E) and lenticular (S0) galaxies are early-type galaxies and spirals (S/SB) and irregular galaxies are late-type galaxies.*

with low star-forming activities. They contain relatively old stars and are believed to be settled-down without further star formation. From the disk formation and merging theory, we know that stars form in disks and merging destroys disks. The former process can produce flat disk galaxies while the latter can produce rounder spheroidal galaxies. Therefore, a group of flat early-type galaxies implies that stars formed in the disks and merging seldom occurred until the stars in disks become older. In contrast, a group of round early-type galaxies implies that most of the disk structures are destroyed by merging while the stars get older. As a result, we can understand how important these two activities are in different groups, environments, and epochs by understanding the shapes of early-type galaxies and their fractions.

1.4 INTERNAL STRUCTURES OF LOCAL GALAXIES

In this thesis, the projected axis ratio q is the key parameter to describe and reconstruct the intrinsic shape and internal structures of early-type galaxies. It is defined by:

$$q = \frac{b}{a}, \tag{1.1}$$

where b is the semi-minor axis and a is the semi-major axis.

Besides the projected axis ratio, most of the surface brightness profile of galaxies can

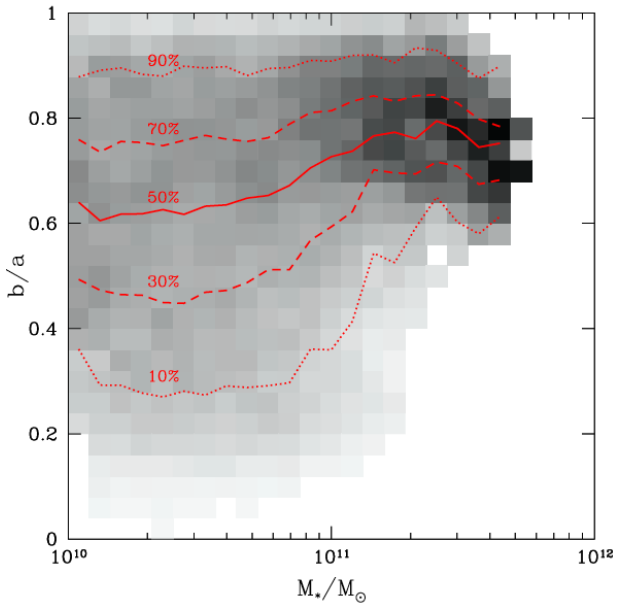

Figure 1.4: *The projected axis ratio v.s. stellar mass plots of* $0.04 < z < 0.08$ *early-type galaxies (van der Wel et al. 2009b). The distribution of low mass (*$M_* < 10^{11} M_\odot$*) early-type galaxies are broad, which indicates a oblate-like intrinsic shape. And the massive (*$M_* > 2 \times 10^{11} M_\odot$*) early-type galaxies are rounder, which implies a triaxial-like intrinsic shape.*

be well fit by the Sérsic profile (Sérsic, 1968):

$$I(R) = I_0 \exp\left[-\beta_n \left(\frac{R}{R_e}\right)^{1/n} \right], \tag{1.2}$$

where I_0 is the central surface brightness, R_e is the effective radius that encloses half of the total light, n is the Sérsic index which sets the concentration of the profile, and β_n is approximated by $\beta_n = 2n - 0.324$ for $n \gtrsim 1$. In general, the Sérsic index is higher for early-type galaxies ($n = 4$ is the de Vaucouleurs profile that applies to giant elliptical galaxies) and lower for late-type galaxies ($n = 1$ is the exponential profile that applies to spiral galaxies). In our local Universe, high-mass (brighter) early-type galaxies are more concentrated and have higher Sérsic indices than low-mass (fainter) early-type galaxies (Caon et al. 1993; Graham et al. 2003; Trujillo et al. 2004). In this thesis, we fit the galaxy images with a Sérsic profile and measure the best-fit n, R_e, and the projected axis ratio q, for each individual galaxy.

In fact, the internal structures of galaxies in our local Universe have been discussed for several decades. The projected axis ratio distribution derived from large samples can reconstruct the internal structures of galaxies by assuming random viewing angles. The first assumption was axisymmetric structures, that is, simple oblate and prolate shapes (Hubble 1926; Sandage et al. 1970; Binney 1978; Fall & Frenk 1983). Then the

projection and deprojection of triaxial shapes (Stark 1977; Binney 1985; Franx et al. 1991) was considered to explain that local early-type galaxies are not axisymmetric (pure oblate or prolate) (Lambas et al. 1992; Padilla & Strauss 2008). For local spirals, it is clear that the disks are generally elliptical rather than circular (Ryden 2004; Unterborn & Ryden 2008). For elliptical galaxies, the non-axisymmetric intrinsic shape is proved by both projection (Ryden 1992) and deprojection (Tremblay & Merritt 1995).

Tremblay & Merritt (1996) showed that the projected axis ratio distribution of early-type galaxies is accurately described by a two-population model which consists of an oblate and a triaxial set of galaxies. Vincent & Ryden (2005) also found that bright galaxies are more triaxial-like (non-axisymmetric) and faint galaxies are more axisymmetric. The two-population model is not a mathematically unique solution, but a physically plausible one, in line with the kinematic distinction of 'fast rotators' and 'slow rotators' (e.g., Emsellem et al. 2011). In addition, van der Wel et al. (2009b) use the projected axis ratio from the Sloan Digital Sky Survey (SDSS) to study the intrinsic distribution of early-type galaxies as shown in Figure 1.4. They found that the projected axis ratios of massive ($M_* > 2 \times 10^{11} M_\odot$) early-type galaxies are essentially all larger than 0.6, implying that they must be intrinsically round and that merging produced such large ellipticals. Moreover, they showed a broad distribution of projected axis ratio for low mass ($M_* < 10^{11} M_\odot$) early-type galaxies, implying a mix of bulge- and disk- dominated galaxies. Accordingly, disk-like early-type galaxies have a ceiling mass of $M_* \sim 2 \times 10^{11} M_\odot$, above which essentially all early-type galaxies are intrinsically round.

1.5 Internal Structural Evolution of Early-Type Galaxies

At high redshift, it is still unclear whether the most massive early-type galaxies are always round, as in our local Universe. If so, there is a universal mass limit to build disk galaxies and all the massive ellipticals above $M_* \sim 10^{11} M_\odot$ are built from hierarchical merging processes. Holden et al. (2009) used a sample of early-type galaxies in very massive clusters from $0 < z < 1.3$ and found no evolution in the overall ellipticity, suggesting that the intrinsic shapes of cluster early-type galaxies do not evolve from $z \sim 1$ to $z = 0$. But the shape evolution of massive early-type galaxies is still unknown in the fields and at higher redshifts. Recently, van der Wel et al. (2011) shows a large fraction of 14 massive $1.5 < z < 2$ galaxies, which are not in clusters, are flat in projection. This provided a tentative hint that many massive early-type galaxies are disk dominated at $z > 1$, suggesting that gas had time to settle into a disk before the star forming activities cease. However, the sample sizes were too small to compare with local galaxies to answer whether the evolution occurred, and there were not enough of

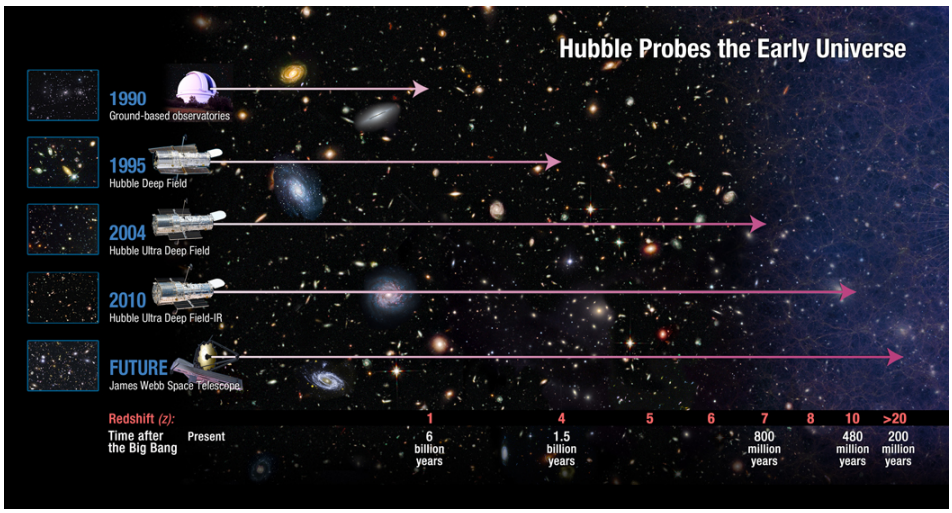

FIGURE 1.5: *The cosmic epochs of our Universe, which can be probed by ground-based and space-based telescopes. From $z \sim 10$ to the present, galaxy evolution and formation is one of the most important way to decode our Universe. Because merging was active around $z \sim 2$, most of the massive early-type galaxies in the present day were formed since $z \sim 2$, which is in the middle of this figure. The observational results also show that massive early-type galaxies are getting more common, bigger, and rounder. Credit: NASA, ESA, and A. Feild (STScI).*

the most massive early-type galaxies in the sample to see whether there is universal mass limit for disk formation.

Considering the shape studies of massive early-type galaxies in massive clusters to $z \sim 1$ and the small sample at $z \sim 2$, it is possible that massive early-galaxies have not evolved at all in both clusters and in the field from $z \sim 2$, and the 14 galaxies from van der Wel et al. (2011) are just part of a broad population as we see at low redshift. Alternatively, galaxy shapes might have evolved, but only in the field and not in clusters. Or shape evolution only occurred at $z > 1$ so we can not see any evolution between $0 < z < 1$ in any environment. If massive early-type galaxies at $z > 1$ are indeed flatter than in the local Universe, it is possible that early-type galaxies since $z \sim 2$ were getting rounder through merging, which is also invoked to explain the evolving sizes of early-type galaxies (van Dokkum et al. 2008; van der Wel et al. 2008).

In this thesis, we will use $z > 1$ samples which are more than an order of magnitude larger than before. The larger sample can clarify the above problems and answer the following questions: Were the most massive early-type galaxies always the roundest as in the local Universe? Is the ceiling mass of disk-like early-type galaxies universal, or do the most massive galaxies need a long time to form and be round because of hierarchical structure growth? Is there shape evolution of early-type galaxies and at what redshift did it occur? How does such evolution depend on galaxy masses, and is the evolution driven

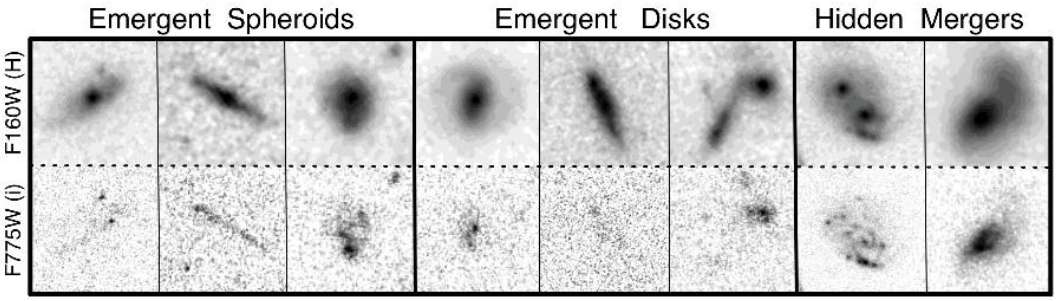

FIGURE 1.6: *Comparison of optical (lower; 4-orbit; ACS/F775W) and near-infrared (upper; 2-orbit; WFC3/F160W) images of distinct galaxies in Hubble Ultra Deep Field. The near infrared images reveal the true stellar information and the structures. Credit: CANDELS team.*

by the emergence of additional flat or round galaxies? Will the respective implications profoundly improve or change our insights into the formation of early-type galaxies? Do early-type galaxies at $z < 2.5$ mostly form due to the transition of disk galaxies from actively star forming to quiescent, or does it require the destruction pre-existing disks?

1.6 DEEP NEAR-INFRARED SURVEYS

To acquire a large population of early-type galaxies and investigate their structural evolution over cosmic time as shown in Figure 1.5, we need wide-area high-resolution imaging at high redshift. For this purpose, the rest-frame UV imaging, which is observed in the optical bands at $z \sim 2$, can not be the tracer of old stellar populations: at $z > 1$, galaxies are often faint in the UV. As shown in Figure 1.6, the optical (rest-frame UV) images in the lower row are biased by young stars and dust extinction, and the infrared (rest-frame optical) images in the upper rows can reveal the structures of galaxy in details at high redshift. Therefore, we need near-infrared imaging at $z \sim 2$ ($500\,nm \times (1+z) \sim 1.5\,\mu$m; J-band: 1.1-1.4 μm, H-band: 1.5-1.8 μm, and K-band: 2.0-2.4 μm) which provides rest-frame optical imaging at high redshift. We also need deep and high resolution data that can resolve high-redshift galaxies. In addition, the accurate statistical properties should be based on many galaxies, which means wide imaging. We introduce two deep, wide-area, high-resolution and near-infrared data sets in this thesis from ground-based and space-based telescopes, respectively.

First, the high-resolution ground-based Very Large Telescope (see Figure 1.7) / High Acuity Wide field K-band Imager (VLT/HAWK-I) provides deep near-infrared data in the full extended Chandra Deep Field South (ECDFS) [1]. The spatial resolution is about 0.5 *arcsec*, the area is about 30'×30', and the 5-σ depth is about 24.3 magnitude. This

[1] ESO program ID: 082.A-0890

Figure 1.7: *The ground-base Very Large Telescope (VLT). The four main VLT units can be seen, as well the four auxiliary telescopes. The High Acuity Wide field K-band Imager of VLT (VLT/HAWK-I) is one of the best ground-based instruments to provides deep wide-area high-resolution near-infrared images. The Paranal platform photographed in January 2007. Credit:ESO/H.H.Heyer.*

provides us with enough massive early-type galaxies at high redshift to study the structural evolution qualitatively in Chapter 2.

The Cosmic Assembly Near-infrared Deep Extragalactic Legacy Survey (CANDELS, Grogin et al. 2011; Koekemoer et al. 2011) is a 902 orbit Hubble Space Telescope (HST, Figure 1.8) multi-cycle treasury program, using the Wide Field Camera 3 (WFC3) to obtain deep high-resolution near-infrared imaging. It contain 5 deep fields: GOODS-S, UDS, GOODS-N, COSMOS, and EGS, which are the most well-studied deep fields and have multi-wavelength information from previous surveys. The spatial resolution is about 0.2 $arcsec$, the area is about 900 $arcmin^2$, and the the 5-σ depth is about 27 magnitude. It provides near-infrared imaging to investigate the structural and morphological properties of galaxies to $z \sim 3$ quantitatively, especially the observed surface brightness distribution in two dimensions. van der Wel et al. (2012) used `GALFIT` (Peng et al. 2010a) to measure the global structural parameters of 109,533 unique, H_{F160W}-selected objects from CANDELS. The high accuracy and precision single Sérsic parametrized measurements provide a complete sample to investigate size and shape evolution to $H_{F160W} \sim 24.5$. Therefore, it provides enough number of early-type galaxies up to $z \sim 2.5$ to apply models and reconstruct intrinsic shapes, and also study faint low mass early-type galaxies in Chapter 3.

At high redshifts, it is difficult or even impossible to classify galaxies visually, which is widely applied to local galaxies as described in Section 1.3. Therefore, in our work, we prefer more practical and objective indicators, which correspond to star forming activities, rather than naked eyes to classify early-type and late-type galaxies. The star formation rates (SFR) or specific star formation rates (sSFR, SFR divided by stellar

FIGURE 1.8: *Installation of Wide Field Camera 3 by astronauts as part of servicing mission 4 (the last shuttle mission) for Hubble Space Telescope. WFC3 detectors are capable of observing at all wavelengths between 200 - 1700 nm. Credit: NASA.*

mass, M_*) provide a direct numerical value to investigate the star forming activities. We can compare the sSFR with Hubble time ($t_{H(z)}$), e.g., sSFR$< 1/3t_{H(z)}$ are classified as early-type galaxies. Alternatively, the color-color diagrams (Wuyts et al. 2007; Williams et al. 2009), which is correspond to specific star formation rates, are used to separate early-type from late-type galaxies. The 4000 Å breaks, caused by absorption by metals in the atmospheres of cooler stars and lack of hot blue (O and B) stars, shows a strong bimodality in the rest $U - V$ versus $V - J$ color-color space. Furthermore, old stellar population of passive galaxies and dust obscuration of star-forming galaxies are also well separated into two groups in the UVJ diagram as shown in Figure 1.9. This selection is essentially independent of any shape or structural parameter, such as the Sérsic index n. For example, a selection of early-type galaxies by low star-forming activities will also include flat early-type galaxies with low n. Therefore, the UVJ diagram will be the technique we use separate early-type and late-type galaxies in this thesis.

1.7 GALAXY IN THE PRESENT-DAY UNIVERSE: AN IMPROVED BENCHMARK FOR LOOKBACK STUDIES

A consistent comparison between present-day galaxies and their progenitors at high redshift is crucial for a correct interpretation of their evolution. So far, we have used stellar masses and star formation rate indicators from SDSS (Brinchmann et al. 2004). Stellar masses are based on optical SEDs and SFRs are based on optical spectra (emission

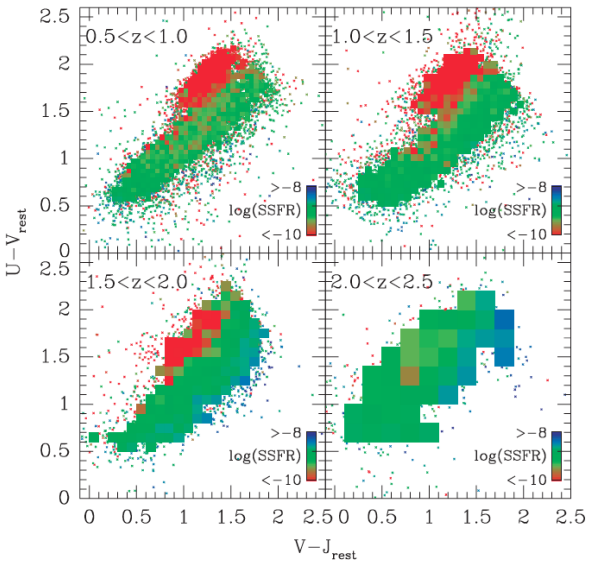

Figure 1.9: *Rest-frame UVJ diagram in four redshift bins by the median sSFR of the galaxies within each bin (Williams et al. 2009). Early-type galaxies with low sSFR are in the upper left region at all redsfhit. The separation in the UVJ diargram between early-type galaxies (red population) and late-type galaxies (green and blue population) are because of the 4000* Å *breaks of early-type galaxies and dust obscuration of late-type galaxies.*

lines). The Wide-field Infrared Survey Explorer (WISE, Wright et al. 2010) mission has provided high-quality, full-sky imaging over the wavelength range 3-22 μm, which probes stellar light in a manner that is insensitive to extinction, and thermal radiation from dust heated by star formation. Thus, we are in a position to improve our stellar mass estimates as compared to Brinchmann et al. (2004), and provide estimates of the SFR that are independent and complementary to those from the SDSS optical emission lines.

In this thesis, we will use an SDSS-selected sample, the New York University Value-Added Galaxy Catalog (NYU-VAGC, Blanton et al. 2005; Adelman-McCarthy et al. 2008; Padmanabhan et al. 2008), with the WISE and the Two Micron All Sky Survey (2MASS, Skrutskie et al. 2006) data. The NYU-VAGC catalogs contain the photometric and spectroscopic catalog data in optical (*ugriz*) and the matched 2MASS extended source catalog data in near-infrared (JHK_s). The WISE catalogs contain infrared data (W1: 3.4 μm; W2: 4.6 μm; W3: 12 μm; W4: 22 μm).

We will fit the spectral energy distribution (SED) and use Multi-wavelength Analysis of Galaxy Physical Properties (MAGPHYS, da Cunha et al. 2008) to produce a novel large catalogs of stellar masses, SFR, rest-frame colors, for local galaxies. MAGPHYS is a model package to interpret multi-wavelength observations of galaxies for galaxy physical parameters of stars and interstellar mediums in the range of 912 Å to 1 *mm*

rest-frame wavelengths. It treats the SED consistently from UV, optical, to far infrared by linking extinction and thermal infrared radiation, requiring energy balance. This will provide a state-of-the art stellar mass and SFR catalog for 100,000s of galaxies in the present-day Universe, which serves as an ideal backbone for future look-back studies. It will also provide a novel description of how SFR is distributed over galaxies of different masses, and how the fraction of passive (early-type) and star-forming (late-type) varies along the mass function.

1.8 OUTLINE OF THIS THESIS

This thesis is based on the three main project in my PhD as following:

- Chapter 2: Shape Evolution of Massive Early-type Galaxies
- Chapter 3: Structural Evolution of Early-type Galaxies
- Chapter 4: On Bimodality of the Galaxy Population

In Chapter 2, we will first focus on the shape evolution of massive early-type galaxies to high redshift in a qualitative way from VLT/HAWK-I data. We will present that 'the most massive early-type galaxies are still roundest' and 'massive early-type galaxies are flatter than local massive early-type galaxies'. The contents of this chapter are based on Chang et al. (2013a), ApJ, 769, 71, "Shape Evolution of Massive Early-Type Galaxies: Confirmation of Increased Disk Prevalence at $z > 1$".

In Chapter 3, we will then invent models of intrinsic shapes and apply these models to massive and less massive early-type galaxies in a quantitative sense to describe the structural evolution for all early-type galaxies from CANDELS. We will describe the disk-like intrinsic shape of massive early-type galaxies and rounder trend of low mass early-type galaxies at high redshift compared to local early-type galaxies by our models quantitatively. The contents of this chapter are based on Chang et al. (2013b), ApJ, 773, 149, "Structural Evolution of Early-type Galaxies to z=2.5 in CANDELS".

In Chapter 4, we will then explore the classification of early-type and late-type galaxies with the color-color diagram and demonstrate the accuracy and convenience of this classification. We will also use infrared and optical data to fit SED and compare the results with previous mass estimates.

2

Shape Evolution of Massive Early-type Galaxies

We use high-resolution K-band VLT/HAWK-I imaging over 0.25 square degrees to study the structural evolution of massive early-type galaxies since $z \sim 2$. Mass-selected samples, complete down to $\log(M/M_{\odot}) \sim 10.7$ such that 'typical' (L^*) galaxies are included at all redshifts, are drawn from pre-existing photometric redshift surveys. We then separated the samples into different redshift slices and classify them as late- or early-type galaxies on the basis of their specific star-formation rate. Axis-ratio measurements for the ~400 early-type galaxies in the redshift range $0.6 < z < 1.8$ are accurate to 0.1 or better. The projected axis-ratio distributions are then compared with lower redshift samples. We find strong evidence for evolution of the population properties: early-type galaxies at $z > 1$ are, on average, flatter than at $z < 1$ and the median projected axis ratio at a fixed mass decreases with redshift. However, we also find that at all epochs $z \lesssim 2$ the very most massive early-type galaxies ($\log(M/M_{\odot}) > 11.3$) are the roundest, with a pronounced lack among them of galaxies that are flat in projection. Merging is a plausible mechanism that can explain both results: at all epochs merging is required for early-type galaxies to grow beyond $\log(M/M_{\odot}) \sim 11.3$, and all early types over time gradually and partially loose their disk-like characteristics.

This chapter is based on Chang et al. (2013a), ApJ, 769, 71.

2.1 INTRODUCTION

In our theory of galaxy formation, the initial angular momentum, radiative energy loss of the gas, and some degree of angular momentum conservation result in gas settling into disks before most of the stars form, which makes for oblate, rotating stellar systems. Observationally, all but the most massive galaxies in the present-day universe have a disk-like structure and are rotating (Dressler 1980; Kormendy & Djorgovski 1989; Marinoni et al. 1999; Krajnović et al. 2008; Holden et al. 2009; Emsellem et al. 2011; Cheng et al. 2011).

Nonetheless, even in disk-like, rotating galaxies, many stars reside in pressure-supported bulges. Photometric decompositions indicate that in the present-day Universe 58±7% of stars are in the spheroids and 42±7% are in the disks (Benson et al. 2007). Violent mergers are thought to scramble the orbits that originally were formed and lived in disks (Toomre 1977; White & Rees 1978; Joseph & Wright 1985; Schweizer et al. 1990; Kauffmann et al. 1993; Steinmetz & Navarro 2002). This process dominates the evolution of the most massive galaxies, which do not show evidence for disks and are generally round and entirely supported by pressure instead of rotation (Jorgensen & Franx 1994; Vincent & Ryden 2005; van der Wel et al. (2009b, hereafter vdW09); Bernardi et al. 2011; Emsellem et al. 2011; Holden et al. (2012, hereafter H12)).

In this chapter we use a low specific star formation as the definition of early-type galaxy, motivated by the smooth appearance of the light profiles of galaxies with little or no young stars or (star-forming) gas. Early-type galaxies show a relatively abrupt change in their structure as a function of galaxy mass. vdW09 and H12 show that galaxies with $\log(M/M_{\odot}) < 11$ have a broad projected axis-ratio distribution, indicative of a disk-like stellar body (with typical short-to-long intrinsic axis ratio about 1:3). In contrast, early-type galaxies with $\log(M/M_{\odot}) > 11$ rarely appear highly flattened, suggesting that their formation channel destroyed any pre-existing stellar disks, with 'dry' merging between generally gas-poor progenitors as a very plausible mechanism.

Such 'dry' mergers can reconcile the relatively late, and continuous, assembly of massive early types with their old, passively evolving stellar populations. In addition, the observed small radii and high densities of early-type galaxies at redshifts $z > 1$ (e.g., van Dokkum et al. 2008; van der Wel et al. 2008) can also be explained by 'dry' merging (e.g., Khochfar & Silk 2006b; van der Wel et al. 2009a; Hopkins et al. 2010). Minor mergers are plausibly the driver of size growth, given that major mergers are less efficient in 'puffing up' galaxies (e.g., Bezanson et al. 2009), such that major merging would overproduce the number of massive galaxies in the present-day universe (e.g., McLure et al. 2013). Given the strong evidence for continuous evolution of the number of early-type galaxies (e.g., Bell et al. 2004; Faber et al. 2007) and size evolution, one may expect that their structural properties also evolve, especially if merging is invoked

as an evolutionary mechanism. To test this, H12 compared the axis-ratio distribution of a large sample of early-type galaxies at $z \sim 0.7$ with that of the local population, but found no evidence for shape evolution for masses larger than $3 \times 10^{10} M_{\odot}$. However, there could be shape evolution at higher redshifts, as major merging occurred more frequently at early epochs (e.g., Robaina et al. 2010) and the early-type galaxy number was much lower at $z > 1$ than it is today.

van der Wel et al. (2011, hereafter vdW11) showed that a good portion of a small sample of $z \sim 2$ early-type galaxies appeared flat in projection, indicative of a disk-like structure. Chevance et al. (2012) and Buitrago et al. (2013) point out that existing, samples are too small to confirm or rule out evolution in the axis ratio distribution, but they attest, based on the Sérsic index distribution, that these galaxies have more disk-like structural properties than present-day early-type galaxies. Recently, Bruce et al. (2012) used bulge-disk decompositions of massive early-type galaxies at $z > 1$ to show that many of them host pronounced disks. Whitaker et al. (2012) show a hint of an evolving axis ratio distribution of early-type galaxies out to $z \sim 1.5$, but these authors did not explore this in detail.

In this chapter we explore the (projected) shapes for a large sample (~400 objects) of early-type galaxies, selected to have masses $\log(M/M_{\odot}) > 10.7$ and low star formation rates (sSFR$< 1/3t_H(z)$, see Section 2.5.), which were drawn from a wide, high-resolution, near-infrared (K-band) imaging mosaic from VLT/HAWK-I; we investigate whether early-type galaxies at $z > 1$ show evolution in structure compared to present-day counterparts. Specifically, we will address the question whether $z > 0.8$ early-type galaxies are more or less disk-like than at the present epoch, and whether early-type galaxies at those epochs also become rounder with increasing mass, as seen today.

The structure of this chapter is as follows. In Section 2 we describe the data and select our sample of early-type galaxies. In Section 3 we analyze the projected axis-ratio distribution and its evolution since $z \sim 2$. In Section 4 we summarize our conclusions.

In this chapter, we use AB magnitudes and adopt the cosmological parameters (Ω_M,Ω_Λ,h)= (0.3, 0.7, 0.7).

2.2 DATA

The first step is to compile a catalog with photometric redshifts and stellar masses of galaxies in the extended Chandra Deep Field South (ECDFS) from MUSYC (Multi-wavelength Survey by Yale-Chile, Taylor et al. 2009; Cardamone et al. 2010). Then we use high-resolution VLT/HAWK-I K-band imaging available over essentially the full E-CDFS (ESO Program ID: 082.A-0890) to determine structural parameter (sizes, Sérsic

indices and projected axis ratios) for these galaxies. The high fidelity of these measurements, verified through the comparison with results from HST imaging, allows us to select early-type galaxies up to $z = 1.8$.

2.2.1 MULTI-WAVELENGTH DATA AND SED FITTING

MUSYC compiled observations in 32 bands, ranging from the UV to the near-infrared for the ECDFS, for which Cardamone et al. (2010) provide an optically selected catalog that we use here. We use the method and algorithms described by Wuyts et al. (2011a) to infer photometric redshifts, stellar masses and rest-frame colors. Briefly, to estimate photometric redshifts (z_{photo}) we use EAzY (Brammer et al. 2008), and to estimate stellar masses, star-formation rates, and rest-frame colors we use FAST (Kriek et al. 2009). We only include objects with significant detection of J, H and K-band imaging, and reject stars by choosing only objects with $J - K > 0.05$. We adopt the Bruzual & Charlot (2003) model, and a Chabrier (2003) stellar Initial Mass Function. A range of ages, star formation histories and extinction parameters is explored. This parent catalog contains 19642 objects.

H12 independently determined the stellar masses of early-type galaxies in the ECDFS in the redshift range $0.6 < z < 0.8$. Those mass estimates are designed to match the stellar mass estimates of present-day early-type galaxies. Since we aim to do the same we add 0.1 dex to all our stellar mass estimates to correct for the median difference between the galaxies that are included both in our parent sample and the H12 sample. This correction is likely incorrect for star-forming galaxies, but those are not considered in this work. A full investigation of the absolute mass scale for $z > 1$ is beyond the scope of this chapter.

Star formation rates (SFRs) were derived following the procedures outlined in Wuyts et al. (2011b). Briefly, the unobscured SFR traced by the UV was added to the dust-reemitted SFR inferred from FIDEL 24 μm photometry (Magnelli et al. 2009) for 24 μm-detected sources, and for sources without 24 μm detection a dust-corrected SFR was derived from stellar population modeling of the U-to-8 μm SED.

2.2.2 HIGH-RESOLUTION, NEAR-INFRARED VLT/HAWK-I IMAGING

High-resolution K-band imaging from VLT/HAWK-I, is central to our study to provide the structural parameters. We have obtained 1-hour exposures for each of 16 adjacent

tiles in a 30'×30' mosaic that covers the full ECDFS (Taylor et al. 2009), which is coincident with the HST/ACS coverage from GEMS (Galaxy Evolution from Morphologies and SEDs, Rix et al. 2004). Observation and reduction of the HAWK-I images have been performed by S. Z. using a customized pipeline based on the original version distributed by ESO. Most notably we implemented improved recipes for the construction of the master flat field and for the frame coaddition, which properly take into account object masks and variance maps. The new effective mask implementation in particular eliminates the effects of background over-subtraction which is often seen in correspondence of (bright) sources. The 5-σ point source limit is K(AB)=24.3, and the Point Spread Function (PSF) has a FWHM of 0.5" or smaller across the field. At that resolution, this ground-based K-band imaging allows us to quantify the rest-frame optical structural properties of $z > 1$ galaxies with spatial resolution that differs by no more than a factor of ~ 2 from that obtained with HST/WFC3 in the H-band (see Figure 2.1). The image quality of our data is substantially better than the ~0.6-0.7" seeing data used by Whitaker et al. (2012).

2.2.3 GALAXY STRUCTURAL PARAMETERS

TABLE 2.1: *Massive early-type galaxies:* $0.6 < z < 1.8$, $\log(M/M_{\odot}) > 10.7$ *and sSFR*$< 1/3t_H(z)$. *ID is the same as Cardamone et al. (2010). Redshift (z_{phot}) and stellar mass (M_*) are from SED fitting. K-band magnitude(K), effective radius (R_e) and projected axis ratio (q_{proj}) are from the* `GALFIT` *results. (Fulll table please see Appendix A.)*

ID	z_{phot}	M_* [$\log M_{\odot}$]	$K[mag]$	R_e	q_{proj}
4032	1.15	10.72	20.68	0.25	0.49
4213	1.11	10.73	20.25	0.35	0.83
4619	1.00	10.87	21.72	0.09	0.87
4844	1.59	10.94	20.94	0.35	0.56
5375	1.13	11.33	19.46	0.44	0.96
.	.	.	.	.	.
.	.	.	.	.	.
.	.	.	.	.	.

We use `GALAPAGOS` (Galaxy Analysis over Large Areas: Parameter Assessment by GALFITting Objects from SExtractor, Barden et al. 2012) to separately process each of the 16 HAWK-I tiles. Here we briefly describe the process as relevant for the present study. For a full description, see Barden et al. (2012). `GALAPAGOS` first constructs a catalog with `SExtractor` (Software for source extraction, Bertin & Arnouts 1996). We choose the `SExtractor` detection parameters such that the catalog is only complete

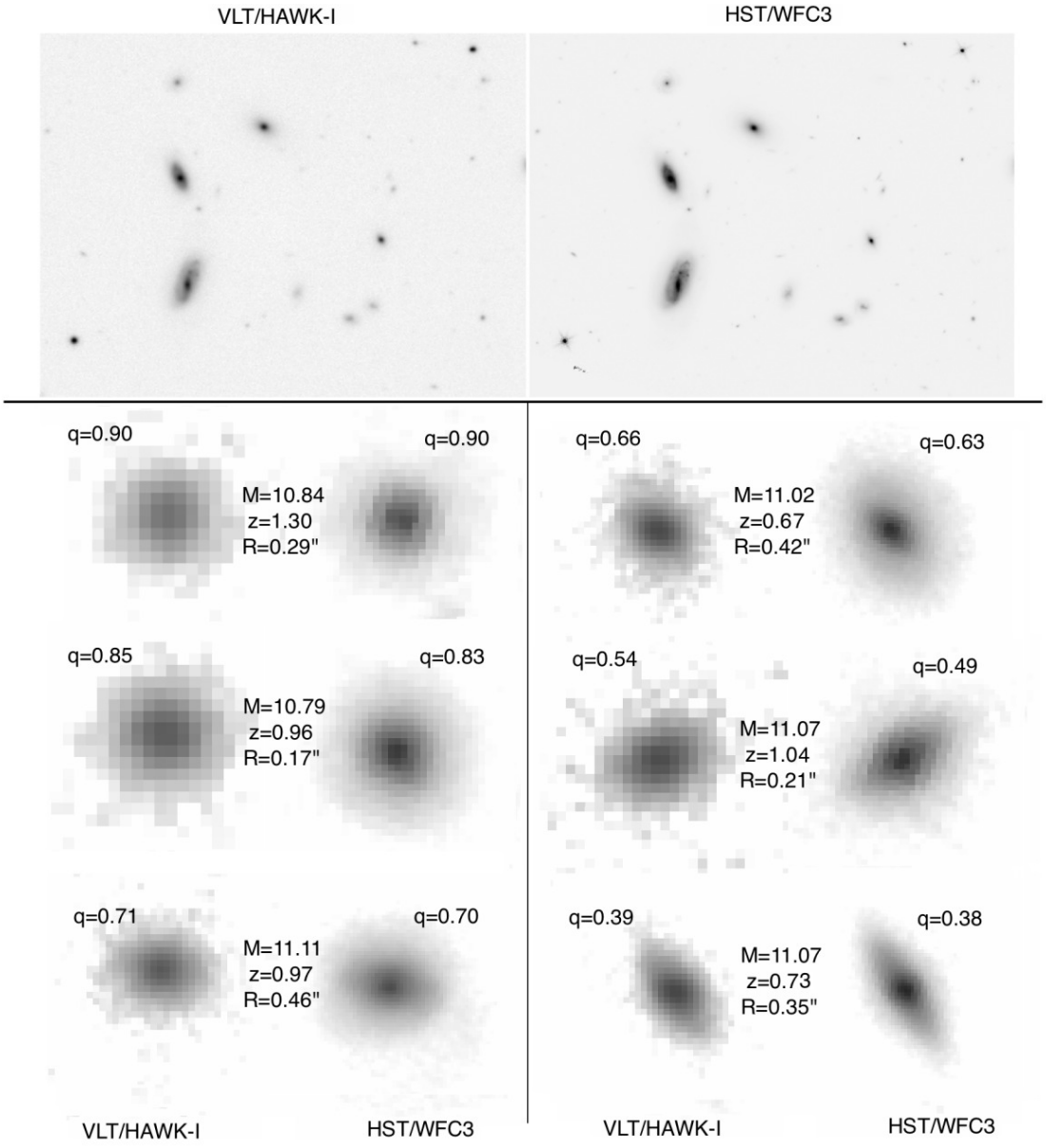

FIGURE 2.1: *Comparison between VLT/HAWK-I imaging (top left) used for the analysis in this chapter HST/WFC3 imaging (top right; Early Release Science data from Windhorst et al. 2011) of the same galaxies. The bottom panels show zoomed-in versions of the images of the HAWK-I and WFC3 images of 6 early-type galaxies in the redshift, stellar mass range of interest and circularized half-light radii of HAWK-I, as indicated. Each panel is about 2" on the side. These examples indicate that the resolution and depth of the HAWK-I imaging are sufficient to infer the projected axis ratio q, consistent with the values obtained from the WFC3 images.*

down to K(AB)=23: as we will demonstrate below this is well beyond the limit down to which structural parameters can accurately be determined. GALAPAGOS then creates image and noise cutouts for each object, including neighboring objects as necessary. The noise map is obtained from the variance map that was produced for each of the HAWK-I tiles. The background is estimated for each object by identifying a set of sky pixels that are not influenced by any of the objects in the catalog.

For each of the 16 tiles a single star is taken as the PSF, chosen among the 5 brightest, isolated stars in each tile. This choice is made after subtracting a flux-scaled version of each of those 5 stars from ∼25 stars in a tile and examining the residuals from this fit. The star that produces the cleanest residuals is selected as the PSF for that tile.

Then GALFIT (v3.0.3, Peng et al. 2002, 2010a) is called to perform the actual measurement of the structural parameters. A single Sérsic profile is fit to each target object. Neighboring objects are either masked or fit simultaneously. The free parameters in the fit are position, magnitude (m), effective radius as measured along the major axis (R_e), Sérsic index (n), axis ratio (q), and position angle. The input values of these parameters are taken from the SExtractor catalog (with the exception of n, for which 2.5 is adopted).

2.2.4 PRECISION AND ACCURACY OF AXIS-RATIO MEASUREMENTS

Our ability to determine axis ratios for distant galaxies is the limiting factor in our study. To establish the precision and accuracy of our measurements we compare the axis ratios inferred from the HAWK-I imaging with those from GEMS (Häussler et al. 2007) for galaxies in the redshift range $0.6 < z < 0.8$ (the sample from H12). The wavelength difference between GEMS (z-band) and HAWK-I (K-band) could cause intrinsic differences between axis-ratio measurements that cannot be attributed to measurement errors. For this reason, we also compare with the axis ratio estimates from objects in our sample that are contained with HST/WFC3 F160W imaging from Early Release Science (ERS) (Windhorst et al. 2011). GALAPAGOS is deployed in a similar fashion as described above – full details will be provided by van der Wel (2012, in prep.). Through the comparison with HST/ACS and HST/WFC3 (see Figure 2.2) we find that the precision of our HAWK-I axis ratio estimates is better than 10% for galaxies brighter than K(AB)=22. In addition, we see no systematic difference between HST and VLT measurements shown in Figure 2.2. The differences in the median are -0.019 and -0.025, respectively. Our axis-ratio measurements remain accurate over the entire magnitude range of our sample. In Figure 2.3 we show that, in addition, the accuracy of our axis ratio measurements does not depend on redshift.

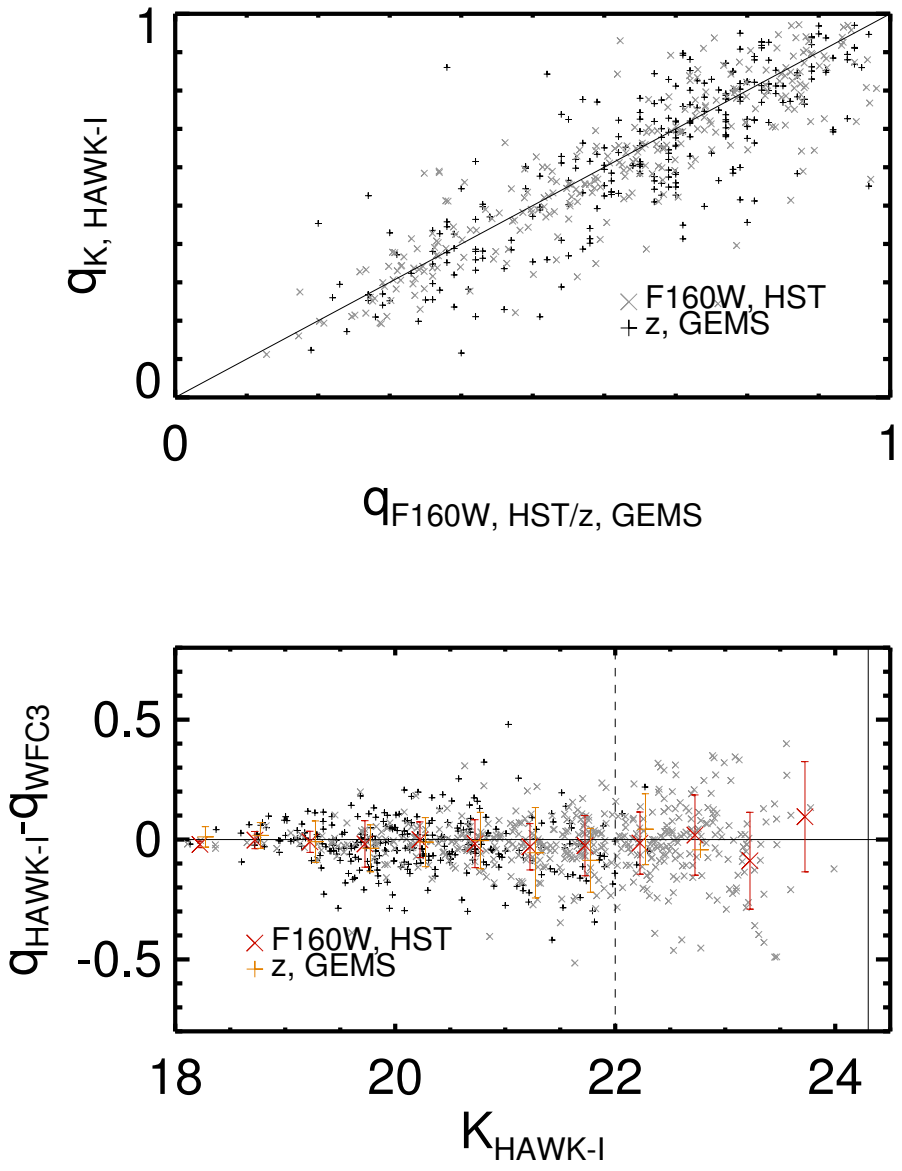

FIGURE 2.2: *Comparison of axis-ratio measurements from HAWK-I K-band and from HST imaging. The crosses represent the comparison with measurements from WFC3 F160W imaging for a HAWK-I K-band selected sample (regardless of galaxy type and redshift). The plus signs represent the comparison with measurements from HST/ACS F850LP of the H12 sample, which includes early-type galaxies in the redshift range* $0.6 < z < 0.8$*. The top panel directly compares the VLT and HST axis-ratio measurements; the bottom panel shows the difference between the VLT and HST measurements as a function of HAWK-I K-band magnitude. The red and orange bars represent the median and standard deviation for a series of magnitude bins. The standard deviation represents the measurement uncertainty in the VLT-inferred axis ratio, assuming the HST-based value as 'truth'. For galaxies, regardless of type, brighter than* $K = 22$ *the uncertainty is smaller than or equal to 0.1, and we adopt this as the magnitude limit for our study. Interestingly, the accuracy of the axis-ratio measurement is good down to at least* $K \sim 24$*: systematic effects in the axis-ratio measurements are small compared to the random uncertainty.*

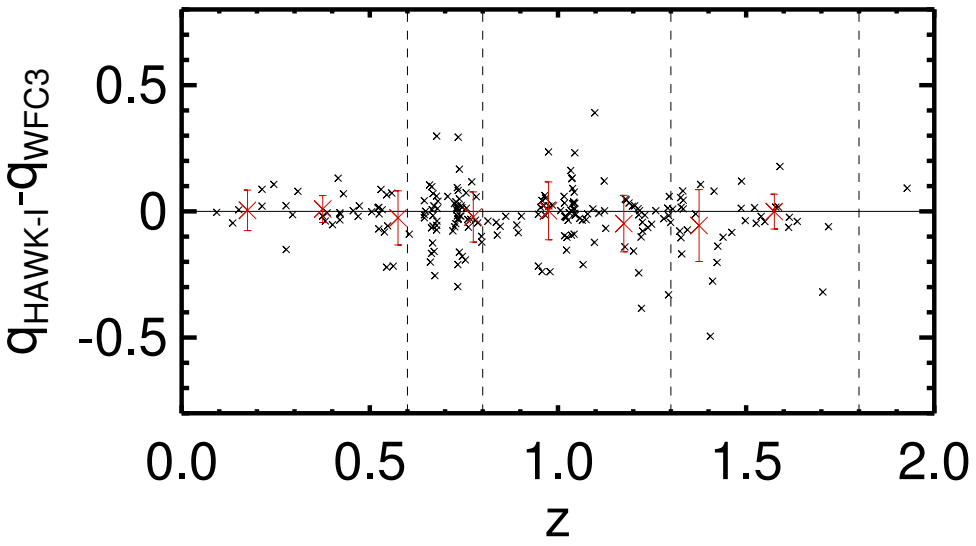

FIGURE 2.3: *Comparison of axis-ratio measurements from VLT/HAWK-I and HST/WFC3 imaging as a function of redshift. The difference in axis ratio measurements, $q_{HAWK-I} - q_{WFC3}$ has been multiplied by the total K-band flux in units of the K-band flux for a $K = 21$ object, such that variations in magnitude and their effect on the measurement uncertainty are accounted for. For galaxies in a narrow magnitude range (here, $20 < K < 22$), there is no systematic redshift dependence: the uncertainty for galaxies at $0.5 < z < 1.0$ is comparable to the uncertainty for galaxies at $z > 1$. The trends shown in Figure 2.2 and this figure imply that the accuracy of our axis ratio measurements is 10% of better for all galaxies in our sample.*

2.2.5 SAMPLE SELECTION

We match the MUSYC-based catalog (containing photometric redshifts and stellar population properties) with the HAWK-I based catalog (containing K-band magnitudes and structural parameters) by searching within apertures with radius 1". In Figure 2.4 we show the distribution of K-band magnitude as a function of stellar mass in three redshift bins. Given the magnitude limit of $K = 22$ that we adopted to ensure precise axis-ratio measurements (see above), we find that our catalog is complete down to $\log(M/M_{\odot}) = 10.7$ for all redshifts $z < 1.8$.

We select galaxies with stellar masses $\log(M/M_{\odot}) > 10.7$ and redshifts $0.6 < z < 1.8$, using spectroscopic redshifts when available, and, otherwise, photometric redshifts. We select as early-type galaxies those with specific star-formation rates (sSFR=SFR/$M_{\odot}$) smaller than $1/3t_H(z)$, where $t_H(z)$ is the Hubble time at the photometric redshift of the galaxy. This is similar to the strategy adopted by H12, who also selected their samples by star-formation activity, rather than morphological appearance.

Visual morphological classifications are not possible for the $z > 1$ galaxies in our sample as they are too faint. Automated classifiers based on, for example, concentration or Sérsic index have the problem that, by definition, they will select against disk-like objects. This motivates our choice to select early-type galaxies by their star-formation activity. This is justified further by the well-established agreement between morphological appearance and star formation activity at all redshifts $z < 1$ (e.g., Bell et al. 2004), and the correlation between structure and star formation activity that is observed to persist out to at least $z \sim 2$ (e.g., Szomoru et al. 2011; Patel et al. 2013).

In Figure 2.5 we show that our selection technique is compatible with the rest-frame UVJ selection technique that is often adopted to identify passive, early-type galaxies (e.g, Wuyts et al. 2007; Williams et al. 2009). Almost all of our low sSFR galaxies would also be identified as early-type galaxies by selecting them in this UVJ diagram. There is a substantial number of galaxies in the 'passive' UVJ color-color box that are star forming according to our direct star formation estimates fits. This number is far larger than the number of galaxies with low star formation rates that are located outside the 'passive' UVJ color box. While we include the latter in our subsequent analysis, we note that this does not affect our results. Samples selected by UVJ, star-formation rate or a combination all have have the same median axis ratio within 0.05.

In Figure 2.6 we show the correlation between rest-frame $U - V$ color and sSFR. Even in our highest redshift bin the populations of star-forming and passive galaxies separate cleanly, which implies little cross-contamination between the two types of galaxies.

Finally, we visually inspected all `GALFIT` fitting results, rejecting 10 objects with corrupted fits. The final sample consists of 394 galaxies (see Table 2.2) in the redshift

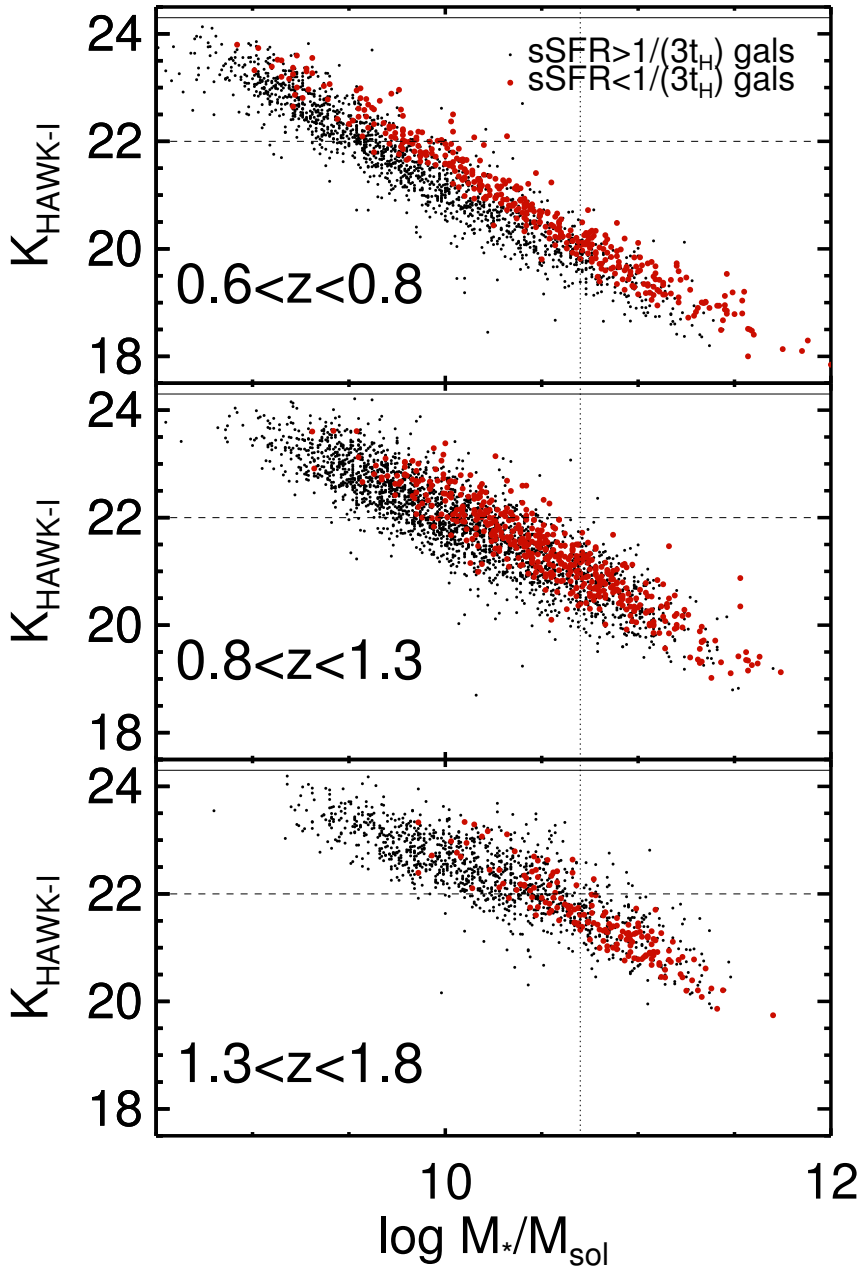

FIGURE 2.4: *HAWK-I K-band magnitude versus stellar mass in three redshift bins. Early-type galaxies, selected by their low sSFR (see Section 2.5.), are indicated by red symbols. The limiting factor in selecting our sample is set by the axis ratio estimate precision (see Figure 2.2), which sets our magnitude limit to* $K = 22$ *(the horizontal lines). The implication is that in our highest redshift bin we are complete down to a mass limit of* $\log(M/M_{\odot}) \sim 10.7$ *(the vertical lines).*

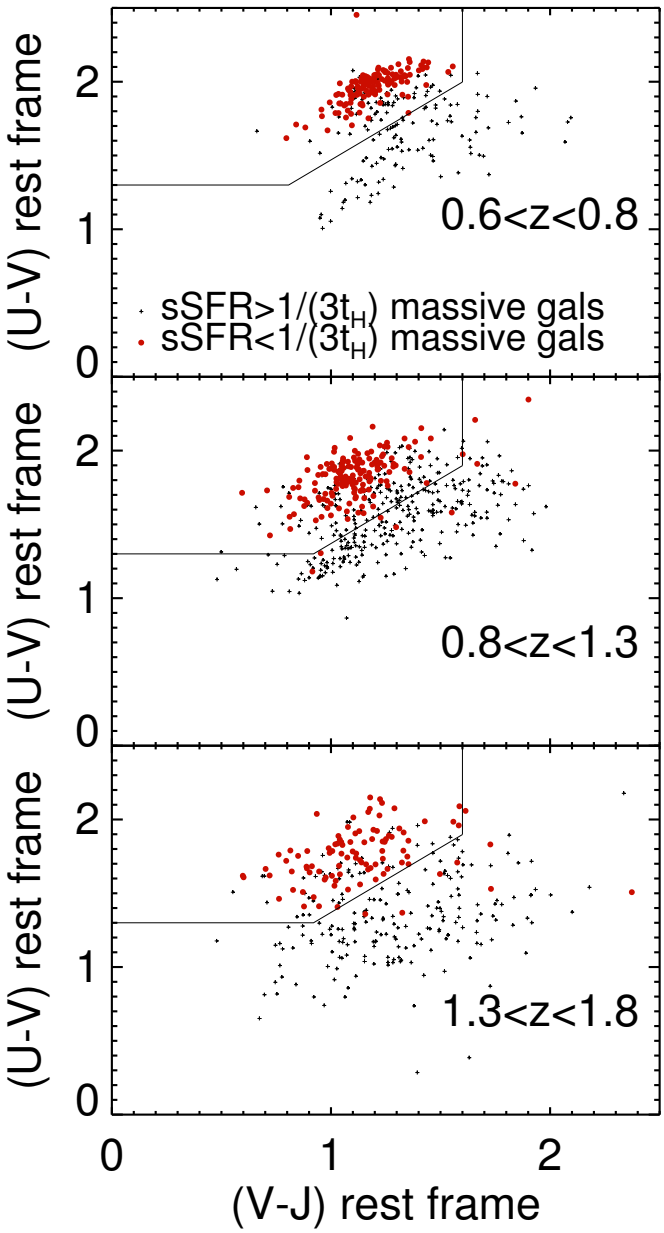

FIGURE 2.5: *Rest-frame U-V color vs. rest-frame V-J color, a diagnostic diagram to distinguish passive and star-forming galaxies. The early-type galaxies in our sample, selected by having SED-based sSFR(=SFR/M)< $1/3t_H(z)$, are indicated by red symbols. These are essentially always located in the 'passive box' as defined by Williams et al. (2009) as indicated by the polygons. That our selection criteria are conservative is indicated by the presence of a substantial number of objects with U-V and V-J colors consistent with those of passive galaxies but with sSFR larger than our limit.*

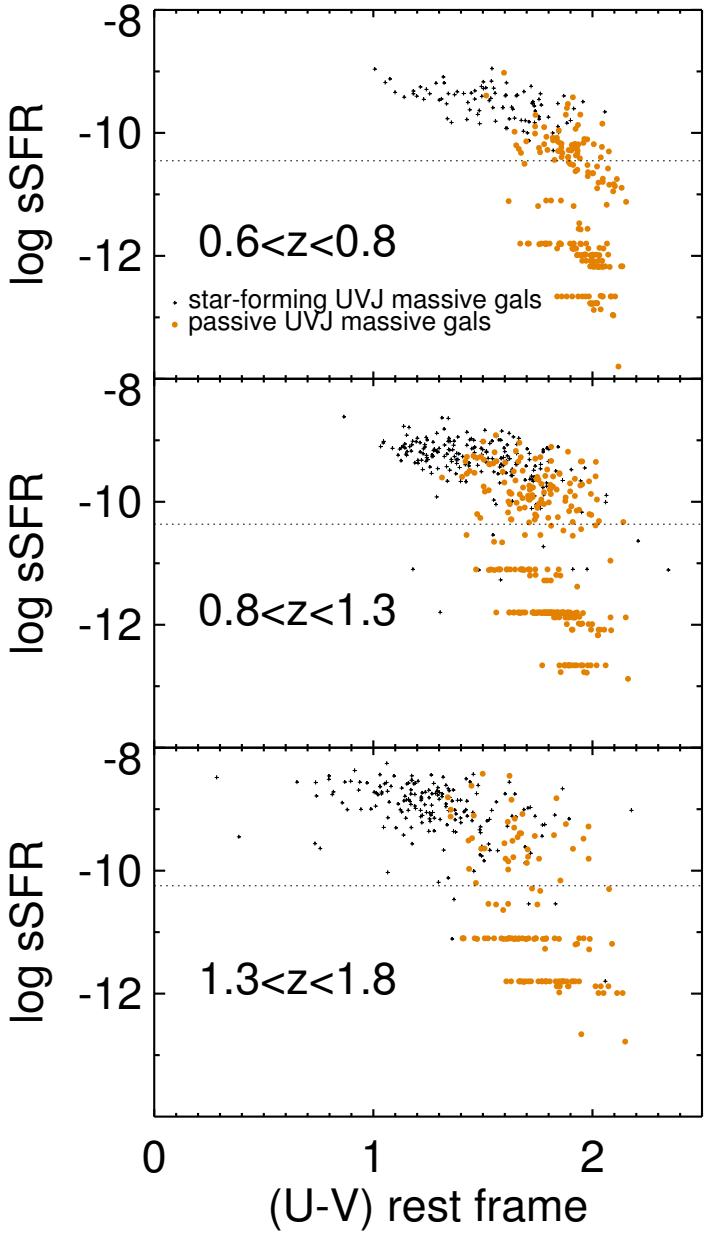

FIGURE 2.6: *The correlation between rest-frame $U-V$ color and sSFR for massive galaxies in the three redshift bins. The red symbols represent galaxies in the 'passive' UVJ color-color box (see Figure 2.5); the black symbols represent star-forming galaxies. Our selection criterion for early-type galaxies is based on a sSFR cut (sSFR$< 1/3t_H(z)$), here illustrated by the horizontal, dotted lines which correspond to the sSFR cuts in the center of the redshift bins. For all redshift bins the two types of galaxies are cleanly separated; moving the sSFR cut by a modest amount does not strongly affect our selection of early-type galaxies. Note that aliasing occurs for low-sSFR objects as a result of template choices in the SED fitting.*

range $0.6 < z < 1.8$, $\log(M/M_\odot) >= 10.7$, and sSFR$< 1/3t_H(z)$. There are 134, 163 and 97 galaxies in the redshift bins, $0.6 < z < 0.8$, $0.8 < z < 1.3$ and $1.3 < z < 1.8$, respectively.

TABLE 2.2: *Statistical properties of* q_{proj}

$\log(M/M_\odot) > 10.7$	number	median	mean	stddev	median of z
$1.53 < z < 2.31$ (vdW11)	14	0.665	0.681	0.186	1.69
$1.3 < z < 1.8$	97	0.634	0.612	0.200	1.38
$0.8 < z < 1.3$	163	0.646	0.619	0.213	1.09
$0.6 < z < 0.8$	134	0.734	0.662	0.222	0.69
$0.6 < z < 0.8$ (H12)	533	0.710	0.692	0.179	0.69
$0.04 < z < 0.08$ (vdW09)	18316	0.719	0.692	0.181	0.06

2.3 STRUCTURAL EVOLUTION OF MASSIVE EARLY-TYPE GALAXIES

We now examine two aspects of the structural evolution of early-type galaxies. First, we address the question whether the most massive galaxies are intrinsically round at redshifts $1 < z < 2$, as is observed at $z < 1$ by vdW09 and H12. Second, we address the question whether, in general, early-type galaxies are flatter or rounder (e.g., disk-like or bulge-like) at $z > 1$ than at $z < 1$; H12 showed that there is little evolution up to $z < 1$, but vdW11 presented tentative evidence for a higher incidence of disk-like early-type galaxies at $z \sim 2$.

2.3.1 THE MASS-DEPENDENCE OF EARLY-TYPE GALAXY SHAPES UP TO $z \sim 2$

In Figure 2.7 we show the projected axis ratios of our sample of early-type galaxies as a function of their stellar mass, split into three redshift bins, each with ~ 100 galaxies.

Qualitatively speaking, Figure 2.7 shows the same trend in all redshift bins: there appears to be a mass dependence for the projected axis-ratio, such as was seen in vdW09. As previously demonstrated by H12, at $z \sim 0.7$ we find that the most massive ($\log(M/M_\odot) > 11.3$) early-type galaxies are round in projection and we find a lack of objects that are flat in projection among the most massive early-type galaxies (also see Huertas-Company et al. 2013). In Figure 2.7 a similar trend is seen for early-type

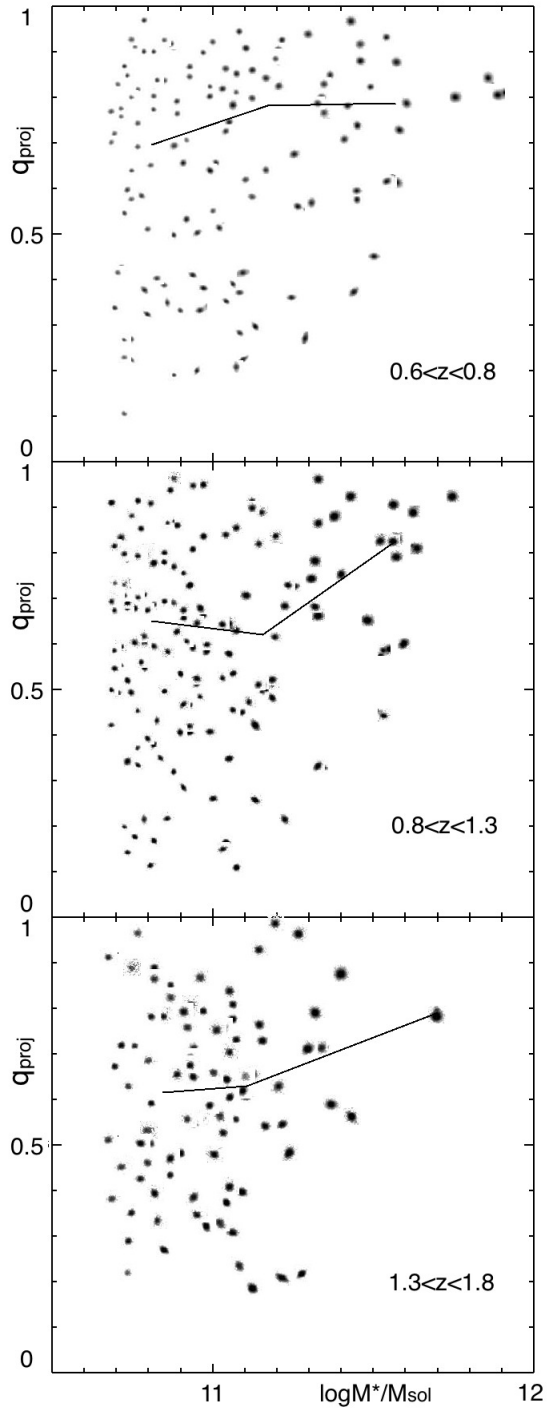

Figure 2.7: *The projected axis ratio versus stellar mass for our early- type galaxy sample, split into three redshift bins. The symbols are the HAWK-I K-band images of the galaxies. The lines represent running median values of the axis ratio. Up to our highest redshift bin, the most massive galaxies appear to be the roundest (see also Figure 2.8 and Sec 3.1). Overall, the galaxies in the highest redshift bins are also flatter than their lower-redshift counterparts (see also Figure 2.9 and Sec 3.2).*

galaxies at $z > 1$: at and below masses of $\log(M/M_\odot) \sim 11$ the galaxies in our sample show a broad range in axis ratios, whereas more massive galaxies are predominantly round. This is consistent with the conclusion reached by Targett et al. (2011), who found that very luminous radio galaxies at $z \sim 2$ have morphological properties similar to today's most massive elliptical galaxies in clusters.

In Figure 2.8 we compare the axis-ratio distributions of galaxies with masses below and above $\log(M/M_\odot) \sim 11.3$. The Mann-Whitney U test shows that the trend seen in Figure 2.7 is marginally significant in each of the redshift bins. For the combined sample of galaxies at redshifts $0.8 < z < 1.8$ we find that the most massive galaxies are rounder than the less massive galaxies with high confidence ($P = 2.51 \times 10^{-4}$, i.e., a 3.66-σ result). For comparison, the equivalent value from the classifical Kolmogorov-Smirnov test is also low ($P_{K-S} = 1.81 \times 10^{-3}$, i.e., a 3.12-$\sigma$ result).

Combining the results from vdW09, H12 and from this chapter, we conclude that at all redshifts $0 < z < 2$ the most massive early-type galaxies are predominantly round in projection. This implies that at all these cosmological epochs the formation mechanism for such massive galaxies precludes the formation of or requires the destruction of pre-existing disks. Our interpretation is that merging, accompanied with little dissipation and star formation, has been the dominant formation channel for galaxies more massive than $\log(M/M_\odot) = 11.3$ since $z \sim 2$. This process is reproduced in early-type galaxy formation models (e.g., Naab et al. 2009; Oser et al. 2012), and the observed major merger rates up to $z \sim 2$ are consistent with theoretical expectations (e.g., Man et al. 2012).

2.3.2 SHAPE EVOLUTION AT $1 < z < 2$

Now we turn to the question whether the structural population properties evolve with redshift. vdW11 found an indication of a high incidence of disk-like early-type galaxies at $z \sim 2$, but their sample is too small to confirm or rule out evolution with respect to the structure of early-type galaxies at the present day. In Figure 2.9 we compare the shape distributions of early-type galaxies with masses $\log(M/M_\odot) > 10.7$ across a broad range in redshift, $0 < z < 1.8$. We reproduce the lack of strong evolution in the range $0 < z < 0.8$, reported by H12.

Vulcani et al. (2011) showed that cluster early-type galaxies are *rounder* at z=0.5-1 than in the local universe. This result is not necessarily at odds with our measurements: their signal is mostly driven by galaxies below our mass limit and, moreover, structural differences between cluster and field galaxies (e.g., van der Wel et al. 2010) can be explained by environmental processes such gas stripping that can produce flat early-

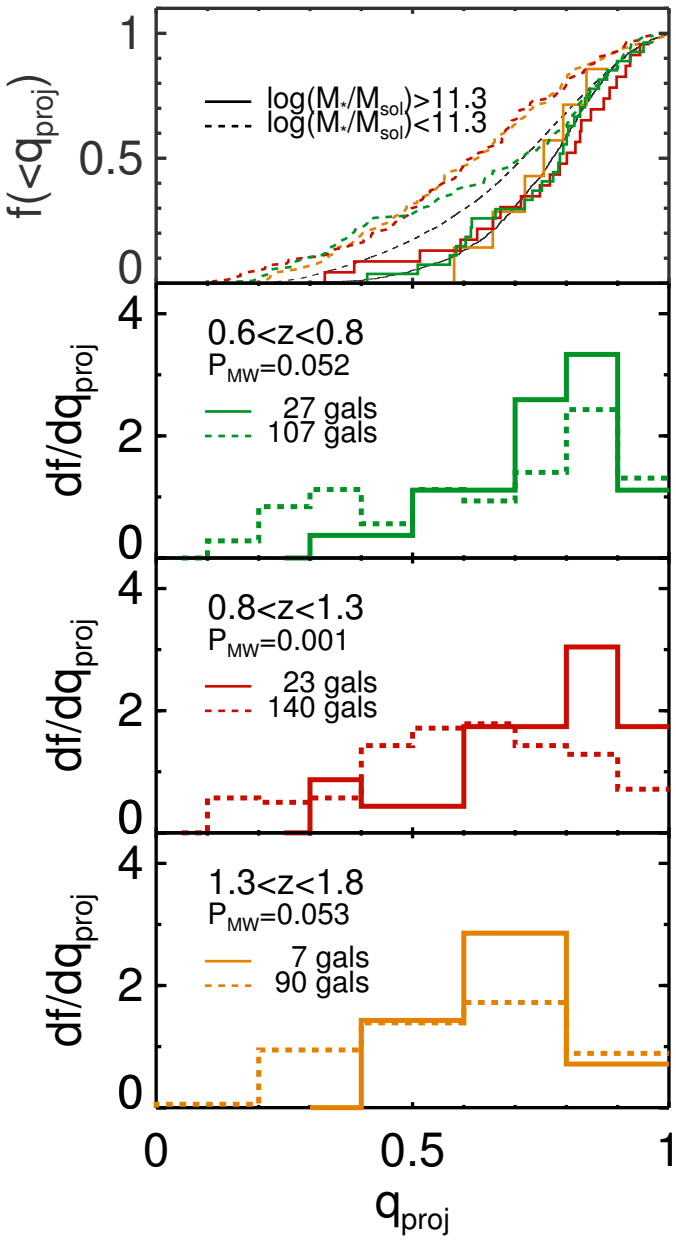

Figure 2.8: *Axis ratio histograms of early-type galaxies with masses* $10.7 < \log(M/M_{\odot}) < 11.3$ *(dashed lines) and early-type galaxies with masses* $\log(M/M_{\odot}) > 11.3$ *(solid lines). The bottom panels show the distributions* (df/dq_{proj}) *of different redshift bins, as indicated; the top panel combine all redshift bins and show the cumulative histograms as a function of projected axis ratio* $(f(< q_{proj})$*, where the color coding corresponds to redshift, following the color coding in the bottom panels. The top panel also shows in black the SDSS-based sample of local early-type galaxies from H12 in the same mass range. At all redshifts the most massive galaxies galaxies are the roundest; the significance of this observation is confirmed by the M-W statistical test (as indicated by the listed probabilities that the samples are statistically the same).*

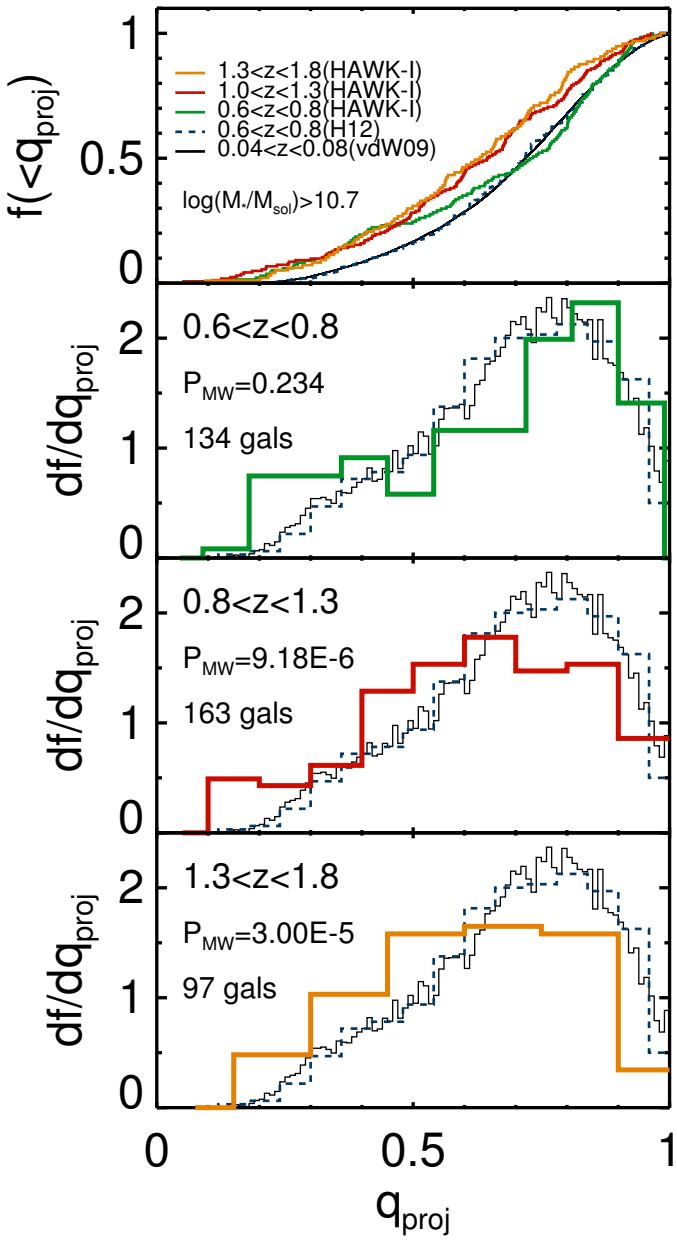

FIGURE 2.9: *Axis ratio histograms (df/dq_{proj}) of early-type galaxies with all masses* $\log(M/M_{\odot}) > 10.7$ *(our full sample) as a function of redshift in bottom three panels, always compared with the present-day sample from H12. The top panel shows cumulative histograms for all redshift bins as a function of projected axis ratio $f(< q_{proj})$. Up to z=0.8, as confirmed by the M-W statistical test (of which the probability is given that the samples are statistically the same) there is no significant redshift evolution in the projected axis-ratio distribution, consistent with the results from H12. At $z > 1$, we find that early-type galaxies are flatter than their present-day counterparts.*

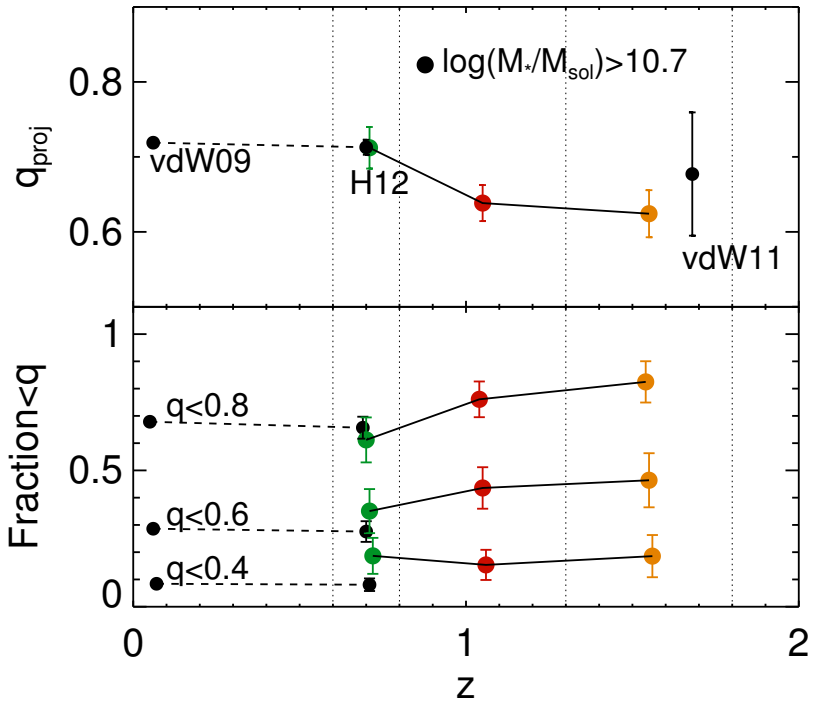

Figure 2.10: *Top panel: median axis ratio of early-type galaxies more massive than* $\log(M/M_{\odot}) > 10.7$ *as a function of redshift. The sample presented in this chapter is represented by the colored data points; the black data points are taken from the literature as indicated. The error bars are estimated by bootstrapping. Bottom panel: fraction of galaxies with axis ratios smaller than indicated, again as a function of redshift. Beyond* $z \sim 1$*, early-type galaxies typically have smaller axis ratios than present-day counterparts in the same mass range, indicative of a more disk-like structure. All error bars are inferred by 95% confidence level compare to the same fraction.*

type galaxies in clusters. An indication that the chosen mass range is relevant is that low-mass galaxies show stronger environmental dependencies in their properties than high-mass galaxies (see, e.g., Peng et al. 2010b). Observations over a broader range of environments and down to lower stellar masses than what is possible with our data set are required to address these issues.

TABLE 2.3: *Kolmogorov-Smirnov test: significant level (*$\log(M/M_\odot) > 10.7$*)*

$\log(M/M_\odot) > 10.7$	$1.53 < z < 2.31$	$1.3 < z < 1.8$	$0.8 < z < 1.3$	$0.6 < z < 0.8$	$0.6 < z < 0.8$	$0.04 < z < 0.08$
$1.53 < z < 2.31$ (vdW11)	-	0.463	0.549	0.671	0.668	0.688
$1.3 < z < 1.8$	0.463	-	0.875	*1.02E-2*[1]	*2.58E-3*	*1.54E-4*
$0.8 < z < 1.3$	0.549	0.875	-	*1.26E-2*	*8.93E-4*	*1.21E-4*
$0.6 < z < 0.8$	0.671	*1.02E-2*	*1.26E-2*	-	0.060	0.035
$0.6 < z < 0.8$ (H12)	0.668	*2.58E-3*	*8.93E-4*	0.060	-	0.584
$0.04 < z < 0.08$ (vdW09)	0.688	*1.54E-3*	*1.21E-4*	0.035	0.584	-

TABLE 2.4: *Mann-Whitney test: significant level (*$\log(M/M_\odot) > 10.7$*)*

$\log(M/M_\odot) > 10.7$	$1.53 < z < 2.31$	$1.3 < z < 1.8$	$0.8 < z < 1.3$	$0.6 < z < 0.8$	$0.6 < z < 0.8$	$0.04 < z < 0.08$
$1.53 < z < 2.31$ (vdW11)	-	0.139	0.167	0.456	0.372	0.373
$1.3 < z < 1.8$	0.139	-	0.315	*1.12E-2* [2]	*1.20E-4*	*3.00E-5*
$0.8 < z < 1.3$	0.167	0.315	-	*2.06E-2*	*8.71E-5*	*9.18E-6*
$0.6 < z < 0.8$	0.456	*1.12E-2*	*2.06E-2*	-	0.249	0.234
$0.6 < z < 0.8$ (H12)	0.372	*1.20E-4*	*8.71E-5*	0.249	-	0.445
$0.04 < z < 0.08$ (vdW09)	0.381	*3.00E-5*	*9.18E-6*	0.234	0.445	-

However, in our higher redshift bins ($z > 0.8$) we see an excess of flat galaxies and a detectable evolution compared to the $z < 0.8$ samples. A Kolmogorov-Smirnov (K-S) and Mann-Whitney U (M-W) tests shows that this trend is highly significant (see Tables 2.3 and 2.4). Note that the axis ratio distribution from vdW11, due to their small sample size, is consistent with both the low- and high-z axis ratio distributions we analyze here.

Figure 2.10 summarizes the observed evolution in the mean projected shape of early type galaxies. Beyond $z \sim 1$ we see a gradual decrease in the median axis ratio of early-type galaxies, which is the result of an increased fraction of galaxies with axis ratios smaller than 0.6. The observed axis-ratio distributions imply that the intrinsic thickness of the typical early-type galaxy is no more than about 0.4. In a forthcoming chapter we will quantify this intrinsic shape through detailed modeling.

The observations presented here can now put on a firmer footing the claim by vdW11 that many high-redshift early-type galaxies display a disk-like structure and that, plausibly, these galaxies will grow into larger, intrinsically round galaxies through merging. The vdW11 sample had been too small to confirm or rule evolution at a fixed stellar mass, which is important in order to differentiate evolutionary paths that galaxies of a

[1] Star symbol (*) represent the significant probability is smaller than 5%. It implies the distributions are distinguishable.

[2] Star symbol (*) represent the significant probability is smaller than 5%. It implies the distributions are distinguishable.

given mass take at different cosmic times. Even at the present-day, the typical early-type galaxy with a mass below $\log(M/M_{\odot}) = 11$ is rather flattened (vdW09), which also corresponds to a disk-like kinematic structure (rotation) as shown by, for example, Emsellem et al. (2011). Here we show that such galaxies had yet thinner intrinsic shapes at $z > 1$. Good correspondence between rotation of the stellar body and flattening has been confirmed up to $z \sim 1$ by van der Wel & van der Marel (2008). Although such confirmation is, so far, lacking at higher redshifts it is reasonable to assume that flattening implies rotation at all redshifts.

We note that beyond the simple observation that early-type galaxies, here defined as galaxies with little star-formation activity, are on average flatter at $z > 1$ than at lower redshifts, we cannot distinguish between the different varieties of such galaxies – such as quiescent spirals, barred/ringed S0s, etc. – and their evolution.

Our results do not argue against a morphological transition that occurs along with the truncation of star formation, as argued by, for example, Bell et al. (2012) on the basis of the high Sérsic indices of quiescent galaxies: high-redshift early-type galaxies such as those studied here, despite the generally disk-like character inferred from their axis ratio distribution, are not pure disks and have higher Sérsic indices than star forming galaxies (e.g., Wuyts et al. 2011a). Based on bulge-disk decompositions, Bruce et al. (2012) arrive at the conclusion that the early-type galaxy population at $z > 1$ is mix of bulge- and disk-dominated galaxies, indicating that the transition from actively star-forming to quiescent need not always coincide with the formation of a dominant bulge. Taken together, these observations are consistent with a picture in which gas had time to settle in a disk before star formation was truncated, and that this disk wholly or partially survived the process that truncated star formation.

2.4 CONCLUSIONS

We measured the projected axis ratios from VLT/HAWK-I K-band imaging of a sample of early-type galaxies in the redshift range $0.6 < z < 1.8$ selected by their low specific star formation rates. We find that at all redshifts $z < 2$ the most massive galaxies $\log(M/M_{\odot}) > 11.3$ are predominantly round. The lack of very massive, highly flattened galaxies suggests a universal ceiling mass for the formation of disks, independent of cosmic epoch. In order for galaxies to grow beyond this ceiling mass, separate evolutionary channel, presumably merging, has to be invoked.

In the full sample ($\log(M/M_{\odot}) > 10.7$), we find, at all redshifts, a large range in projected axis ratios, reflecting a more disk-like structure. In addition, we find quantitative evidence that early-type galaxies at $z > 1$ are more disk-like than their equally massive, present-day counterparts. Therefore, for most early-type galaxies gas had time to settle into a disk before star formation ceased to produce a more passive galaxy. Plausibly, such galaxies grow in mass over time, through mostly dissipationless merging and accretion of satellites, losing some of the angular momentum, and growing in size.

3

Structural Evolution of Early-type Galaxies

Projected axis ratio measurements of 880 early-type galaxies at redshifts $1 < z < 2.5$ selected from CANDELS are used to reconstruct and model their intrinsic shapes. The sample is selected on the basis of multiple rest-frame colors to reflect low star-formation activity. We demonstrate that these galaxies as an ensemble are dust-poor and transparent and therefore likely have smooth light profiles, similar to visually classified early-type galaxies. Similar to their present-day counterparts, the $z > 1$ early-type galaxies show a variety of intrinsic shapes; even at a fixed mass, the projected axis ratio distributions cannot be explained by the random projection of a set of galaxies with very similar intrinsic shapes. However, a two-population model for the intrinsic shapes, consisting of a triaxial, fairly round population, combined with a flat ($c/a \sim 0.3$) oblate population, adequately describes the projected axis ratio distributions of both present-day and $z > 1$ early-type galaxies. We find that the proportion of oblate versus triaxial galaxies depends both on the galaxies' stellar mass, and - at a given mass - on redshift. For present-day and $z < 1$ early-type galaxies the oblate fraction strongly depends on galaxy mass. At $z > 1$ this trend is much weaker over the mass range explored here ($10^{10} < M_*/M_\odot < 10^{11}$), because the oblate fraction among massive ($M_* \sim 10^{11} M_\odot$) was much higher in the past: 0.59 ± 0.10 at $z > 1$, compared to 0.20 ± 0.02 at $z \sim 0.1$. In contrast, the oblate fraction among low-mass early-type galaxies ($\log(M_*/M_\odot) < 10.5$) increased toward the present, from 0.38 ± 0.11 at $z > 1$ to 0.72 ± 0.06 at $z = 0$.

This chapter is based on Chang et al. (2013b), ApJ, 773, 149.

3.1 INTRODUCTION

Early-type galaxies show a large variety in spatial and kinematic structure (e.g., Kormendy & Bender 1996; Emsellem et al. 2011and references therein). Among early types with typical luminosities (L^*) or stellar masses, most have disk-like properties in that they are axisymmetric, rotating and intrinsically flat, even though their light profiles are significantly more concentrated than those of late-type, star-forming L_* galaxies. More massive early-type galaxies are rounder, triaxial, and slowly rotating. Given these fundamental differences, one may surmise that disk-like and spheroid-dominated galaxies have different evolutionary paths and formation mechanisms. Here we empirically address this issue by analyzing the shape distribution of early-type galaxies as a function of redshift. Our reconstruction of the internal structure of early-type galaxies at different cosmic epochs will provide insight into the assembly history of massive, triaxial galaxies as well as the evolutionary path of less massive, disk-like early-type galaxies.

The internal structure of galaxies has been studied by means of analyzing projected shape distributions for several decades. Early on, axisymmetric structure was assumed to describe the three-dimensional light profile of galaxies, that is, the projection of simple oblate and prolate models was used (Hubble 1926; Sandage et al. 1970; Binney 1978; Fall & Frenk 1983). Then the triaxial model family (Stark 1977; Binney 1985; Franx et al. 1991) was considered to account for observational evidence that local early-type galaxies are not axisymmetric (Ryden 1992; Lambas et al. 1992; Tremblay & Merritt 1995; Kimm & Yi 2007; Padilla & Strauss 2008; Méndez-Abreu et al. 2010). Tremblay & Merritt (1996) showed that the projected axis ratio distribution of early-type galaxies is accurately described by a model that consists of an oblate and a triaxial set of objects. Brighter galaxies tend to be more triaxial (non-axisymmetric) than fainter galaxies, which are more axisymmetric and intrinsically flatter (Vincent & Ryden 2005). This two-component model does not provide a mathematically unique solution, but is physically plausible, in line with the kinematic distinction of 'fast rotators' and 'slow rotators' (e.g., Emsellem et al. 2011).

van der Wel et al. (2009b, hereafter vdW09) used stellar masses instead of luminosity, and described the projected axis ratio distribution of early-type galaxies. In addition to enabling a more immediate comparison with galaxy formation models, the use of stellar masses instead of luminosities simplifies the interpretation of evolution with redshift (Holden et al. 2012, hereafter H12) (also see Holden et al. 2009) vdW09 and H12 found that at all redshifts $z \lesssim 1$ there is a quite sudden transition in the projected axis ratio distribution at a stellar mass of $\sim 10^{11} M_{\odot}$. At lower masses the projected axis ratio distribution is broad, indicative of a large fraction of disk-like early-type galaxies, which have a ceiling mass of $\sim 2 \times 10^{11} M_{\odot}$, above which essentially all early-type galaxies are

intrinsically round. H12 provide a quantitative analysis by describing the projected axis ratio distribution of early-type galaxies, and its evolution with redshift by the aforementioned two-component model. Overall, they found little evolution between $z = 0.8$ and the present. van der Wel et al. (2011) and Chang et al. (2013a, hereafter C13) extended these studies to higher redshift. They found that massive early-type galaxies at $z \gtrsim 1.5$ are flatter than at the present. Their implied disk-like structures show that these galaxies formed while gas had time to settle into disks.

The vdW09, H12, and C13 samples were selected by (a lack of) star formation activity (also see Wuyts et al. 2007; Williams et al. 2009). Such a selection can effectively be used as a proxy for a (visual) morphological classification, as a smooth light profile is the main criterion for the visual classification of an early-type galaxy, which usually corresponds to low star-formation activity (also see Patel et al. 2012). A practical advantage of a star formation selection is that it allows for the consistent selection of high-redshift samples, for which visual classification is difficult or impossible. Furthermore, since we are investigating the evolution of structural properties, the use of structural parameters such as concentration or Sérsic index to select early-type galaxies are prone to introducing biases.

So far, these results have been rather qualitative. In this chapter, we provide a more quantitative description of the internal structure of $z = 1 - 2.5$ early-type galaxies down to $M \sim 10^{10} M_{\odot}$. The Cosmic Assembly Near-infrared Deep Extragalactic Legacy Survey (CANDELS, Grogin et al. 2011; Koekemoer et al. 2011), a 902 orbit Hubble Space Telescope (HST) multi-cycle treasury program, provides high-resolution near-infrared imaging aimed at investigating the structural and morphological properties of galaxies to $z \sim 3$ in the rest-frame optical. van der Wel et al. (2012, hereafter vdW12) used `GALFIT` (Peng et al. 2010a) to measure the global structural parameters of $\sim$ 100,000 galaxies in CANDELS. We draw from this work to construct a sample of 569 $z > 1$ early-type galaxies with accurately measured axis ratios.

The structure of this chapter is as follows. In Section 3.2 we describe the data and select our sample of early-type galaxies. In Section 3.3 we analyze the structural parameters of early-type galaxies and their evolution since $z \sim 2.5$ and as a function of stellar mass. In Section 3.4 we describe our models to reconstruct the intrinsic shape distribution. In Section 3.5 we investigate the internal structure of early-type galaxies and its evolution. In Section 3.6 and 3.7 we discuss and summarize our results.

We use AB magnitudes and adopt the cosmological parameters (Ω_M,Ω_Λ,h)=(0.27, 0.73, 0.70) in this chapter.

3.2 DATA

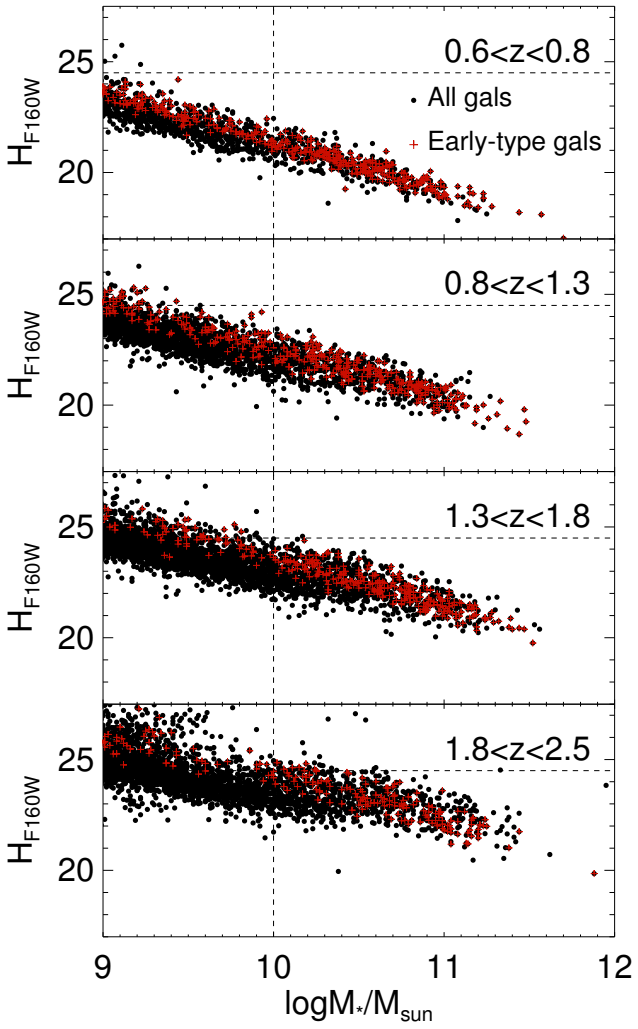

FIGURE 3.1: *CANDELS H_{F160W} magnitude vs. stellar mass at different redshifts. The red crosses represent early-type galaxies, selected as described in Section 3.2.3 and illustrated in Figure 3.2. The black symbols represent all galaxies. We adopt $H_{F160W} = 24.5$ as our magnitude limit: vdW12 showed that size and shape measurements are better than 10% down to this limit. This leads us to adopt a stellar mass limit of $\log(M_*/M_\odot) > 10$, ensuring robust structural parameter estimates for all galaxies in our sample up to $z \sim 2.5$.*

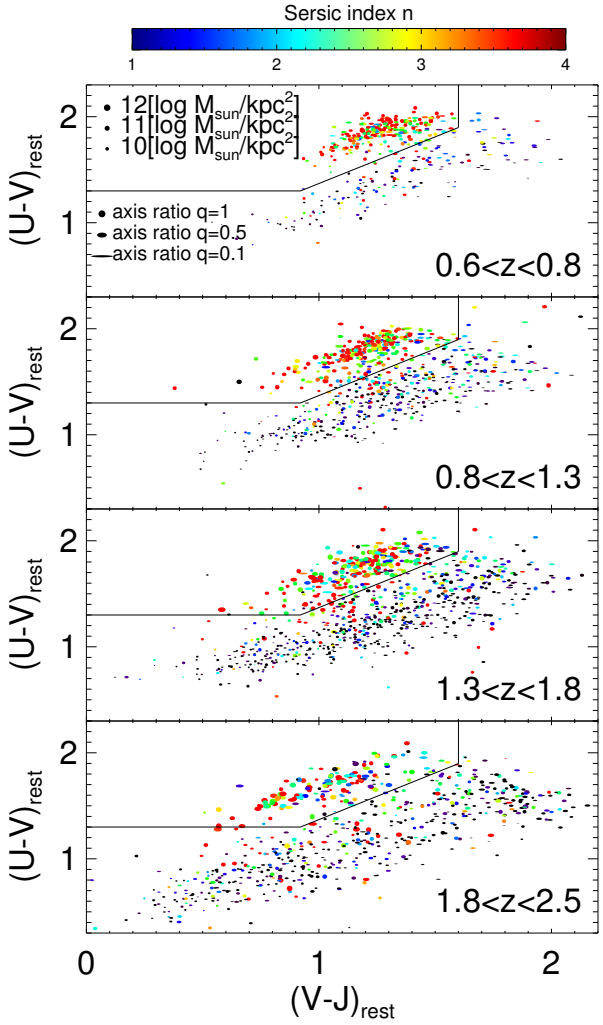

FIGURE 3.2: *Rest-frame $U-V$ vs. rest-frame $V-J$ colors for galaxies in four redshift bins. As shown, e.g., by Williams et al. (2009), the black polygons effectively separate star-forming and quiescent galaxies, which we use in this chapter to select our early-type sample. The symbols' color coding corresponds to the Sérsic index n, the symbol size (area) with stellar mass surface density ($M_*/2\pi qR_{\rm eff}^2$), and symbol shape with observed, projected axis ratio q. The color-color selection separation of early- and late-type galaxies corresponds well with their structural properties in the sense that early-type galaxies have high Sérsic indices and large surface mass densities.*

3.2.1 MULTI-WAVELENGTH DATA AND SED FITTING

In this chapter, we use imaging and multi-wavelength catalogs from CANDELS in the Great Observatories Origins Deep Survey-South field (GOODS-S, Giavalisco et al.

2004, 'wide' over 4'×10' and 'deep' over 7×10') and Ultra Deep Survey field (UDS; Lawrence et al. 2007wide over 9'×24'). The deep near-infrared HST survey allows us to select early-type galaxies up to $z = 2.5$. The details of the multi-wavelength catalogs are described in Guo et al., (2013, GOODS-S), Galametz et al. (2013, UDS), and Ashby et al. (2013, IRAC SEDS catalog).

The method and algorithms for acquiring photometric redshifts, rest-frame colors and stellar masses are described by Wuyts et al. (2011a). Briefly, photometric redshifts are estimated by EAzY (Brammer et al. 2008) and available spectroscopic redshifts are included. The stellar masses, star-formation rates, and rest-frame colors are estimated by FAST (Kriek et al. 2009). The Bruzual & Charlot (2003) model, and a Chabrier (2003) stellar initial mass function is adopted. A range of ages, star formation histories and extinction parameters is explored.

3.2.2 GALAXY STRUCTURAL PARAMETERS

The structural parameters (radii, Sérsic indices and projected axis ratios) are taken from vdW12 who fit single Sérsic profiles to individual galaxies with `GALFIT`. Many of the galaxies in our sample are very small (∼ 1kpc), close to the resolution limit. If the point spread function (PSF) is precisely known, this is not a problem as shown by vdW12, at least under the assumption that the characterization of the light profile by a single Sérsic component is reasonable. In order to test the sensitivity of our results to errors in the PSF model, we refit our sample with the 'wrong' PSF: if we convolve the Sérsic profile with the F125W PSF model in order to fit the F160W images, the resulting axis ratios are larger, but not to the extent that our results are affected. Since we know the F160W PSF with much better accuracy than the ∼ 15% difference between the F125W and F160W PSFs ($\mathrm{FWHM}_{F125W} \sim 0''.20$; $\mathrm{FWHM}_{F160W} \sim 0''.17$), we conclude that errors in our PSF model do not affect our results.

3.2.3 SAMPLE SELECTION

Combining the multi-wavelength and structure parameter catalogs, we have an initial sample of 56,010 objects (21,889 in GOODS-S and 34,121 in UDS). Size and shape measurements are accurate and precise to 10% for galaxies with $H_{F160W} \sim 24.5$ (see vdW12). We adopt a stellar mass limit of $M = 10^{10} M_{\odot}$, which allows us to consistently compare galaxies at all redshift $z < 2.5$ (see Figure 3.1). We reject stars by including only objects with $J - H > 0.15$. We only include galaxies with good `GALFIT` fits (flag=0; 87% of the remaining sample) from the vdW12 catalog and ignore 13%

with suspect fits (flag=1) or bad fits (flag=2). This mass-selected sample with reliable structure measurements consists of 2,827 objects.

To separate quiescent galaxies from star-forming galaxies, we use color-color selection criteria as shown in Figure 3.2, following: $(U-V) > 0.88\times(V-J)+0.49$, $(U-V) > 1.3$ and $(V-J) < 1.6$. [1] We define these as early-type galaxies and the remainder as late-types. This approach follows the technique outlined by, Williams et al. (e.g., 2009), but the color selection criteria are slightly different to account for differences in filter transmission curves and small offsets in the flux measurements. In Figure 3.2 it can be seen that this star-formation activity- based selection corresponds well with the Sérsic index, indicating that our selection by star formation activity is effectively equivalent to a concentration-based definition of early type (also see Bell 2008; Wuyts et al. 2011a; Bell et al. 2012; Wuyts et al. 2012) over the full redshift range probed here. As noted before, star-formation activity is strongly anti-correlated with Sérsic index and surface mass density, up to at least $z = 2.5$. Even though in this chapter we emphasize the diskiness of early-type galaxies, it is also apparent in Figure 3.2 that late-type galaxies are still flatter, that is, more disk-like, than early-type galaxies at all redshifts.

The final sample of mass-selected early-type galaxies with reliable (flag=0) structure measurements consists of 880 galaxies in the redshift range $0.6 < z < 2.5$. The numbers of galaxies in different redshift bins are shown in Table 3.1. We create three stellar mass bins for CANDELS with a roughly equal number of galaxies.

TABLE 3.1: *Sample sizes*

$\log(M_*/M_\odot)$	$10.1-11.5$	$10.8-11.5$	$10.5-10.8$	$10.1-10.5$
redshift	numbers			
SDSS	32842	13640	13991	5211
H12	1321	384	475	462
$1 < z < 2.5$	569	197	168	204
$0.6 < z < 0.8$	220	47	67	106
$0.8 < z < 1.3$	256	78	66	112
$1.3 < z < 1.8$	244	88	71	85
$1.8 < z < 2.5$	147	55	47	45

The SDSS sample from H12 is used as a low-redshift benchmark. Here, the early-type galaxies are selected by an equivalent color-color criterion. We verified that rejecting all SDSS color-color selected early-type galaxies with detected $H\alpha$ emission ($\sim 18\%$ of the sample) does not change our results. Even though the galaxies with detected emission lines are on average somewhat flatter than their counterparts without emission lines, the axis ratio distribution analyzed in the subsequent sections is not significantly altered.

[1] To compute the rest-frame U, V, and J band fluxes, we use the UX and V Bessell filters and the Palomar J filter.

Sufficiently deep emission-line data are not available for the galaxies in CANDELS. Instead, we search for detections in public MIPS 24 μm imaging in the UDS[1] and cataloged MIPS 24 μm flux measurements from Wuyts et al. (2008) in GOODS-S. Removing the 3-σ detected objects ($\sim$ 16%) does not change the projected axis ratio distributions significantly. We conclude that the evolutionary trends with redshift are not sensitive to the inclusion of contaminating populations of star-forming galaxies and/or active galactic nuclei.

3.3 EVOLUTION OF THE PROJECTED AXIS RATIO DISTRIBUTION

In Figure 3.3 we show the axis-ratio distributions of early-type galaxies as a function of stellar mass for a number of redshift bins from $z = 0.6$ to $z = 2.5$. Half-light radii (R_{eff}) and Sérsic indices (n) are represented by varying the symbol size and color coding, respectively. Over the whole stellar mass range probed here the typical R_{eff} and n increase from $z \sim 2.5$ to later times, while non-starforming galaxies with exponential light profiles are rare at all redshifts. As previously reported by vdW09, H12, and C13, the most massive galaxies are the roundest, which can be seen here in particular at $z \sim 1$; at higher redshifts the probed volume is too small to include a sufficiently large number of very massive galaxies.

The main results presented in this chapter can all be qualitatively seen in Figure 3.3. First, as was also shown by C13, there are many flat early-type galaxies with mass $\sim 10^{11} M_{\odot}$ at $z > 1$. Second, and contrarily, there are not many flat early-type galaxies with mass $\sim 10^{10} M_{\odot}$ at $z > 1$. The overall tendency is that the dependence of shape on galaxy mass is weak at $z > 1$ and strong at $z < 1$. To investigate these indications of structural evolution in a quantitative way, we will model the projected axis ratio distributions to infer the intrinsic shape distribution in Section 3.5.

But first, we will establish the significance of these trends in a model-independent manner. In Figure 3.4, we perform least-squares fits to the axis ratios of the full $0.6 < z < 2.5$ sample separated into three mass bins, anchored by the low-redshift median values from the SDSS sample to which we assign a 0.01 systematic uncertainty (see H12). The uncertainties on the least-square fits are obtained by bootstrapping the sample and perturbing the photometric redshift (z_{phot}) and the projected axis ratio by their measurement uncertainties. Moreover, uncertainties in stellar masses (M_*) are included in two steps: first, the perturbation in photometric redshift is propagated ($M_* \propto (1+z)^4$) and, second, a random mass uncertainty of 0.2 dex (see, e.g., van der Wel et al. 2006) is included.

[1] http://irsa.ipac.caltech.edu/data/SPITZER/SpUDS

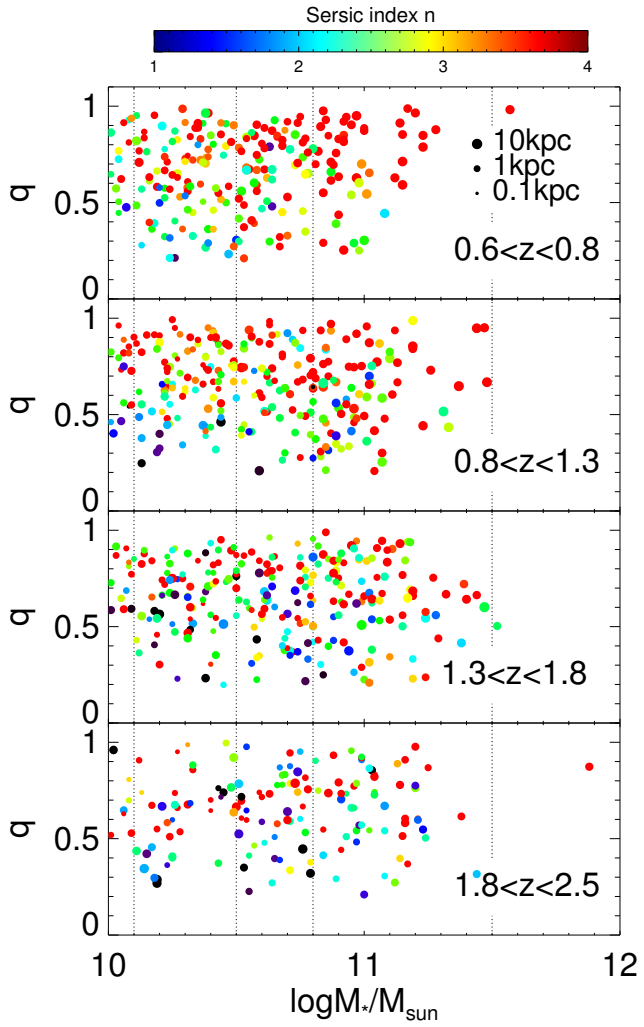

FIGURE 3.3: *Projected axis ratio vs. stellar mass for early-type galaxies in CANDELS in four redshifts bins. The symbols' color coding corresponds to the Sérsic index n, the symbol size represents the radius in kiloparsecs. High-mass early-type galaxies are rounder and have higher Sérsic indices than low-mass early-type galaxies, but these trends apparently weaken at $z \sim 2$. At all redshifts, flatter galaxies have lower Sérsic indices, indicating that the population exists of a mix of different types of galaxies, and that variation in projected shape is not only the result of different viewing angles. The thin vertical lines indicate the mass bins that we use in this chapter, and are chosen to contain similar numbers of galaxies.*

Figure 3.4 shows that there is significant evolution in the projected axis ratios for massive galaxies, with the projected axis ratios decreasing toward high redshift, and we find marginal evidence for increasing projected axis ratios with redshift for the lowest-mass sample.

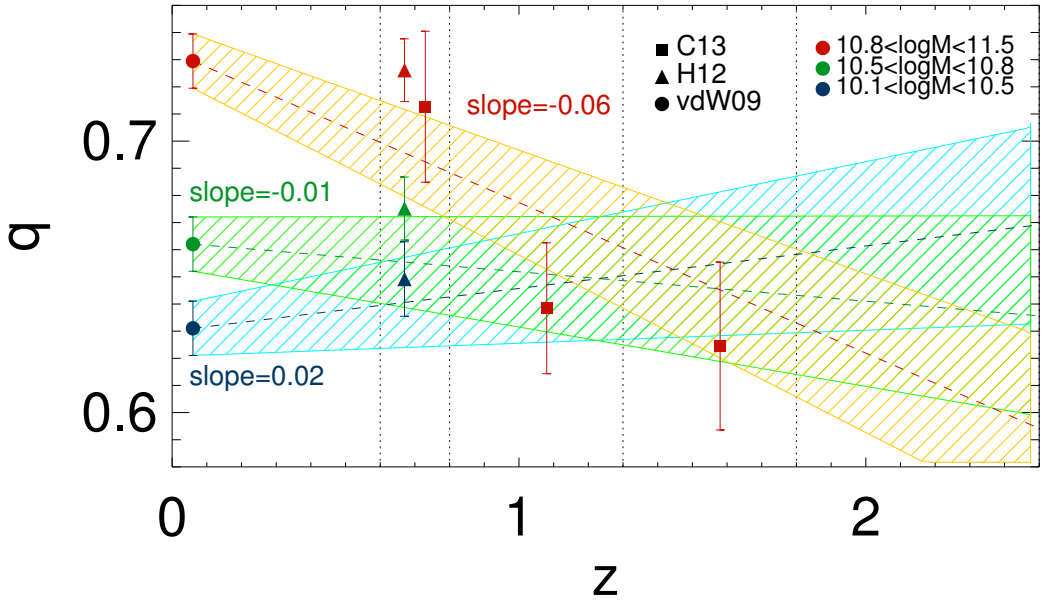

FIGURE 3.4: *Evolution of the projected axis ratios for galaxies in three mass bins (color coding). The filled symbols are median values of previously published results. The dashed lines represent fits to the redshift-axis ratio distribution of the individual objects in the CANDELS sample, anchoring to the median axis ratio of present-day galaxies. The shaded area indicates the 1-σ uncertainty. See the text for details on the fitting method. The most significant evidence for evolution is seen for the massive galaxies: these are progressively flatter at higher redshift.*

We now turn to the full distribution of axis ratios, which, compared to evolution in the average or median, enables more sensitive tests for structural evolution. In Figure 3.5, we compare the axis ratio distributions of our $1 < z < 2.5$ early-type galaxies with local early-type galaxies (see vdW09 and H12) by means of cumulative distributions and of histograms. Figure 3.5 shows that for $\log(M_*/M_\odot) > 10.8$, high-redshift galaxies are flatter (have smaller projected axis ratios) than local galaxies, while for $\log(M_*/M_\odot) < 10.5$, high-redshift galaxies are rounder. We use Kolmogorov-Smirnov (K-S) and Mann-Whitney U (M-W) tests to show that these trends are significant at the 5-σ and 3-σ level, respectively. These quantitative comparisons confirm the hints seen in Figure 3.3.

While the flattening of high-mass galaxies is consistent with previous results (van der Wel et al. 2011; Bruce et al. 2012; Whitaker et al. 2012; Buitrago et al. 2013, and C13), the 3-σ level evidence that low-mass early types were rounder at earlier epochs is surprising. One could suspect that systematic shape measurement errors may prevent us from recovering the actual flatness of the small, faint galaxies in this sub-sample. However, the simulations performed by vdW12 indicate that shapes and sizes can be recovered with high accuracy down to the regime probed here. Note, however, that

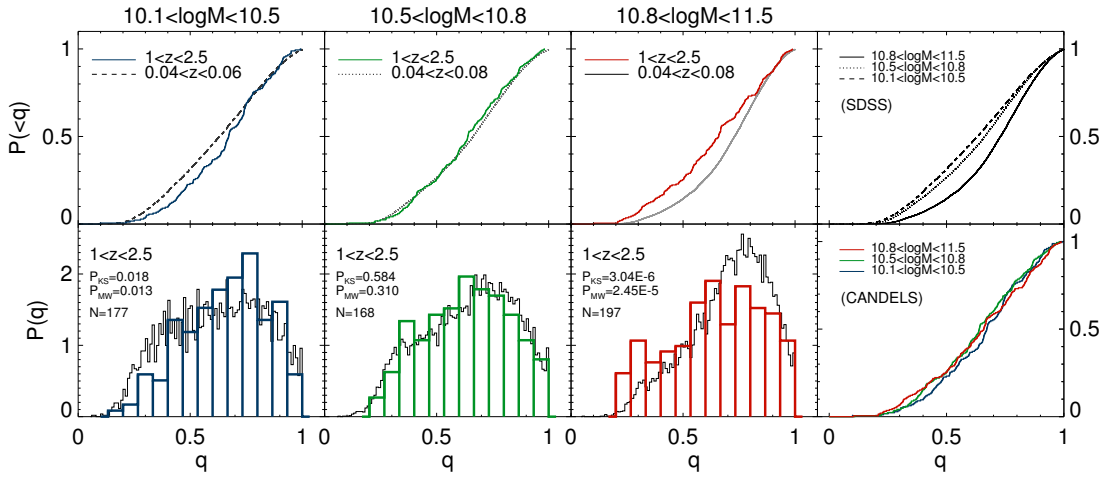

FIGURE 3.5: *Redshift evolution of the projected axis ratio distributions in different mass bins. The top row of panels shows cumulative distributions; the bottom row shows binned histograms. The colored lines and histograms represent the* $1 < z < 2.5$ *CANDELS early-type galaxy sample; the gray/black lines represent the present-day early-type galaxy sample from SDSS. The right most panels combine the cumulative histograms for the present-day sample (top) and high-redshift sample (bottom), separated according to the mass bins. Probabilities that the distributions are consistent with each other from two statistical tests (Kolmogorov-Smirnov and Mann-Whithney) are given in the bottom panels. The samples high- and low-mass bins show evidence for evolution in opposite directions: whereas high-mass galaxies are flatter at high redshifts, low-mass galaxies are rounder.*

those simulations were performed with ideal Sérsic profiles, not with real galaxy light profiles. In addition, we can ask whether mismatches in the PSF model matter. In order to test this we rerun the profile fits on the F125W images of this sub-sample of low-mass early-type galaxies. For this test we replace the F125W PSF model, which we assume to be accurate, with the F160W PSF model. We know that the F160W PSF model is too broad to describe the light profiles of point sources in the F125W imaging (by $\sim$ 15%). Therefore, the projected axis ratio will now be underestimated (objects will appear flatter than they are). Even with this crudely wrong PSF model we find that the axis ratios of the low-mass $z > 1$ early types are not flatter than the axis ratios of their present-day counterparts. Given that the uncertainty in our PSF models is much smaller than the difference between the F125W and F160W PSF models, we can safely conclude that the observed evolution in the axis ratio distribution for low-mass early-type galaxies is not due to uncertainties in our PSF models.

Now we proceed in the next two sections to reconstruct the intrinsic structural properties of early-type galaxies as a function of stellar mass and redshift. We explore a variety of approaches that employ different model families and search for solutions by assuming random viewing angle distributions for our samples. In Section 3.4 we apply an

analytical approximation to reconstruct the intrinsic axis ratio distribution of axisymmetric model families. In Section 3.5 we project model distributions that represent a combination of axisymmetric and triaxial families in order to reproduce the observed distributions of projected axis ratios and to find best-fitting solutions.

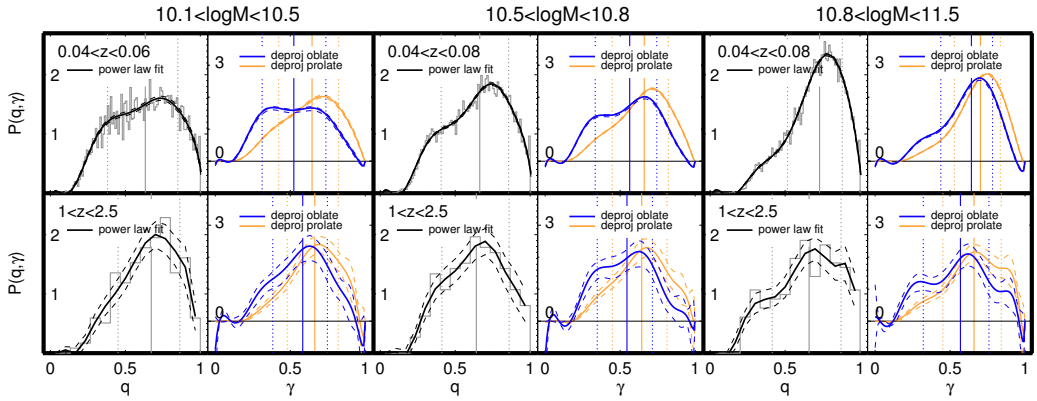

FIGURE 3.6: *Projected axis ratio (q) distributions in gray/black and deprojected, intrinsic axis ratio (γ) distributions in blue/orange, inferred as described in Section 3.4. Observed, projected axis ratio distributions (black histograms) are represented by eighth-order polynomials (black lines) and then analytically deprojected according to Equation (3.1) to infer the intrinsic shape distribution of axisymmetric model populations (oblate in blue; prolate in orange). The dashed lines below and above the solid lines represent the 16 and 84 percentile confidence intervals obtained from bootstrapping ($n = 10,000$). The vertical lines show the 16, 50, and 84 percentiles of the deprojected intrinsic axis ratios. The top row of panels shows present-day early-type galaxies from SDSS; the bottom row shows $1 < z < 2.5$ early-type galaxies from CANDELS.*

3.4 ANALYTICAL RECONSTRUCTION OF THE INTRINSIC SHAPE DISTRIBUTION

For an oblate ellipsoid at the origin of a Cartesian coordinate system, the intrinsic shape can be written as $x^2 + y^2 + z^2/\gamma^2 = 1$, where γ ($0 < \gamma \leq 1$) is the intrinsic axis ratio between the (one) short axis and the (two) long axes. For a prolate ellipsoid, the intrinsic shape can be written as $x^2/\gamma^2 + y^2/\gamma^2 + z^2 = 1$, where γ ($0 < \gamma \leq 1$) is the intrinsic axis ratio between the (two) short axes and the (one) long axis. The intrinsic axis-ratio

distribution, $\psi(\gamma)$, can be inferred as prescribed by Fall & Frenk (1983):

$$\psi_O(\gamma) = \frac{2}{\pi}\sqrt{1-\gamma^2}\frac{d}{d\gamma}\int_0^q \frac{\phi_O(q)dq}{\sqrt{\gamma^2-q^2}} \tag{3.1a}$$

$$\psi_P(\gamma) = \frac{2}{\pi}\frac{\sqrt{1-\gamma^2}}{\gamma^2}\frac{d}{d\gamma}\int_0^q \frac{\phi_P(q)q^3dq}{\sqrt{\gamma^2-q^2}}, \tag{3.1b}$$

where ϕ is the projected axis-ratio distribution, and the subscripts O and P refer to the oblate and prolate case, respectively. If we describe the projected axis-ratio distribution by a power law ($\phi(q) = (m+1)q^m$ with $m > -1$), we can rewrite Equation (3.1) analytically:

$$\psi_O(\gamma) = \frac{2\gamma^{m-1}\sqrt{1-\gamma^2}}{B(0.5m, 1.5)} \tag{3.2a}$$

$$\psi_P(\gamma) = \frac{2\gamma^{m}\sqrt{1-\gamma^2}}{B(0.5m+0.5, 1.5)}, \tag{3.2b}$$

where $B(x, y)$ is the beta function. The reconstructed intrinsic axis ratio distribution should be non-negative if an oblate or prolate model is a good description of the data.

3.4.1 Application

Figure 3.6 shows the results of the deprojection outlined above. We use an eighth-order power law, $\phi(q) = \Sigma_{m=0}^{8} C_m(m+1)q^m$, to describe the observed projected axis ratio distributions (black lines in Figure 3.6). The dashed lines show the 16 and 84 percentile confidence intervals obtained from bootstrapping (e.g., Tremblay & Merritt 1995, 1996; Ryden 1996a,b). The reconstructed intrinsic shape distributions for the oblate and prolate models (shown in thick blue and orange lines, respectively) are sometimes slightly negative, but the uncertainties are such that this can be attributed to the limited sample size. The distributions are very broad; that is, in narrow ranges of mass, galaxies display a large variety in intrinsic shape, and the population cannot consist of objects that are all similar in intrinsic thickness. This is true both for present-day galaxies and for $z > 1$ galaxies. Changes in the intrinsic shape distribution with redshift mirror changes in the projected shape distribution: high-mass galaxies were on average flatter at $z > 1$, and low-mass galaxies were rounder. Especially for the large, present-day samples, there is a clear hint that multiple components (galaxy populations) are needed to describe the intrinsic shape distribution, which we will explore below.

3.5 PROJECTION OF AXISYMMETRIC AND TRIAXIAL MODELS

Following Binney (1985) Equation (11) and (12), we project a triaxial ellipsoid (written as $m^2 = x^2/a^2 + y^2/b^2 + z^2/c^2$, at the origin of Cartesian coordinate system) and compute the projected axis ratio q as follows:

$$A = \frac{\cos^2\theta}{\gamma^2}\left(\sin^2\phi + \frac{\cos^2\phi}{\beta^2}\right) + \frac{\sin^2\theta}{\beta^2} \tag{3.3a}$$

$$B = \cos\theta \sin 2\phi \left(1 - \frac{1}{\beta^2}\right)\frac{1}{\gamma^2} \tag{3.3b}$$

$$C = \left(\frac{\sin^2\phi}{\beta^2} + \cos^2\phi\right)\frac{1}{\gamma^2} \tag{3.3c}$$

$$q(\theta, \phi; \beta, \gamma) = \sqrt{\frac{A + C - \sqrt{(A-C)^2 + B^2}}{A + C + \sqrt{(A-C)^2 + B^2}}}, \tag{3.3d}$$

where (θ,ϕ) are the polar and azimuthal viewing angles in a spherical coordinate system, and $\beta = b/a$ and $\gamma = c/a$. Note that $\beta = 1$ and $\beta = \gamma$ correspond to the special, axisymmetric cases (oblate and prolate, respectively). In order to account for variations in intrinsic shape, we assume a Gaussian distribution for the triaxiallity $T(= [1-\beta^2]/[1-\gamma^2])$ and ellipticity $E(= 1-\gamma)$ with dispersion σ_T and σ_E.

For a given set of parameters (T,E,σ_T,σ_E), we numerically generate distributions for β and γ. Then, a random viewing angle (θ,ϕ) is assigned to each of the elements of the distribution (100,000 in our case) such that with Equation (3.3) the projected axis ratio distribution can be generated. This distribution corresponds to the probability distribution $p(q_{model})$.

For nearly round ($q \sim 1$) galaxies, random noise will always cause the measured q to be an underestimate as the position angle of the long axis becomes ill-determined. This affects the projected axis-ratio distribution as described by Rix & Zaritsky (1995) (Equation (C5)):

$$P_e(\epsilon, \epsilon_e, \Delta\epsilon) = \frac{\epsilon}{\Delta\epsilon^2} I_o\left(\frac{\epsilon\epsilon_e}{\Delta\epsilon^2}\right) \exp\left(-\frac{\epsilon^2 + \epsilon_e^2}{2\Delta\epsilon^2}\right), \tag{3.4}$$

where $\epsilon(= 1 - q)$ is the measured ellipticity, ϵ_e is the expected ellipticity, $\Delta\epsilon$ is the measured error, and P_e is the expected ellipticity distribution. We numerically implement the difference between ϵ and ϵ_e to correct the generated probability distribution $p(q_{model})$. We adopt fixed values $\Delta\epsilon = \Delta q$ for each of the data sets used here: 0.03 and 0.05 for the low- and high-z data sets from H12, and 0.04 for the CANDELS data set.

The total likelihood L for a measured set projected axis ratios q_{data} and a given set of model parameters T, E, σ_T, and σ_E is given by $L = \Sigma_{q_{data}} \log p(q_{data}|q_{model})$, where p has a minimum value of 0.01.

L is computed for a grid of model parameters, chosen in various ways for the different approaches explored below, such that the maximum likelihood model can be located in the grid and the best-fitting model is identified.

In order to obtain uncertainty estimates on the best-fitting model parameters, we bootstrap the observed data (q_{data}), also perturbing q_{data} by the measurement uncertainty and perturbing the redshift and stellar mass estimates as described in Section 3.3.

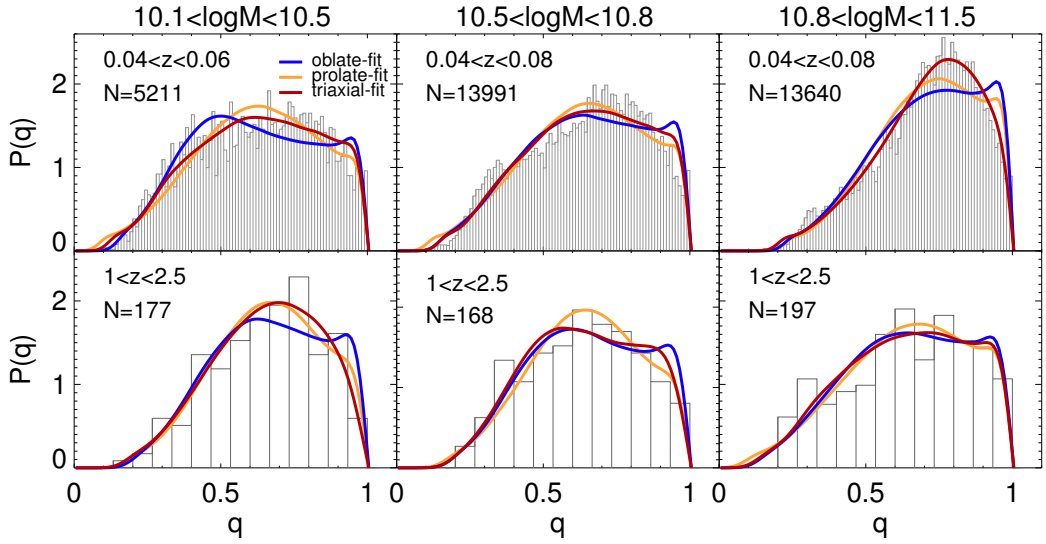

Figure 3.7: *Histograms show observed distributions of projected axis ratios for present-day early-type galaxies from SDSS (upper row) and at* $1 < z < 2.5$ *from CANDELS (bottom row), each in three mass bins. The colored lines represent the best-fitting, single-component models with Gaussian distributions for intrinsic axis ratios, with the oblate model in blue, the prolate model in orange, and the triaxial model in red. See Section 3.5.1.1 for details. The mean and dispersion of the best-fitting Gaussians are listed in Table 3.2.*

3.5.1 APPLICATION

3.5.1.1 SINGLE-COMPONENT MODEL FOR THE INTRINSIC SHAPE

For each of the SDSS (vdW09), COSMOS/GEMS (H12), and CANDELS data sets we search for the best-fitting triaxial model as described above on a grid spaced as (ΔT, $\Delta\sigma_T$, ΔE, $\Delta\sigma_E$)=(0.04, 0.04, 0.01, 0.01). We separately consider the two special cases: oblate, with $T = 0$ and $\sigma_T = 0$; and prolate, with $T = 1$ and $\sigma_T = 0$. As before, the samples are analyzed in bins of stellar mass and redshift. The results are given in Table 3.2 and a subset are shown in Figure 3.7. For each best-fitting model we estimate the goodness-of-fit by computing the K-S and M-W probabilities that the observed q_{data} represent a population of galaxies with a projected axis ratio distribution q_{model}. Note that our fitting method does not aim to maximize the probabilities given by these goodness-of-fit indicators.

As noted by H12, the axis ratio distribution of present-day early-type galaxies cannot generally be accurately described by a single-component model with Gaussian distributions for the intrinsic parameters. The one exception is that massive early-type galaxies ($\log(M_*/M_\odot) > 10.8$) quite closely resemble a single, highly triaxial population ($T = 0.6$). At all redshifts up to $z = 2.5$ no prolate model fits the data, while an oblate model cannot be ruled out. The oblate model fitting results reflect the previously mentioned evolution in the median axis ratio: the intrinsic ellipticity for the most massive galaxies increases from $E = 0.48$ at $z < 0.1$ to $E = 0.61$ at $z > 1$, while it decreases from $E = 0.66$ to $E = 0.56$ for galaxies in the mass range $10.1 < \log(M_*/M_\odot) < 10.5$.

TABLE 3.2: *Single-component fitting results*

Model	Mass($\log(M_*/M_\odot)$)	redshift(z)	T [1]	σ_T	E [2]	σ_E	P_{K-S} [3]	P_{M-W}
single oblate model								
Oblate	10.8-11.5	0.04-0.08 (SDSS)	0	0	0.48 ± 0.01 [4]	0.18 ± 0.01	*0.00* [5]	*0.01*
Oblate	10.5-10.8	0.04-0.08 (SDSS)	0	0	0.61 ± 0.00	0.18 ± 0.00	*0.00*	*0.01*
Oblate	10.1-10.5	0.04-0.06 (SDSS)	0	0	0.66 ± 0.01	0.13 ± 0.01	*0.00*	0.16
Oblate	10.8-11.5	0.6-0.8 (H12)	0	0	0.46 ± 0.03	0.17 ± 0.03	0.21	0.20
Oblate	10.5-10.8	0.6-0.8 (H12)	0	0	0.58 ± 0.04	0.17 ± 0.04	0.24	0.46
Oblate	10.1-10.5	0.6-0.8 (H12)	0	0	0.58 ± 0.03	0.14 ± 0.03	0.12	0.13
Oblate	10.8-11.5	1-2.5	0	0	0.61 ± 0.03	0.18 ± 0.03	0.99	0.45
Oblate	10.5-10.8	1-2.5	0	0	0.59 ± 0.04	0.14 ± 0.03	0.69	0.26
Oblate	10.1-10.5	1-2.5	0	0	0.56 ± 0.03	0.15 ± 0.03	0.41	0.34
single prolate model								
Prolate	10.8-11.5	0.04-0.08 (SDSS)	1	0	0.37 ± 0.00	0.18 ± 0.00	*0.00*	0.34
Prolate	10.5-10.8	0.04-0.08 (SDSS)	1	0	0.45 ± 0.00	0.20 ± 0.01	*0.00*	0.07
Prolate	10.1-10.5	0.04-0.06 (SDSS)	1	0	0.47 ± 0.00	0.20 ± 0.00	*0.00*	0.35
Prolate	10.8-11.5	0.6-0.8 (H12)	1	0	0.36 ± 0.02	0.17 ± 0.02	0.70	0.26
Prolate	10.5-10.8	0.6-0.8 (H12)	1	0	0.42 ± 0.03	0.20 ± 0.02	0.29	0.35
Prolate	10.1-10.5	0.6-0.8 (H12)	1	0	0.45 ± 0.02	0.17 ± 0.02	0.24	0.41
Prolate	10.8-11.5	1-2.5	1	0	0.44 ± 0.03	0.21 ± 0.02	0.90	0.48
Prolate	10.5-10.8	1-2.5	1	0	0.45 ± 0.02	0.17 ± 0.02	0.55	0.37
Prolate	10.1-10.5	1-2.5	1	0	0.43 ± 0.02	0.17 ± 0.02	0.61	0.47
single triaxial model								
Triaxial	10.8-11.5	0.04-0.08 (SDSS)	$0.60^{+0.00}_{-0.08}$	$0.16^{+0.00}_{-0.12}$	$0.45^{+0.02}_{-0.00}$	$0.23^{+0.00}_{-0.01}$	*0.03*	0.15
Triaxial	10.5-10.8	0.04-0.08 (SDSS)	$0.92^{+0.00}_{-0.92}$	$0.00^{+0.66}_{-0.00}$	$0.47^{+0.16}_{-0.00}$	$0.24^{+0.00}_{-0.06}$	*0.00*	0.12
Triaxial	10.1-10.5	0.04-0.06 (SDSS)	$0.92^{+0.02}_{-0.92}$	$0.00^{+0.24}_{-0.00}$	$0.50^{+0.17}_{-0.00}$	$0.26^{+0.00}_{-0.11}$	*0.03*	0.13
Triaxial	10.8-11.5	0.6-0.8 (H12)	$0.76^{+0.00}_{-0.62}$	$0.92^{+0.00}_{-0.92}$	$0.44^{+0.06}_{-0.05}$	$0.20^{+0.05}_{-0.04}$	0.82	0.34
Triaxial	10.5-10.8	0.6-0.8 (H12)	$0.92^{+0.00}_{-0.72}$	$0.00^{+0.06}_{-0.00}$	$0.43^{+0.20}_{-0.00}$	$0.25^{+0.09}_{-0.06}$	0.39	0.18
Triaxial	10.1-10.5	0.6-0.8 (H12)	$0.92^{+0.04}_{-0.88}$	$0.00^{+0.28}_{-0.00}$	$0.47^{+0.18}_{-0.00}$	$0.21^{+0.04}_{-0.09}$	0.40	0.26
Triaxial	10.5-10.8	1-2.5	$0.00^{+0.72}_{-0.00}$	$0.20^{+0.08}_{-0.20}$	$0.61^{+0.05}_{-0.10}$	$0.13^{+0.06}_{-0.05}$	0.53	0.38
Triaxial	10.8-11.5	1-2.5	$0.92^{+0.04}_{-0.82}$	$0.00^{+0.04}_{-0.00}$	$0.47^{+0.17}_{-0.03}$	$0.26^{+0.02}_{-0.11}$	0.75	0.33
Triaxial	10.1-10.5	1-2.5	$0.00^{+0.80}_{-0.00}$	$0.52^{+0.00}_{-0.52}$	$0.56^{+0.05}_{-0.07}$	$0.17^{+0.07}_{-0.03}$	0.70	0.47

[1] T is the mean triaxiality parameter, with standard deviation σ_T; these are set to 0 or 1 for the oblate and prolate models.

[2] E and σ_E are the ellipticity (1 minus the intrinsic short-long axis ratio) and its standard deviation.

[3] The final two columns list the K-S and M-W probabilities that the observed and best-fitting model projected axis ratio distributions are indistinguishable, for a randomly drawn realization of the model distribution with the same number of objects as the observed samples. These serve as a crude goodness-of-fit test.

[4] Uncertainties are obtained from bootstrapping.

[5] Star symbol (*) represent the significant probability is smaller than 5%. It implies the distributions are distinguishable.

3.5.1.2 TWO-COMPONENT MODEL FOR THE INTRINSIC SHAPES

Because the single-component models with Gaussian distributions for the intrinsic shape parameters cannot reproduce the shape distribution of the low-redshift sample, we now explore a different approach. As shown most recently by H12, a two-component model can accurately describe the axis-ratio distribution of present-day early-type galaxies over a large range in mass. One of these components is triaxial, precisely of the form used above; the other component is oblate, with a normally distributed intrinsic axis ratio, with mean b and standard deviation σ_b. Thus, we now have six parameters that describe the intrinsic shape distribution; the seventh free parameter is the fraction assigned to the oblate component (f_{ob}). The spacing of the grid we now use to search for the best-fitting model is (Δf_{ob}, ΔT, $\Delta\sigma_T$, ΔE, $\Delta\sigma_E$, Δb, $\Delta\sigma_b$)=(0.04, 0.04, 0.02, 0.01, 0.01, 0.01, 0.01).

TABLE 3.3: *Double-component fitting results for $z = 0$*

Mass	redshift(z)	f_{ob} [1]	b [2]	σ_b	T [3]	σ_T	E [4]	σ_E	P_{K-S} [5]	P_{M-W}
10.8-11.5	0.04-0.08 (SDSS)	0.20 ± 0.02 [6]	0.29 ± 0.02	0.07 ± 0.01	0.64 ± 0.06	0.08 ± 0.05	0.41 ± 0.02	0.19 ± 0.02	0.26	0.46
10.5-10.8	0.04-0.08 (SDSS)	0.56 ± 0.06	0.28 ± 0.01	0.08 ± 0.01	0.68 ± 0.12	0.08 ± 0.06	0.45 ± 0.02	0.16 ± 0.03	0.29	0.19
10.1-10.5	0.04-0.06 (SDSS)	0.72 ± 0.06	0.28 ± 0.01	0.09 ± 0.01	0.48 ± 0.08	0.08 ± 0.06	0.49 ± 0.02	0.12 ± 0.02	0.84	0.28

[1] $f_{\rm ob}$ is the fraction of the oblate component.

[2] b the intrinsic axis ratio of the oblate component and σ_b its standard deviation.

[3] T is the mean triaxiality parameter, with standard deviation $\sigma_{\rm T}$; these are set to 0 or 1 for the oblate and prolate models.

[4] E and σ_E are the ellipticity (1 minus the intrinsic short-long axis ratio) and its standard deviation.

[5] The final two columns list the K-S and M-W probabilities that the observed and best-fitting model projected axis ratio distributions are indistinguishable, for a randomly drawn realization of the model distribution with the same number of objects as the observed samples. These serve as a crude goodness-of-fit test.

[6] Uncertainties are obtained from bootstrapping.

The two-component approach results in a very good description of the observed axis ratio distributions of present-day galaxies (see Table 3.3 and Figure 3.8). The goodness-of-fit indications from the K-S and M-W statistical tests suggest that the best-fitting models provide a realistic view of the intrinsic shape distribution. Over the entire galaxy mass range, a highly triaxial ($T \sim 0.6$), yet flattened ($E \sim 0.45$), component combined with an even flatter ($b \sim 0.3$) oblate component provides a good description of the data, with little variation in these shape parameters with galaxy mass. The parameter that captures the strong mass-dependence in galaxy structure is f_{ob}, the fraction assigned to the second, oblate component: it rises from $f_{ob} = 0.20 \pm 0.02$ at high mass to $f_{ob} = 0.72 \pm 0.06$ at low mass.

These results are very similar to those presented by H12 – small differences occur due the choice of different stellar mass bins as well as a different implementation of the intrinsic variation in the shape parameters – the σ parameters – in generating the probability distributions $p(q_{model})$.

The high-redshift samples are too small to be treated with seven independent free parameters. However, given the success of the two-component model in describing the shape distribution of present-day early-type galaxies, we can use our superior knowledge of the low-redshift population to inform the model for the high-redshift population. Because each of the two components are very similar across the mass range explored here for the low-redshift sample, we assume that the same components can be used as an appropriate model to describe the higher-redshift observations. First, we use the best-fitting triaxial component for each of the three mass bins, with fixed intrinsic shape distributions, but let the oblate component vary arbitrarily. That is, the parameters b, σ_b, and f_{ob} are allowed to vary, while the others are kept fixed. The results are shown in Table 3.4 and Figure 3.8.

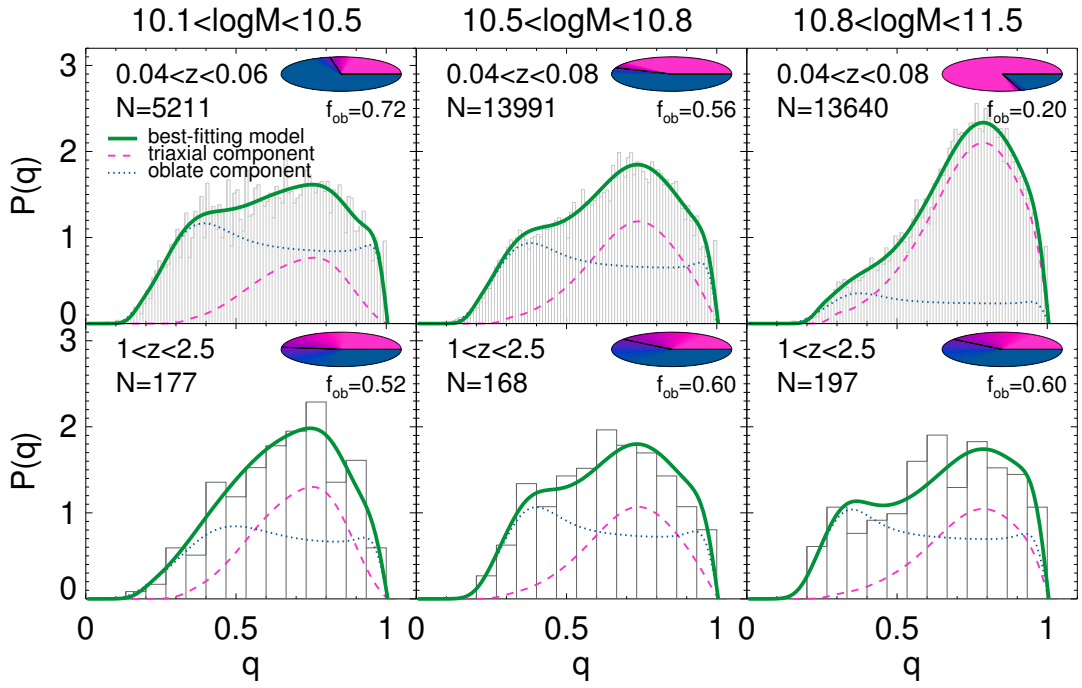

FIGURE 3.8: *Histograms show observed distributions of projected axis ratios for present-day early-type galaxies from SDSS (upper row) and at* $1 < z < 2.5$ *from CANDELS (bottom row), each in three mass bins. The green lines represent the best-fitting, two-component models with Gaussian distributions for intrinsic axis ratios as described in Section 3.5.1.2. The dashed pink lines respresent the triaxial component; the dotted blue lines represent the oblate component. The parameters characterizing the Gaussians are given in Tables 3.3 and 3.4. The small pie charts represent* f_{ob}*, the oblate fraction, and its uncertainty. For the CANDELS sample, the triaxial components are assumed to be identical to the best-fitting triaxial components found for the SDSS sample in the same mass bin. The strong dependence of the oblate fraction on galaxy mass is much weakened at* $z > 1$*. The most striking feature is the large fraction of oblate, that is, disk-like galaxies in the high-mass bin.*

Table 3.4: *Double-component fitting results for* $z = 0.6 - 2.5$

Mass	redshift(z)	oblate parameters free [1]					oblate fraction free [2]		
		f_{ob} [3]	b [4]	σ_b	P_{K-S} [5]	P_{M-W}	f_{ob}	P_{K-S}	P_{M-W}
10.8-11.5	0.6-0.8 (H12)	0.16 ± 0.18 [6]	0.33 ± 0.10	0.05 ± 0.08	0.70	0.36	0.12 ± 0.06	0.43	0.26
10.5-10.8	0.6-0.8 (H12)	0.48 ± 0.23	0.28 ± 0.07	0.05 ± 0.06	0.21	0.24	0.49 ± 0.08	0.22	0.24
10.1-10.5	0.6-0.8 (H12)	0.56 ± 0.12	0.32 ± 0.03	0.06 ± 0.04	0.87	0.36	0.51 ± 0.08	0.67	0.38
10.8-11.5	1-2.5	0.60 ± 0.24	0.27 ± 0.07	0.06 ± 0.05	0.71	0.49	0.59 ± 0.10	0.54	0.40
10.5-10.8	1-2.5	0.60 ± 0.25	0.31 ± 0.07	0.07 ± 0.03	0.87	0.37	0.53 ± 0.14	0.61	0.33
10.1-10.5	1-2.5	0.52 ± 0.24	0.34 ± 0.10	0.12 ± 0.06	0.69	0.46	0.38 ± 0.11	0.12	0.16
redshift bins of CANDELS									
10.8-11.5	0.6-0.8	1.00 ± 0.31	0.52 ± 0.13	0.25 ± 0.10	0.96	0.44	0.35 ± 0.20	0.25	0.29
10.8-11.5	0.8-1.3	0.84 ± 0.21	0.29 ± 0.05	0.06 ± 0.05	0.99	0.50	0.81 ± 0.20	0.97	0.44
10.8-11.5	1.3-1.8	0.48 ± 0.28	0.22 ± 0.08	0.05 ± 0.07	0.89	0.46	0.59 ± 0.16	0.73	0.48
10.8-11.5	1.8-2.5	1.00 ± 0.27	0.41 ± 0.09	0.20 ± 0.07	0.97	0.44	0.51 ± 0.21	0.94	0.45
10.5-10.8	0.6-0.8	0.36 ± 0.31	0.27 ± 0.10	0.05 ± 0.09	0.92	0.46	0.42 ± 0.24	0.89	0.49
10.5-10.8	0.8-1.3	1.00 ± 0.28	0.40 ± 0.07	0.16 ± 0.07	0.99	0.49	0.53 ± 0.27	0.87	0.48
10.5-10.8	1.3-1.8	0.64 ± 0.31	0.30 ± 0.10	0.05 ± 0.08	0.67	0.30	0.63 ± 0.24	0.66	0.31
10.5-10.8	1.8-2.5	0.56 ± 0.32	0.29 ± 0.09	0.05 ± 0.03	0.93	0.39	0.55 ± 0.28	0.92	0.38
10.1-10.5	0.6-0.8	0.56 ± 0.28	0.26 ± 0.09	0.05 ± 0.08	0.63	0.32	0.57 ± 0.19	0.68	0.37
10.1-10.5	0.8-1.3	0.84 ± 0.26	0.46 ± 0.08	0.17 ± 0.10	0.97	0.45	0.31 ± 0.18	0.41	0.28
10.1-10.5	1.3-1.8	0.44 ± 0.36	0.23 ± 0.12	0.19 ± 0.10	0.37	0.19	0.47 ± 0.20	0.94	0.42
10.1-10.5	1.8-2.5	0.80 ± 0.28	0.31 ± 0.10	0.05 ± 0.06	0.47	0.28	0.71 ± 0.35	0.82	0.46

[1] Fix triaxial component in the same stellar mass bins as local galaxies.

[2] Fix other parameters in the same stellar mass bins as local galaxies.

[3] $f_{\rm ob}$ is the fraction of the oblate component.

[4] b the intrinsic axis ratio of the oblate component and σ_b its standard deviation.

[5] The final two columns list the K-S and M-W probabilities that the observed and best-fitting model projected axis ratio distributions are indistinguishable, for a randomly drawn realization of the model distribution with the same number of objects as the observed samples. These serve as a crude goodness-of-fit test.

[6] Uncertainties are obtained from bootstrapping.

For the COSMOS+GEMS and combined ($1 < z < 2.5$) CANDELS samples we find that all evolution with redshift can be accounted for by evolution in f_{ob}; no significant changes in b (or σ_b) are seen. For the highest-mass galaxies ($10.8 < \log(M_*/M_\odot) < 11.5$) f_{ob} is seen to rise at $z > 1$, from $f_{ob} \sim 0.2$ at $z < 1$ to $f_{ob} = 0.60 \pm 0.24$. The large uncertainty is due to the degeneracy between b and f_{ob}: evolution in the average shape can either be accommodated by a change in the average shape of the galaxies represented by the oblate component, or by a change in the fraction of oblate galaxies. The unsubstantial changes in b (σ_b) with mass and redshift motivate us to implement a second restriction to our model: we now keep all intrinsic shape parameters at the values found for the low-z SDSS sample, and only allow f_{ob} to vary.

This restriction seems justified by the results from the goodness-of-fit tests: the predicted distribution from the best-fitting models, even with only a single free parameter (f_{ob}), do not significantly differ from the observed distributions according the the K-S and M-W tests. The results are also shown in Table 3.4 and Figure 3.9. We now find that the oblate fraction for the massive galaxies increases from 0.20 ± 0.02 at $z < 0.1$ to 0.59 ± 0.10 at $z > 1$, a highly significant (4-σ) change. For galaxies in our middle mass bin ($10.5 < \log(M_*/M_\odot) < 11.8$), f_{ob} does not change with redshift and stays at $\sim 0.5-0.6$, whereas, remarkably, f_{ob} significantly declines from 0.72 ± 0.06 to 0.38 ± 0.11 for low-mass galaxies ($10.1 < \log(M_*/M_\odot) < 10.5$). The latter was already reflected by the increased median axis ratio with redshift (see § 3.3).

This restriction seems justified by the results from the goodness-of-fit tests: the predicted distribution from the best-fitting models, even with only a single free parameter (f_{ob}), do not significantly differ from the observed distributions according the the the K-S and M-W tests. The results are also shown in Table 3.4 and Figure 3.9. We now find that the oblate fraction for the massive galaxies increases from 0.20 ± 0.02 at $z < 0.1$ to 0.59 ± 0.10 at $z > 1$, a highly significant (4-σ) change. For galaxies in our middle mass bin ($10.5 < \log(M_*/M_\odot) < 11.8$), f_{ob} does not change with redshift and stays at $\sim 0.5-0.6$, whereas, remarkably, f_{ob} significantly declines from 0.72 ± 0.06 to 0.38 ± 0.11 for low-mass galaxies ($10.1 < \log(M_*/M_\odot) < 10.5$). The latter was already reflected by the increased median axis ratio with redshift (see Section 3.3).

3.6 DISCUSSION

L^* early-type galaxies ($M_* \sim 10^{11} M_\odot$) in the present-day universe possess a wide range of intrinsic shapes: there is no single oblate, prolate, or triaxial shape that, viewed from any number of random viewing angles, can account for their projected axis ratio distribution (e.g., Lambas et al. 1992; Tremblay & Merritt 1996). We implemented two methods to describe and model this distribution. First, we showed that a single family

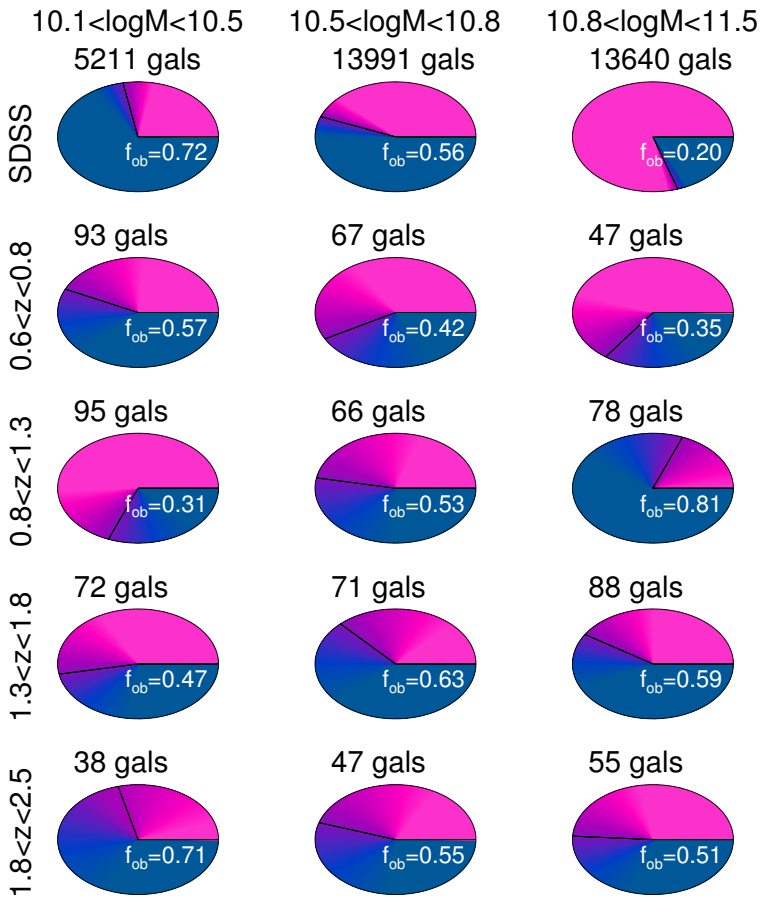

Figure 3.9: *The evolution of the oblate fraction of early-type galaxies in different mass bins. Compared to the results shown in Figure 3.8, the redshift bins at $z > 1$ are now narrower, as indicated, and the intrinsic shape distributions of both the oblate and the triaxial component are kept fixed at the values found for the present-day SDSS sample. The values of f_{ob} and their uncertainties are given in Table 3.4.*

of oblate or prolate structures with broadly distributed intrinsic axis ratios accurately captures the observed projected distribution (Section 3.4 and Figure 3.6). Second, we showed that a combination of triaxial and oblate structures, with normally distributed intrinsic shapes, works equally well. This second approach is attractive as the distinction of two components corresponds to the kinematical distinction between 'fast rotators' and 'slow rotators' (e.g., Emsellem et al. 2011). Figure 3.8 shows that a triaxial component combined with a thinner, oblate component provides a good description over a large range of galaxy masses. The strong dependence of galaxy structure on stellar mass is driven by the variation in the relative abundances of triaxial and oblate objects.

We now discuss the evolution of the intrinsic shape distribution of early-type galaxies, based on our analysis presented in Section 3.3, 3.4, and 3.5.

3.6.1 INCREASED INCIDENCE OF DISK-LIKE, MASSIVE EARLY-TYPE GALAXIES AT $z > 1$

The cumulative distributions of projected axis ratios of L^* early-type galaxies at $z > 1$ and at the present-day show that these were on average flatter in the past (Section 3.3; Figure 3.5). Our parameterized modeling approach presented Section 3.5.1.2 interprets this as a change in the fraction of the oblate component, from 0.20 ± 0.02 at $z < 0.1$ to 0.59 ± 0.10 at $z > 1$.

Because the $z > 1$ sample is too small to directly distinguish what structural family the galaxies belong to, we consider independent evidence for our interpretation that the $z > 1$ population largely consists of flat, oblate objects. At the present day, flatness is associated with rotation (e.g., van den Bosch et al. 2008; Emsellem et al. 2011), but so far such kinematic evidence has not been extended beyond $z \sim 1$ (van der Wel & van der Marel 2008). The best direct evidence for our interpretation that flat galaxies in our sample are indeed disk-like in structure is that the stellar surface mass density (middle panel of Figure 3.10) and the surface brightness (bottom panel of Figure 3.10) are larger for galaxies with small projected axis ratios. This is expected in case the flat galaxies are edge-on and oblate, but not if they are edge-on and prolate. In the latter case, the flattest galaxies should have the smallest surface brightness. We note that these considerations are only valid for transparent, that is, dust-poor, stellar systems. This assumption is supported by the observation that the rest-frame $V-J$ color does not significantly change with projected axis ratio, implying little variation in dust attenuation with inclination and, thus, a low dust content. The lack of star formation activity in these objects combined with their low dust content indicate that our sample consists of galaxies with smooth light profiles, and is therefore comparable to a morphologically classified sample of early-type galaxies based on visual inspection of images.

Further direct evidence of prominent disks in high-redshift early-type galaxies comes from two-dimensional bulge-disk decompositions (Stockton et al. 2006, 2008; McGrath et al. 2008; van der Wel et al. 2011; Bruce et al. 2012)

Based on these independent lines of evidence, we conclude that at $z > 1$ a substantially larger fraction of L^* early-type galaxies are disk-like than at $z < 1$. This evolution in structure coincides with evolution in size (e.g., Zirm et al. 2007; Toft et al. 2007; van Dokkum et al. 2008; van der Wel et al. 2008; Newman et al. 2012). Van der Wel et al. (2013a, in preparation) showed that the number density of small ($\lesssim$ 2kpc) early-type

galaxies dramatically decreases between $z \sim 2$ and the present day (also see Cassata et al. 2011, 2013). These early types are, as we have shown here, commonly disk-like, such that we may conclude that individual galaxies evolve from small and disk-like at $z \sim 2$ to large and round at $z \sim 0$. The evolution of size and internal structure could be driven by a single process, and merging is usually considered to be the most plausible process (e.g., Robaina et al. 2010; Man et al. 2012; Newman et al. 2012). Major merging and more smooth growth in mass through accretion and disruption of satellites can account for the disappearance of prominent disks in L^* early types at $z \sim 2$, and the observation that the most massive galaxies in the present-day universe do not host disks (vdW09).

In addition to the growth of individual galaxies, evolution in the population is driven by the strong increase in the number density of early-type galaxies between $z \sim 2$ and the present (e.g., Bell et al. 2004; Faber et al. 2007; Brammer et al. 2011). From $z = 2$ to $z = 1$ the fraction of triaxial galaxies increases, but this cannot be the result of the formation of 'new' early-type galaxies in the form of triaxial systems from already-formed early-type galaxies. The absolute number densities of oblate and triaxial systems both increase over that time span, and we suggest that all 'new' early types start out as compact and disk-like and subsequently evolve into larger, more triaxial systems (e.g., Naab et al. 2009; Oser et al. 2012). This suggestion is motivated by the notion that the immediate progenitors of 'new' early-type galaxies will be gas rich and star-forming, creating suitable circumstances for the formation of disks (see below), and by the notion that it is implausible that round, triaxial systems evolve into disk-like systems in the absence of star formation. At $z < 1$ a natural balance is established between the addition of 'new', disk-like early types and the gradual formation of triaxial systems, resulting in an almost unchanging, but strongly varied mix of intrinsic structures, as discussed by H12.

In the scenario described above, galaxies in which star formation is truncated retain the disk-like structure of their presumed, star-forming progenitors. A full discussion of the transition process is beyond the scope of this chapter, but it is important to point out that while newly formed early-type galaxies retain disk-like properties, their light (and stellar mass) distributions are more centrally concentrated than those of equally massive star-forming galaxies (e.g., Toft et al. 2009; Wuyts et al. 2011a; Bell et al. 2012). This implies that a substantial increase in the central stellar density occurs before or at the time of transition. A centrally concentrated starburst fueled by a gas-rich merger is one possible mechanism to produce bulge-like bodies (e.g., Khochfar & Silk 2006a). More recently, violent disk instabilities in a gas-rich galaxy have been argued to produce clumps that may migrate to the center on a short time scale, quickly creating a dense stellar body (Dekel et al. 2009; Ceverino et al. 2010; Guo et al. 2012). Whether the gas content of the resulting, dense, disk-like, but non-star-forming, galaxy has been heated and removed (e.g., Hopkins et al. 2008) or merely stabilized (e.g., Martig et al. 2009;

Ceverino et al. 2012) is still debated.

3.6.2 DECREASED INCIDENCE OF DISK-LIKE, LOW-MASS EARLY-TYPE GALAXIES AT $z > 1$

Sub-L^* early-type galaxies ($M_* \sim 10^{10} M_\odot$) in the local universe are most often oblate and disk-like. The comparison with the cumulative axis ratio distributions of such objects at $z > 1$ tells us that these were less disk-like (see Figure 3.5). This may appear to be at odds with the results discussed above, that is, that massive early types were more disk-like at $z > 1$.

Our interpretation of this 3-σ effect remains largely speculative. Low-mass early-type galaxies in the present day can be surmised to be disk-like for the simple reason that their star-forming progenitors are also disk-like. Star formation may stop either due to some internal process or due to environmental effects such as ram-pressure stripping. In the latter case the structure of the stellar disk will remain intact, leading to a very flat early-type galaxy. At $z \sim 2$ the fraction of satellite galaxies in this mass range is predicted to be negligible, whereas among the present-day population satellite galaxies make up 30% – 40% of the total (e.g., van den Bosch et al. 2008). Indeed, the axis ratio distributions of present-day centrals and satellites are significantly different (van der Wel et al. 2010), but even the present-day centrals are not as round as their $z > 1$ counterparts (also see Vulcani et al. 2011),. We suggest that the low-mass early-type galaxies at $z > 1$ are not very disk-like, simply because their star-forming progenitors were not disk-like at that epoch: van der Wel et al. (2013b, in preparation) showed that low-mass ($M_* < M_\odot^{10}$) star-forming galaxies at $z > 1$ had not yet attained stable, rotating structures, like they have at later epochs. Whether this is related remains to be seen and hinges on our general lack of understanding of how star-forming galaxies are transformed into passive, early-type galaxies.

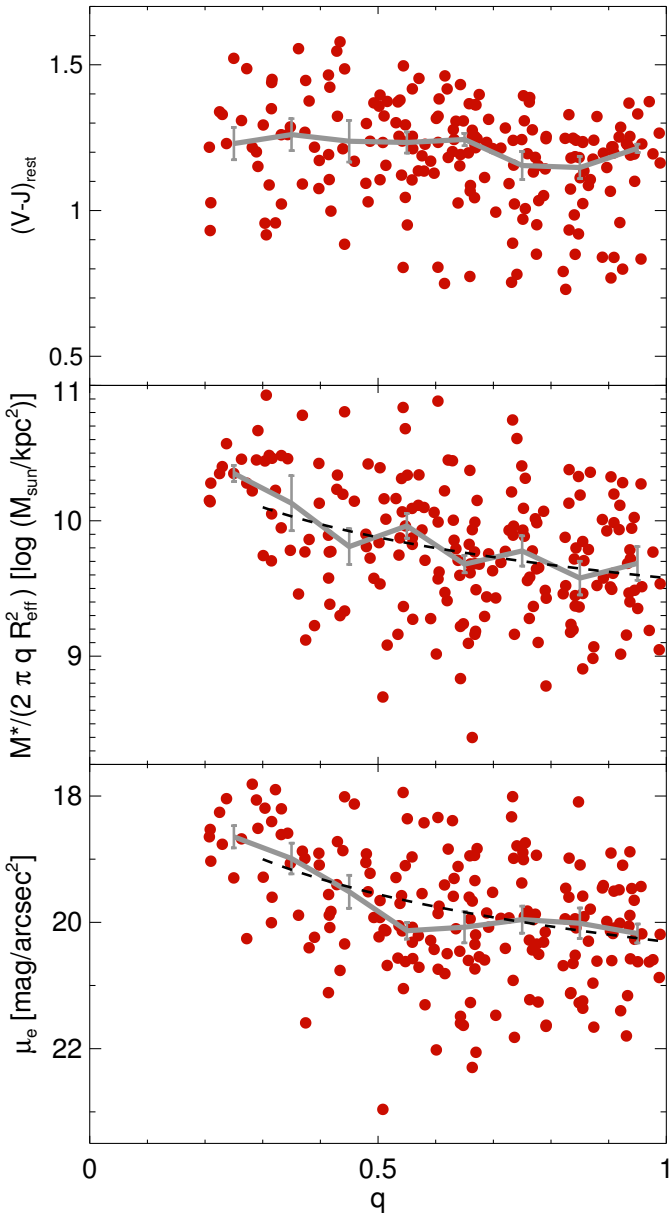

Figure 3.10: *The projected axis ratio vs. rest-frame $V - J$ color, mass surface density, and surface brightness for the early-type galaxies selected from CANDELS at redshifts* $1 < z < 2.5$ *and more massive than* $\log(M_*/M_\odot) > 10.8$. *The gray lines with error bars from bootstrapping represent running medians. The lack of a trend in the top panel suggests that these galaxies contain little or no dust; otherwise, galaxies with small axis ratios, that is, those viewed edge-on, would be expected to have redder colors. The increased surface mass density and surface brightness of the small-axis ratio galaxies (bottom two panels) suggest that these galaxies are oblate rather than prolate; the dashed black lines are the expected projected surface brightness and density for an oblate model, with intrinsic axis ratio* $E = 0.61$, *which is the best-fitting value from the single-component model for this sample (Table 3.2).*

3.7 SUMMARY

Projected axis ratio measurements from HST/WFC3 F160W imaging from CANDELS of 880 early-type galaxies at redshifts $1 < z < 2.5$, complete down to a stellar mass of $\log(M_*/M_\odot) = 10$ over the whole redshift range, are used to reconstruct and model their intrinsic shapes. The sample is selected by low star-formation activity on the basis of $U-V$ and $V-J$ rest-frame colors (see Figure 3.2, and we demonstrate that these galaxies are dust-poor and transparent: those with flat projected shapes have the same colors as those with round shapes (see Figure 3.10, top panel). In addition, the increased surface mass densities and surface brightness of flat galaxies (Figure 3.10, bottom two panels) suggest that flattening is associated with a disk-like internal structure; prolate galaxies would have lower surface densities when viewed edge-on. Therefore, we conclude that our sample consists of genuine early types, comparable to samples based on visual morphological classification. We compare the shape distribution of this sample with the shape distribution of early-type at low redshift ($0.04 < z < 0.08$) selected in a similar manner from the SDSS.

Similar to their present-day counterparts, the $z > 1$ early-type galaxies show a large variety in intrinsic shape; even at a fixed mass, the projected axis ratio distributions cannot be explained by random projection of a set of galaxies with very similar intrinsic shapes. We demonstrated this in two ways by assuming that all galaxies are oblate (or prolate): first, an analytical approximation to deproject the observed axis ratio distributions implies that a very broad range in intrinsic shapes is required (Section 3.4 and Figure 3.6); second, we show that randomly projecting a set of objects with a Gaussian distribution of intrinsic axis ratios cannot match the observed, projected shape distribution (Section 3.5.1.1 and Figure 3.7).

As was demonstrated for present-day early-type galaxies and up to $z \sim 1$, a two-population model can accurately describe the projected axis ratio distributions. We now extend this to $z = 2.5$. This model, inferred from fitting the axis ratio distribution of the low-redshift sample (Section 3.5.1.2 and Figure 3.8), consists of a triaxial, fairly round population combined with a flat ($c/a \sim 0.3$) oblate population. For present-day early-type galaxies the oblate fraction strongly depends on galaxy mass, but at $z > 1$ this trend is not seen over the stellar mass range explored here ($10 < \log(M_*/M_\odot) < 11.3$). This is mostly the result of strong evolution in the oblate fraction among high-mass early-type galaxies: for galaxies with mass $\log(M_*/M_\odot) > 10.8$ the oblate fraction increases from 0.20 ± 0.02 at the present day to 0.59 ± 0.10 at $1 < z < 2.5$. Conversely, we find that the oblate fraction decreases with redshift for low-mass early-type galaxies ($\log(M_*/M_\odot) < 10.5$), from 0.72 ± 0.06 to 0.38 ± 0.11. These results are based on the assumption that the intrinsic shapes of the triaxial and oblate population do not evolve with redshift. We refer to Section 3.5.1.2 for a justification of this assumption and a

demonstration that our results and interpretation do not depend on it.

The decreased prevalence of disk-like systems and larger galaxy sizes at lower redshifts point to a scenario in which classical elliptical galaxies gradually emerge over time through merging and the accretion of satellites, at the expense of the destruction of pre-existing disks. Definitive evidence for the disk-like structure of massive early-type galaxies at $z \sim 2$ should eventually be provided by kinematic evidence for rotation in the stellar body. We speculate that the decreased incidence of disks at early cosmic times among low-mass early-type galaxies can be attributed to two factors: low-mass, star-forming progenitors at $z > 1$ were not settled into stable disks to the same degree as at later cosmic times, and the stripping of gas from satellite galaxies is an increasingly important process at lower redshifts. We refer to Section 3.6.2 for a discussion.

A joint analysis of shapes, sizes, and Sérsic indices for late- and early-type galaxies, will provide further insight into the intrinsic structure of high-redshift galaxies, and allow for more constrained deprojection and model construction approaches. Further improvements will be provided by the extension of the analysis to the full CANDELS data set, drawing samples from all five fields instead of the two fields used here; at the moment we are still limited by small number statistics at $z \sim 2$ and above.

4

On bimodality of the Galaxy Population

We assemble multi-wavelength photometry for the full SDSS spectroscopic galaxy sample, drawing from the SDSS, 2MASS, and WISE surveys, covering the wavelength range 0.4-22 μm. We use the latest modeling techniques (MAGPHYS, da Cunha et al. 2008) to estimate stellar masses and star formation rates. The addition of photometry at $> 1\mu$m improves these measurements as compared to previous SDSS-based estimates. The newly measured star formation rates allow us to test methods to separate early-type (passive) from late-type galaxies (star-forming) galaxies. The rest-frame color-color selection technique, which is widely used at high redshift is equally successful in separating the two types as a selection by specific star formation rate. Furthermore, we show that selection criteria based on optical emission line ratios (from SDSS) and 12 μm/3.4 μm luminosity ratios from WISE also result in the separation of the two types, with similar fidelity.

This chapter is based on Chang et al. (2014), in preparation.

4.1 INTRODUCTION

We need the knowledge of the present-day galaxy population, such as stellar masses and star formation rates (SFRs), to investigate galaxy evolution with cosmic time. Furthermore, the techniques and methods applied to high-redshift galaxies, which less information is available, are require to be tested at low redshift. Specifically, in this thesis, we used the color-color (*urz*) techniques. It is important to know how well it works compared to a real star-formation-based selection (sSFR).

The stellar mass and SFR measurements are widely used as a benchmark from Brinchmann et al. (2004) for the spectroscopic galaxy sample of the SDSS. That is, stellar masses are from Sloan Digital Sky Survey (SDSS) photometry (0.4-0.9 μm), and SFRs are from the spectra (emission lines).

Here, an improved and complementary benchmark is applied: stellar masses are from photometry over a much larger wavelength range (0.4-22 μm). Therefore, not only the stellar light ($< 5\mu$m) but also the dust and polycyclic aromatic hydrocarbon (PAH) regime (5-22 μm) are considered. This is made possible by the Two Micron All Sky Survey (2MASS, Skrutskie et al. 2006) and the Wide-field Infrared Survey Explorer (WISE, Wright et al. 2010) all sky survey.

We use the Multi-wavelength Analysis of Galaxy Physical Properties (MAGPHYS, da Cunha et al. 2008), which uses latest stellar population models, fits the entire spectral energy distribution (SED), consistently treating dust absorption and at short wavelengths and dust emission at long wavelengths. Stellar mass is improved with respect to Brinchmann et al. (2004) because stellar light at wavelength greater than 1 μm is used and extinction is not a problem here. The inclusion of the non-stellar wavelength regime gives us an estimate of the SFR (essentially using PAH and warm dust as tracers). This estimate is complementary to SFRs based on emission lines in Brinchmann et al. (2004) and SFRs based on UV in Salim et al. (2007).

Our results contains stellar mass and SFR estimates for 800,000s of galaxies, which provide the best view to date of the bimodality of galaxy population. This allows us to probe the fidelity of the different approaches to separate the galaxy population into passive (early-type) galaxies and star-forming (late-type) galaxies, which include, for example, color selection techniques (used in this thesis) and emission line criteria.

In Section 2, the SDSS spectroscopic selected data, and the matched 2MASS and WISE data will be described. In Section 3, MAGPHYS and the method to acquire stellar masses, SFR, and rest-frame colors will be introduced. In Section 4, we will compare the stellar mass and SFR between our and previous values for stellar masses, and star formation rates, and investigate the bimodality of the galaxy population. In Section 5,

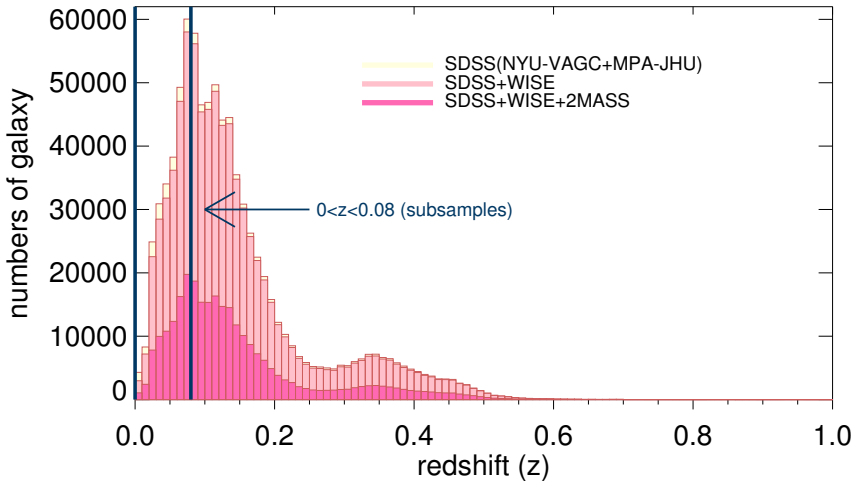

FIGURE 4.1: *Numbers of galaxy in the SDSS, SDSS+WISE, and SDSS+WISE+2MASS sample in different redshift. In the original spectroscopic NYU-VAGC and MPA-JHU catalogs, there are 854,891 galaxies (yellow). 822,499 galaxies (pink) have matches in the WISE catalog, and 275,667 (deep pink) galaxies have 2MASS measurement. In this thesis, we show the results for subsamples (blue cut):* $0 < z < 0.08$.

we will demonstrate the richness of the newly constructed data set by examining several features of the galaxy population in detail.

4.2 SAMPLE AND PHOTOMETRY

We use a SDSS spectroscopic galaxy sample, compiled in the New York University Value-Added Galaxy Catalog (NYU-VAGC, Blanton et al. 2005; Adelman-McCarthy et al. 2008; Padmanabhan et al. 2008) [1], which contained 858,365 galaxies with good measurement of redshift (`OBJTYPE`=GALAXY, `Zwarning`=0). We match the NYU-VAGC catalog with MPA/JHU catalog [2] to acquire the emission line measurements and previous values for stellar masses, SFR, and sSFR. The stellar masses are based on fits to the SDSS *ugriz* photometry following the philosophy of Kauffmann et al. (2003a); Salim et al. (2007) and the updated version[3]. The SFRs are based on Brinchmann et al. (2004) who use emission line luminosities.

We use all available surveys that contains photometry for the majority of the spectro-

[1] http://sdss.physics.nyu.edu/vagc/
[2] http://www.mpa-garching.mpg.de/SDSS/DR7/
[3] http://home.strw.leidenuniv.nl/ jarle/SDSS/

scopic sample: a SDSS selected sample of 854,891 galaxies from intersection of NYU-VAGC and MPA-JHU catalog, with WISE, and the Extended Source Catalog (XSC) of the 2MASS. We found 822,499 matches in the WISE catalog and 275,667 of them in the 2MASS catalogs. We will focus on the nearby subsample at $0 < z < 0.08$. The analysis of the full sample is underway and the full sample will be included in our final data product. In the subsample, there are 234,279 galaxies in the SDSS+WISE catalog, and 80,421 galaxies in the SDSS+WISE+2MASS catalog. For, SDSS, the magnitude limits (95% detection repeatability for point sources) are 22.0, 22.2, 22.2, 21.3, and 20.5 for *u*-, *g*-, *r*-, *i*-, and *z*- bands. For XSC of 2MASS, the 10-σ magnitude limits are 15.0, 14.3, and 13.5 for *J*-, *H*-, and K_s- band. For WISE, the 5-σ limits of point source sensitivities are about 0.08, 0.11, 1, and 6 mJy, and the angular resolution are 6.1", 6.4", 6.5", and 12.0" in the four bands (W1: 3.4 μm, W2: 4.6 μm, W3: 12 μm, and W4: 22 μm).

We will use fluxes in each wavelength from these three surveys as input for SED fitting. For SDSS flux, we use `MODELFLUX`, which is a linear combination of the total flux of the best fitting exponential and de Vaucouleurs profile in each band. For 2MASS flux, we use `J_M_FE`, `H_M_FE`, and `K_M_FE`, which are fluxes measured within elliptical apertures spanning 2.5 times the Kron radius. For WISE flux, we use `W1mpro`, `W2mpro`, `W3mpro`, and `W4mpro`, which are the integrated fluxes based on a two-dimensional intrinsic light distribution model that is created by simultaneously fitting to the images from all four bands, given the different PSFs and automatically deblending neighboring sources. While the flux measurement method varies from surveys to survey they all aim at measuring the total flux, taking the extent and shape of the light distributions of individual objects into account.

We recalculated the galactic extinction from the the `EXTINCTION` in SDSS (Schlegel et al. 1998) to the values suggested by Schlafly & Finkbeiner (2011) ($R_V = 3.1$ in Table 6) and adopted 0.2 variation as estimated by Schlafly et al. (2010) (also see Yuan et al. 2013). We also apply the recalculation for 2MASS fluxes.

Moreover, we add 0.05, 0.02, 0.02, 0.02, 0.02 of the fluxes to the error for *ugriz*-bands of SDSS, 0.05, 0.05, 0.05 of the fluxes for the JHK_s-bands of 2MASS, and 0.1, 0.1, 0.1 of the fluxes for the four bands of WISE. This prevents small systematic errors in the photometry from dominating the outcome of our goodness-of-fit based method to estimate stellar masses and other parameters.

4.3 FITTING METHOD

We fit the photometric SED for $0 < z < 0.08$ subsample by using MAGPHYS (da Cunha et al. 2008, 2012) [1]. It computes the energy distribution evolution of stellar populations in galaxies using the latest version of the population synthesis model of Bruzual & Charlot (2003). MAGPHYS contains 50,000 stellar population spectra (optical photometry libraries) and 50,000 dust emission spectra (infrared photometry libraries). The optical templates created assuming the property that stellar population with any star formation history can be explained in a series of instantaneous bursts. The SED of a galaxy is computed by adding the individual spectra of all simple stellar populations, weighted by the SFR over time. The infrared templates describe emission by dust. The total dust luminosity over 3 to 1000 μm has components of emission from PAHs, the mid-infrared continuum from hot dust, the emission from warm dust (30 to 60 K) in thermal equilibrium, and the emission from cold dust (15 to 25 K) in thermal equilibrium. The ISM of galaxies in the model contains the ambient (diffuse) interstellar medium and the star-forming regions (birth clouds). Because stars are born in dense molecular clouds which dissipate typically after 10^7 years, the emission from young stars and light from may absorbed by dust in the birth clouds and the ambient ISM, while old stars propagates only through the diffuse ISM. MAGPHYS accounts for different attenuation of line and continuum emission, and compute the total energy absorbed by both dust in the birth clouds and in the ambient ISM requiring energy balance between absorption and emission.

To find the best-fitting templates in an efficient way for about one millions galaxies, we select templates before starting fitting fitting process. We choose about stellar templates by $g - i$ selection: $|(g-i)_{model} - (g-i)_{data}| < 0.1 + \sigma[(g-i)_{data}]$, where $(g-i)_{model}$ is the $g - i$ observed color of MAGPHYS template, $(g-i)_{data}$ is the observed color of the data, and $\sigma[(g-i)_{data}$ is the standard deviation of $(g-i)_{data}$. This selection typically eliminates more than 80% of all 50,000 available templates and use 1000 out of 50,000 randomly selected infrared templates.

The differences between stellar masses and star formation rates are based this reduced template library and the full library are small, with no systematic effect: the median is -0.0005 for the difference of stellar masses and 0.0001 for the difference of the sSFRs, as shown in Figure 4.2. In Figure 4.2, the standard deviation is within the measurement uncertainties. For sSFR>-10.6 $year^{-1}$ galaxies (late types), the standard deviation is 0.1087 for the difference of stellar masses and 0.1829 for the difference of the sSFRs.

We use the following approach to derive the rest-frame magnitudes and colors for each of the galaxies in the sample. First, rest-frame and observed magnitude for the templates

[1] http://www.iap.fr/magphys/magphys/MAGPHYS.html

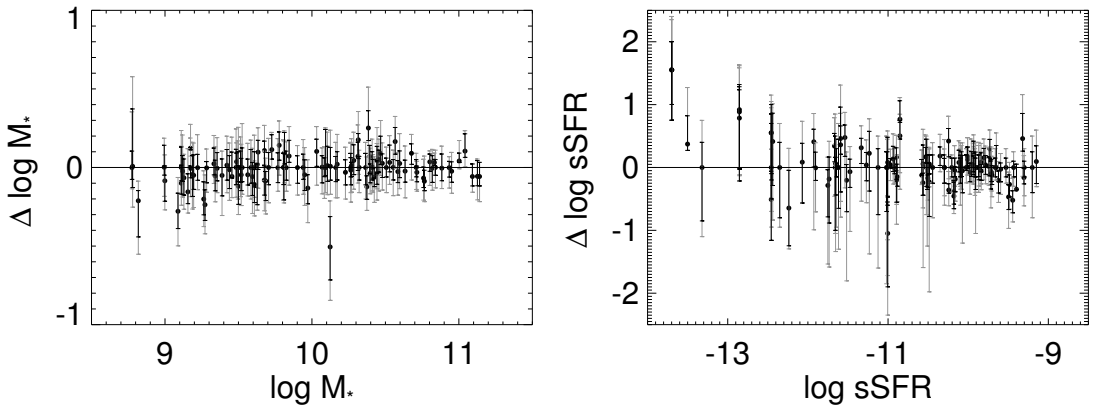

FIGURE 4.2: *Stellar masses and SFRs comparison from the templates we use and the original MAGPHYS templates. The x axes are the stellar masses and SFRs derived from the original MAGPHYS templates. The y axes shows the difference between the libraries we choose and the original MAGPHYS libraries. We use selected optical templates ($|(g-i)_{model} - (g-i)_{data}| < 0.1 + \sigma[(g-i)_{data}]$) and 1,000 random infrared templates to derive the stellar masses and SFRs. The black error bar is 68% value and the gray error bar is 95% value. It shows the templates we use are good as the original templates.*

are calculated. We use their linear relation to fit $A(z)$ and $B(z)$ in:
$m_0 = m_{obs1} + A(z) \times (m_{obs1} - m_{obs2}) + B(z)$, where m_0 is the rest-frame magnitude in the template, m_{obs1} and m_{obs2} are the magnitudes in the observed frame at redshift z that are closest in wavelength to the rest-frame filter (also see Holden et al. 2012). For each galaxy in the sample, we use the observed magnitude and the values of $A(z)$ and $B(z)$ derived as described above, to get rest-frame magnitude.

4.4 COMPARISON WITH PREVIOUS MEASUREMENTS

In Figure 4.3, we show the stellar mass and SFR distribution of our sample. This can be directly compared to Figure 17 and Figure 24 in Brinchmann et al. (2004) and Figure 15. in Salim et al. (2007). The star-forming sequence (late-type galaxies) in the upper left part of Figure 4.3, and passive galaxies (early-type galaxies), usually called the Red Sequence is in the lower right part of Figure 4.3. Selection effects may cause the absence of galaxies with low masses and SFRs, and issue that we will address in a follow-up study.

In Figure 4.4, we compare our masses and SFRs with the values in MPA-JHU catalog. The systematic difference (median) between two results is -0.0070 for stellar masses,

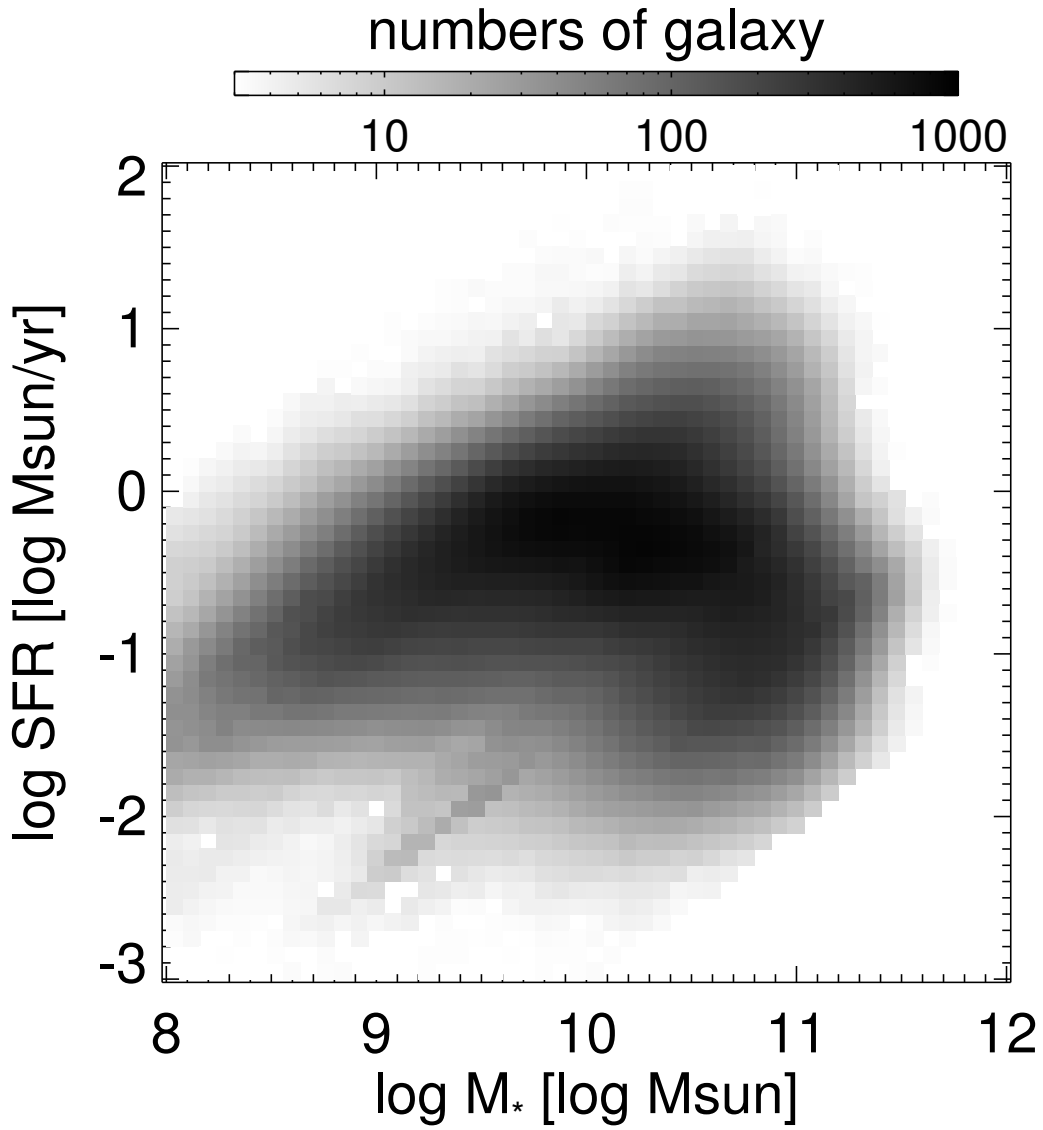

Figure 4.3: *Stellar mass vs. SFR. The grey scale corresponds to the numbers of galaxies in each bin.*

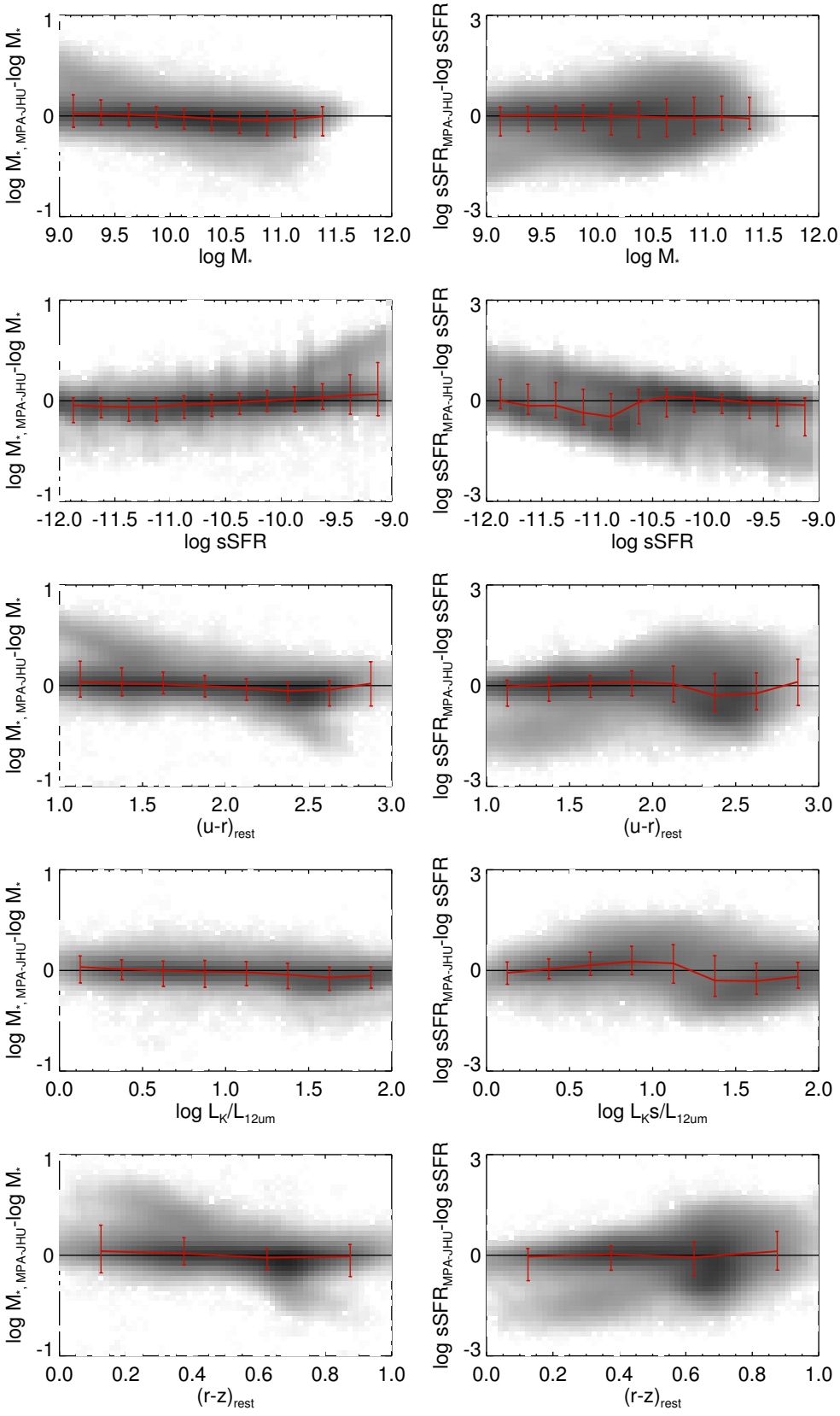

FIGURE 4.4: *MAGPHYS output vs. MPA-JHU catalog comparison. The left plots are the differences of stellar mass and the left plots are the differences of sSFR. The axes from the top to the bottom are stellar mass, SFR,* $(u-r)_{rest}$*, and* $L_k/L_{12\mu m}$*, respectively.*

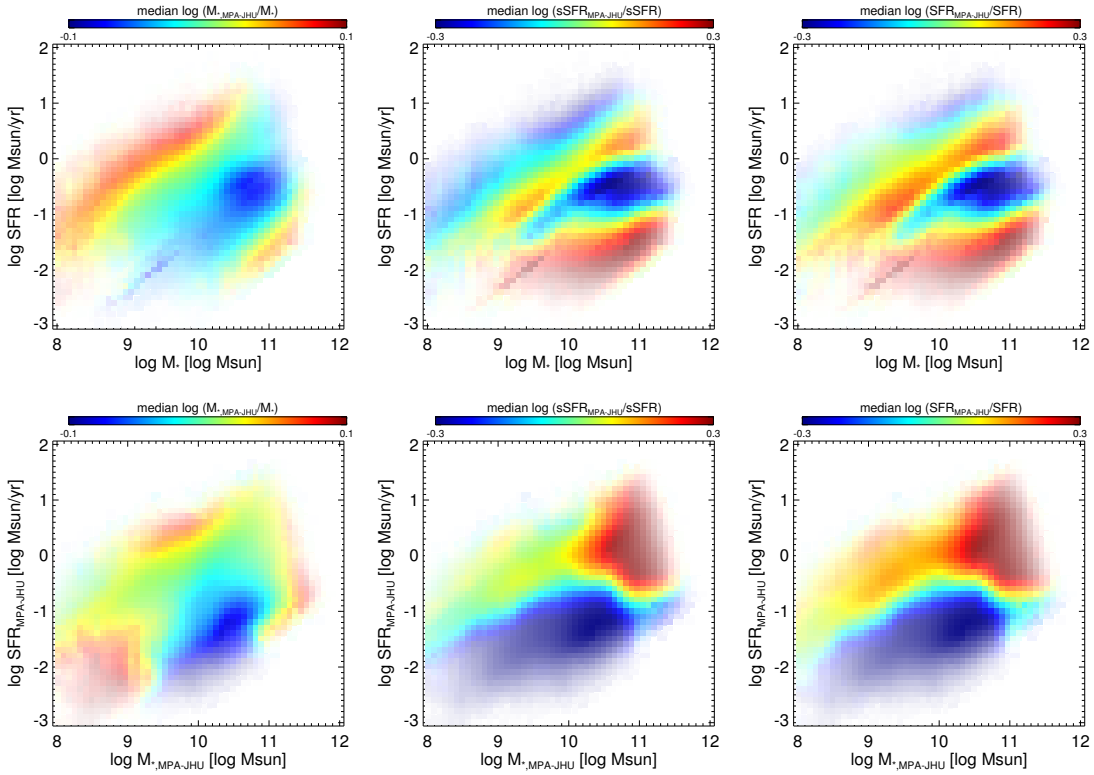

FIGURE 4.5: *The stellar mass, sSFR, and SFR differences between MPA-JHU catalog and MAGPHYS output in the stellar vs. SFR plot. (upper): The data in the axes is our MAGPHYS output. (lower): The data in the axes is from MPA-JHU catalog. The MPA-JHU value may underestimates SFR for massive star-forming galaxies due to lack of dust information.*

and -0.0105 for sSFR. The scatter is consistent with the measurement uncertainties. For sSFR>-10.6 $year^{-1}$ galaxies (late types), the scatter (standard deviation) is 0.1542 for the difference of stellar masses and 0.4162 for the difference of the sSFRs. In Figure 4.4, there are several systematic trends with stellar mass, sSFR, rest-frame colors, and $L_k/L_{12\mu m}$ ratio. Figure 4.5 illustrates the origin of these systematic trends more clearly. We have higher sSFR for high sSFR galaxies, but lower sSFR for low sSFR galaxies. Our SFR estimates for high-mass galaxies are higher than the MPA-JHU value. This may the result of our use of IR tracers of obscured star formation. For low mass galaxies the SFR estimates agree, and the difference is sSFR is due to the difference between the stellar mass estimates. The differences for passive galaxies are caused by a systematic overestimation of the extinction and dust mass by MAGPHYS. We are planning to implement an empirically motivated prior to force MAGPHYS to prefer less dusty solutions for passive galaxies.

4.5 A NEW VIEW ON THE BIMODALITY OF THE GALAXY POPULATION

The richness of the assembled data set (with stellar masses, rest-frame colors, emission line ratios, and infrared luminosities for ~200,000 galaxies) provide us with a new and improved view on the physical properties of the local population, and the well-known bimodality in star formation activity in particular.

Here we compare different methods to identify passive (early-type) and star-forming (late-type) galaxies. First, the rest-frame color-color diagram (*urz* in SDSS/*UVJ* at high redshifts) separate galaxies by the 4000 Å breaks of early-type galaxies and dust reddening of obscured late-type galaxies (e.g., Williams et al. 2009; Whitaker et al. 2011). The BPT diagram (e.g., Baldwin et al. 1981; Kewley et al. 2001; Kauffmann et al. 2003b; Kewley et al. 2006) separate star-forming (late-type) galaxies, Seyferts, and low-ionization nuclear emission-line regions (LINERs) by age, mass, metallicity (e.g., log([NII]/Hα)), and hardness of the ionizing radiation (e.g., log([OIII]/Hβ). We will show a series of plot for (a) SFR versus stellar mass, (b) rest-frame $u-r$ vs. $r-z$ (*urz* plot), and (c) log([OIII]/Hβ) versus log([NII]/Hα) (BPT diagram). For all the plots, the opacity shows the number of galaxies (N_{min} = 3; N_{max} = 1000) in log scale. The color coding depends on the plots, and will be described in the following text and shown in the colorbar. Boxcar smoothing in two dimensions considering the uncertainties of the parameters is applied to the color coding and opacity. We only show galaxies with detected emission lines (SNR> 2 for Hα, Hβ, [NII], and [OIII]) in the BPT diagram.

In Figure 4.6, we show the bimodality of late-type and early-type galaxies in the three plots: (a) SFR versus stellar mass, (b) rest-frame *urz* plot, and (c) BPT diagram. First, we separate galaxies by sSFR= -10.6 $year^{-1}$ (solid line in the SFR versus stellar mass plot) and plot the fraction of late-type galaxies defined by $sSFR > -10.6$ $year^{-1}$ in the (b) *urz* plot and (c) BPT diagram. The early-type galaxies in the upper left region of *urz* plot shows high fraction of low star-forming activities, and the late-type galaxies in lower right diagonal track shows high fraction of star-forming activities. In the BPT diagram, late-type galaxies in the lower left part also show high fraction of high sSFR.

According to the bimodality in the *urz* plot, we separate galaxies by $(u-r)_{rest} = 2.1$ and $(u-r)_{rest} = 1.6(r-z)_{rest} + 1.1$ (solid line in the *urz* plot) in the second row. We define early-type galaxies in the upper left region and late-type galaxies in the lower right region. With the same definition, the (a) SFR versus stellar mass plot and the (c) BPT diagram shows a similar bimodality trend as in the first row. In the third row, we separate galaxies by log([OIII]/Hβ) =0.6/log([NII]/Hα)+1.3 (solid line in the BPT diagram) according to the BPT diagram. Note that the percentage of the early-type galaxies in the first two panels also include galaxies without emission lines (SNR< 2

for Hα, Hβ, [NII], and [OIII]). This definition also shows a strong bimodality in the (a) SFR versus stellar mass plot and the (b) *urz* plot. The percentage of early- (late-) types by any separation in all the plots are larger than 80%. This implies that any of the methods to separate star-forming (late-type) from passive (early-type) galaxies have a high success rate and are essentially interchangeable.

In the fourth row of Figure 4.6, the mass to light ratio in the 12 μm also shows strong bimodality in all the tree plots. The explanation for this trend is well-understood as 12 μm luminosity is known to correlate tightly with SFR (e.g., Lee et al. 2013, see the upper row in Figure 4.7). There is a tail of massive, low SFR galaxies with relatively high 12 μm luminosities. This emission is powered by evolved stars rather than young stars, and is likely in the form of PAH emission in the dust shells around (post) Asymptotic Giant Branch (AGB) Then, consider that near-infrared luminosity (e.g., 3.4 μm) tightly correlates with stellar mass (see the middle row of plots). The increased 3.4 μm luminosity for high SFR galaxies in the middle right plot can be explained by age variation in the 3.4 μm mass-to-light ratio, or possibly uncertainties in the stellar population models. Due to the correspondence between 12 μm luminosity and SFR on the one hand, and 3.4 μm luminosity and stellar mass on he other hand, we can use the 12 μm/3.4 μm luminosity ratio as an sSFR indicator (bottom panel Figure 4.7). This infrared indicator is complementary to the indicators that use optical-near infrared colors and emission line properties (shown in Figure 4.6)

4.6 Dissecting the Bi-Modal Galaxy Population

4.6.1 From Optical to Infrared Luminosity

In Figure 4.8 and 4.9, color codings shows the median of luminosity in different wavelengths. From the *g*- band to 4.5 μm we naturally see that luminosity corresponds closely with stellar mass. In additional, at a fixed mass, strongly star-forming galaxies have higher luminosities. For the *g*- band this means that the low mass-to-light ratio associated with young populations dominates over the competing effect of increased extinction. The low mass-to-light for high-SFR galaxies is also seen at near-infrared wavelengths. For example an increased SFR by a factor 10 corresponds to a factor 3 increase in 3.4 μm luminosity. We also note that at each wavelength the most luminous galaxies are found among the passive population. As expected, 12 μm and 22 μm luminosity correlate more closely with SFR than with stellar mass. At these wavelengths the most luminous galaxies are the most massive, metal-rich star-forming galaxies. Among the luminous infrared galaxies a subset has line ratios that indicate that a relevant AGN contribution.

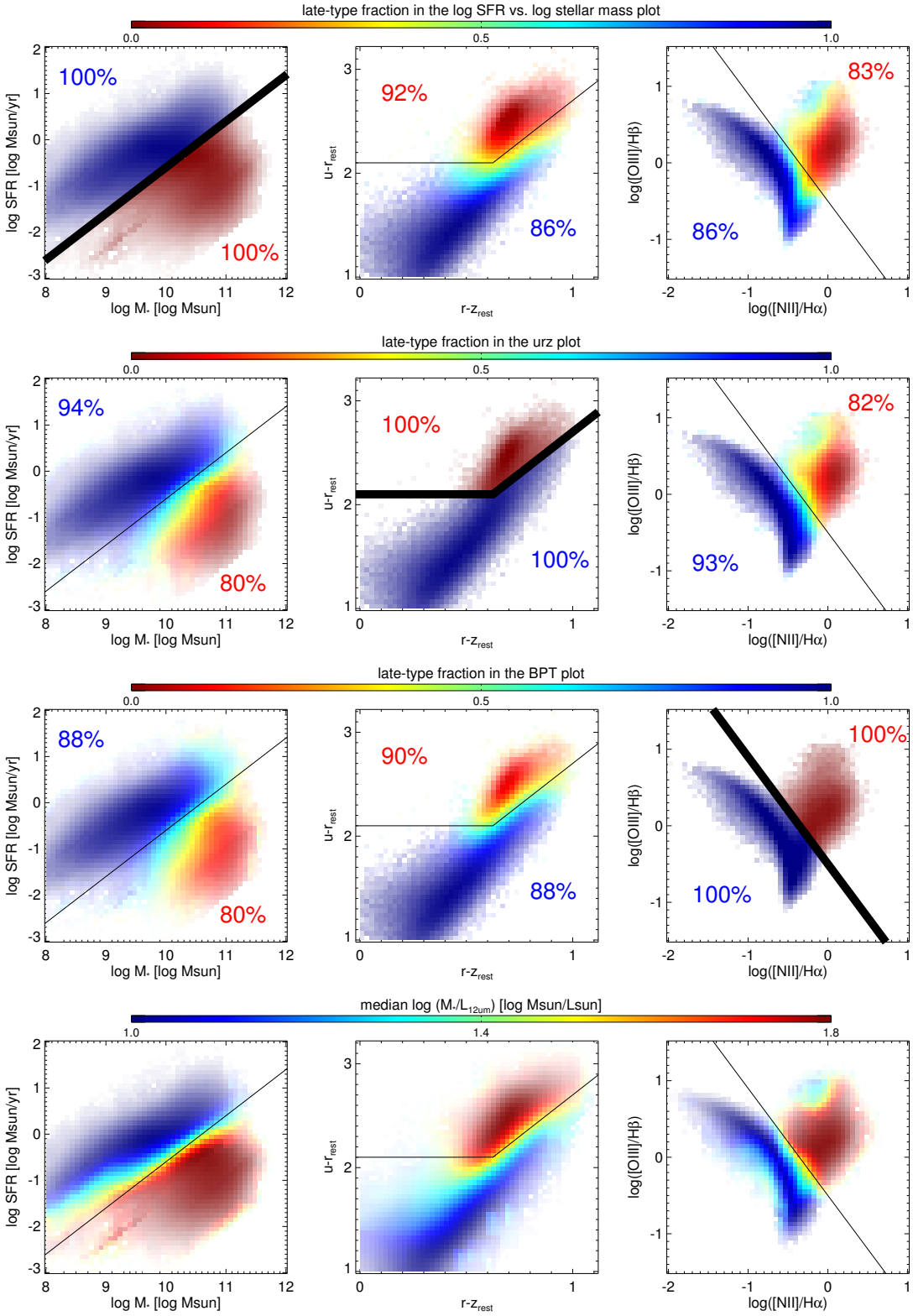

FIGURE 4.6: *The color coding is the fraction of the star-forming/early-type galaxies with different kinds of selection (thick line): (1st row) early-type:* $\log sSFR > -10.6\ year^{-1}$*; late-tyle:* $\log sSFR < -10.8\ year^{-1}$*, (2nd row) early-type:* $(u-r)_{rest} > 2.4$ *and* $(u-r)_{rest} > 1.7(r-z)_{rest} + 1.2$*; late-tyle:* $(u-r)_{rest} < 2.1$ *or* $(u-r)_{rest} < 1.6(r-z)_{rest} + 1.1$*, and (3rd row) early-type:* $\log([O\,\textsc{iii}]/H\beta) > 0.6/\log([N\,\textsc{ii}]/H\alpha)$*; late-tyle:* $\log([O\,\textsc{iii}]/H\beta) < 0.6/\log([N\,\textsc{ii}]/H\alpha)$*. The percentages of early- (late-) types by the separation (solid line in the same row) in the individual region are shown. In the (4th row), the color coding is the medium of mass to 12 μm luminosity ratio.*

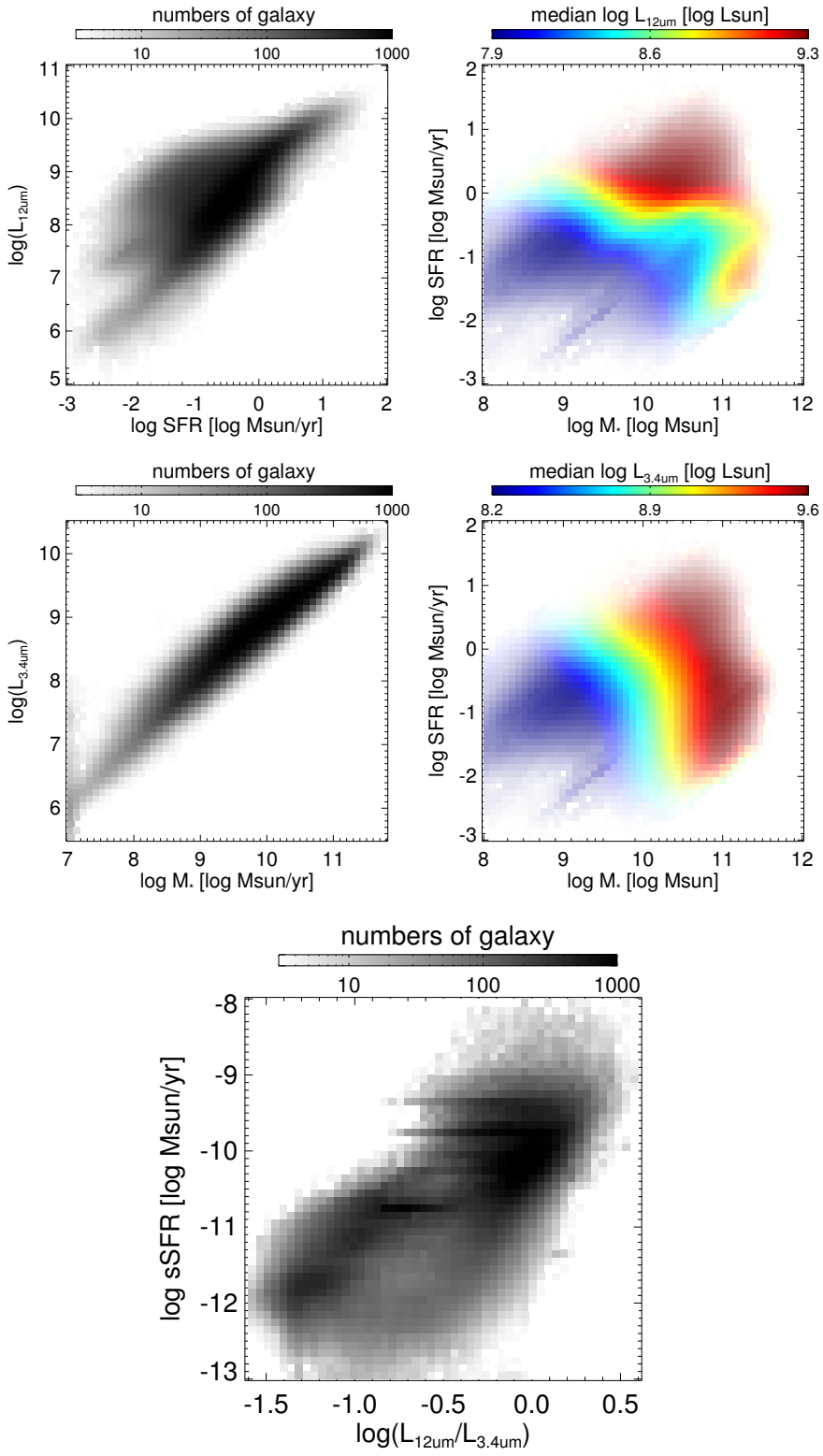

Figure 4.7: *(top left) SFR vs. 12 μm luminosity plot. (top right) mass vs. SFR plot, color coding with 12 μm luminosity. (middle left) stellar mass vs. 3.4 μm luminosity plot. (middle right) mass vs. SFR plot, color coding with 3.4 μm luminosity. (bottom) sSFR vs. Ratio of 12 μm to 3.4 μm luminosity, the grey scale corresponds to the numbers of galaxies in each bin. We show the correlation between 3.4 μm luminosity (optical band) with stellar mass, 12 μm luminosity (infrared band) with SFR, and the combined correlation between luminosity ratio and sSFR.*

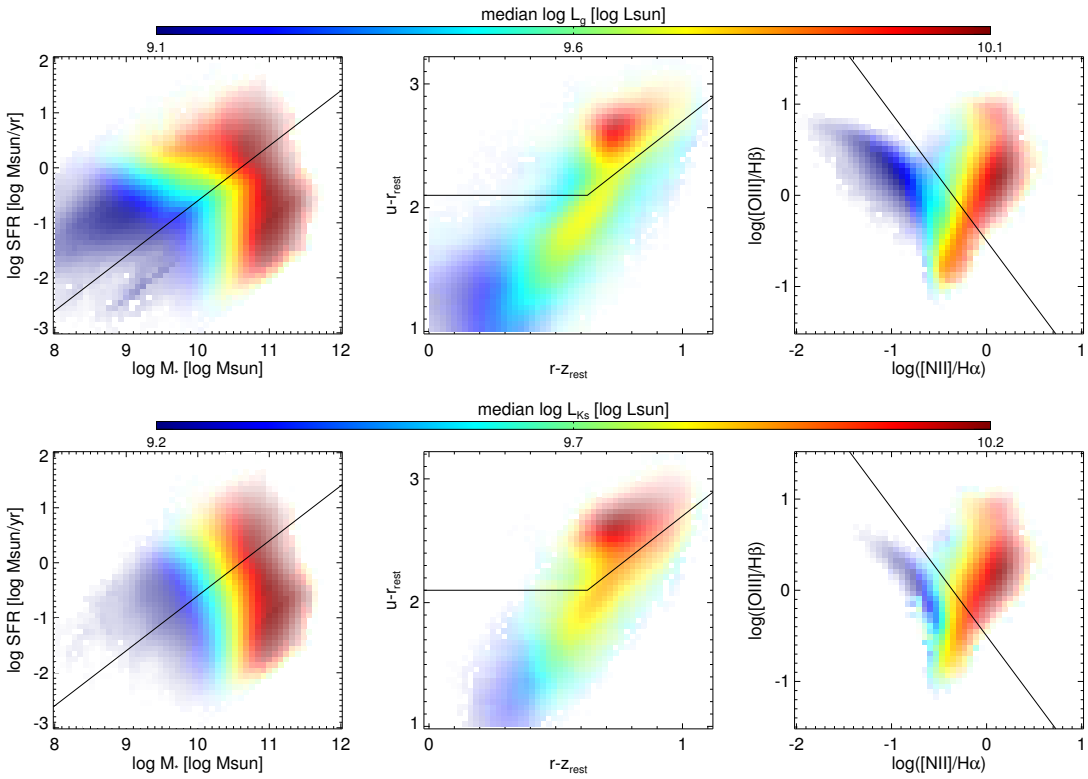

FIGURE 4.8: *The color codings are the mediums of g-band in SDSS and Ks-band in 2MASS luminosity within each bin. Low mass galaxies are not available in the 2MASS data.*

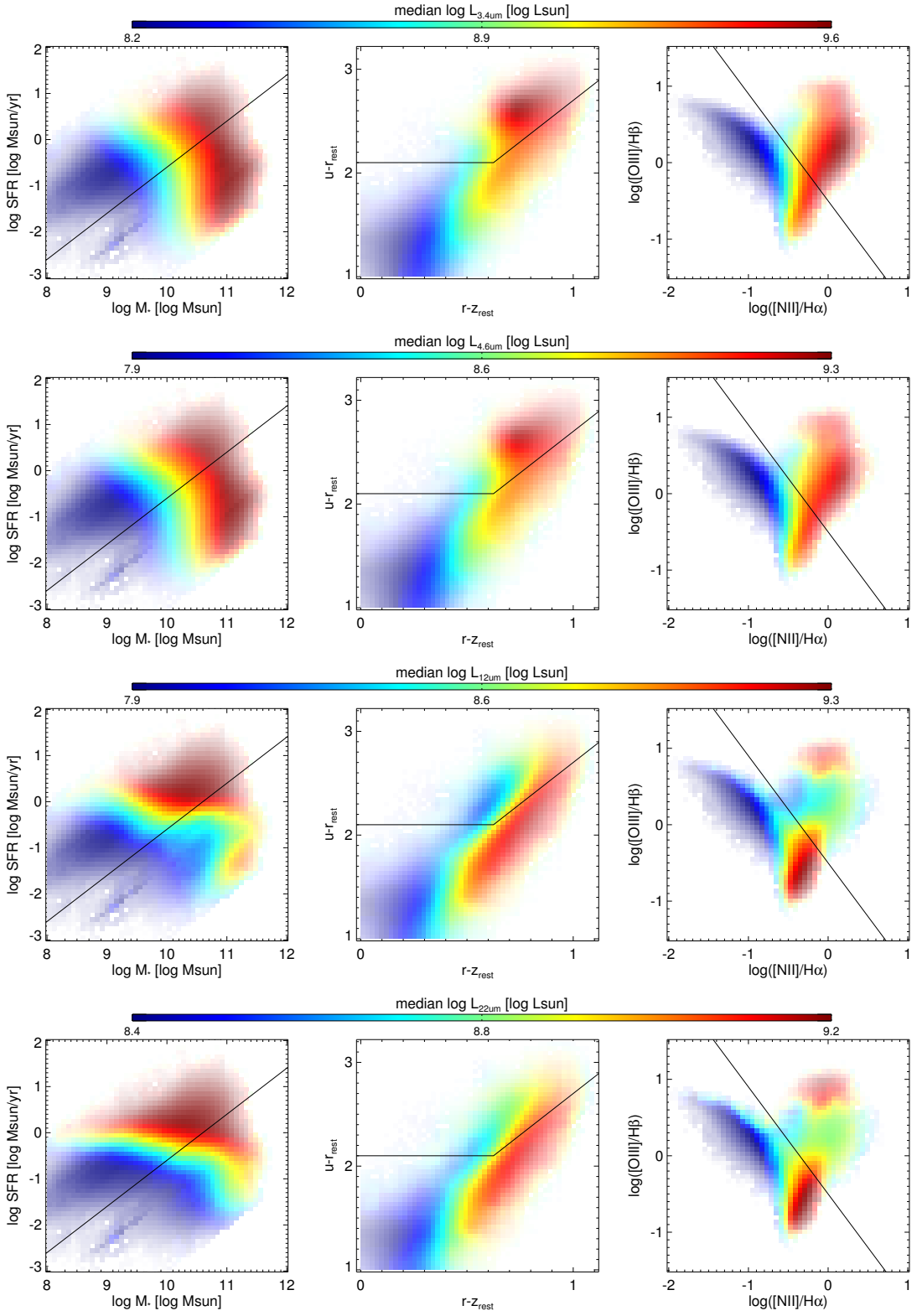

Figure 4.9: *The color codings are the mediums of 3.4 μm (W1), 4.6 μm (W2), 12 μm (W3), and 22 μm (W4) luminosity within each bin. The infrared data (W3/W4) shows the dust information, which are not sensitive in the optical or near-infrared bands.*

4.6.2 MASS AND STAR FORMATION RATE

In Figure 4.10, we show the color coding for median of sSFR, SFR, and stellar mass. As discussed before and shown in the first and second row, sSFR/SFR can be one indicator to separate early-type and late-type galaxies. The diagonal lines in the middle *urz* plot (middle middle) shows $(u-r)_{rest} - 1.6 * (r-z)_{rest}$ is a good SFR proxy. In the BPT diagrams, galaxies with the lowest metallicities have the highest sSFR (top right), but have low absolute SFRs (middle right). Moreover, the AGN (Seyfert galaxies) in the BPT diagram have relatively high (s)SFR. It remains to be tested whether this is real or due to MAGPHYS mistaking AGN heating for star formation.

In Figure 4.11, we show the sSFR distribution for different mass ranges. As known before and shown in the *urz* and BPT diagram, there are more massive early-type galaxies than late-type galaxies. High and low mass galaxies are concentrated in relatively small parts of *urz* and BPT parameter space, indicating they are homogeneous sets of objects. There is no bimodality in star-forming activity within these mass ranges. Only at 10^{10}-$10^{11} M_{\odot}$ there exists a broad range in galaxy properties, with substantial populations of each passive and star forming galaxies.

The upper row of Figure 4.12 we color code with stellar the surface mass density. The strong correlation between passiveness and surface mass density, even at a fixed stellar mass, suggests that a high surface mass density is a necessary and sufficient condition for passiveness (Bell 2008; Bell et al. 2012). Surface mass density also increases with mass along the star-forming sequence, suggesting that galaxies grow inside-out through star formation up until a point at which the surface mass density reaches a critical value after which star formation stops.

The middle and bottom rows are color coded with rest-frame $u-r$ and $r-z$ distribution. This emphasizes once more that a single color, especially the widely used $u-r$ color, is not enough to be a SFR indicator and separate early- and late-type galaxies. There is a remarkable correspondence between $r-z$ color and surface mass density, presumably due to the underlying correlation with metallicity.

4.6.3 EMISSION LINES

Figure 4.13 shows the color coding according to emission line ratio. The log([NII]/Hα) values are highest for early-type galaxies, objects that are referred to as as LINERs, the emission lines of which are most likely powered by hot, evolved stars. Their large log([OIII]/Hβ) are indicative of a relatively high-energy ionizing source, part of which, in a subset of objects called Seyferts, can be attributed to AGN. The upper left panel shows

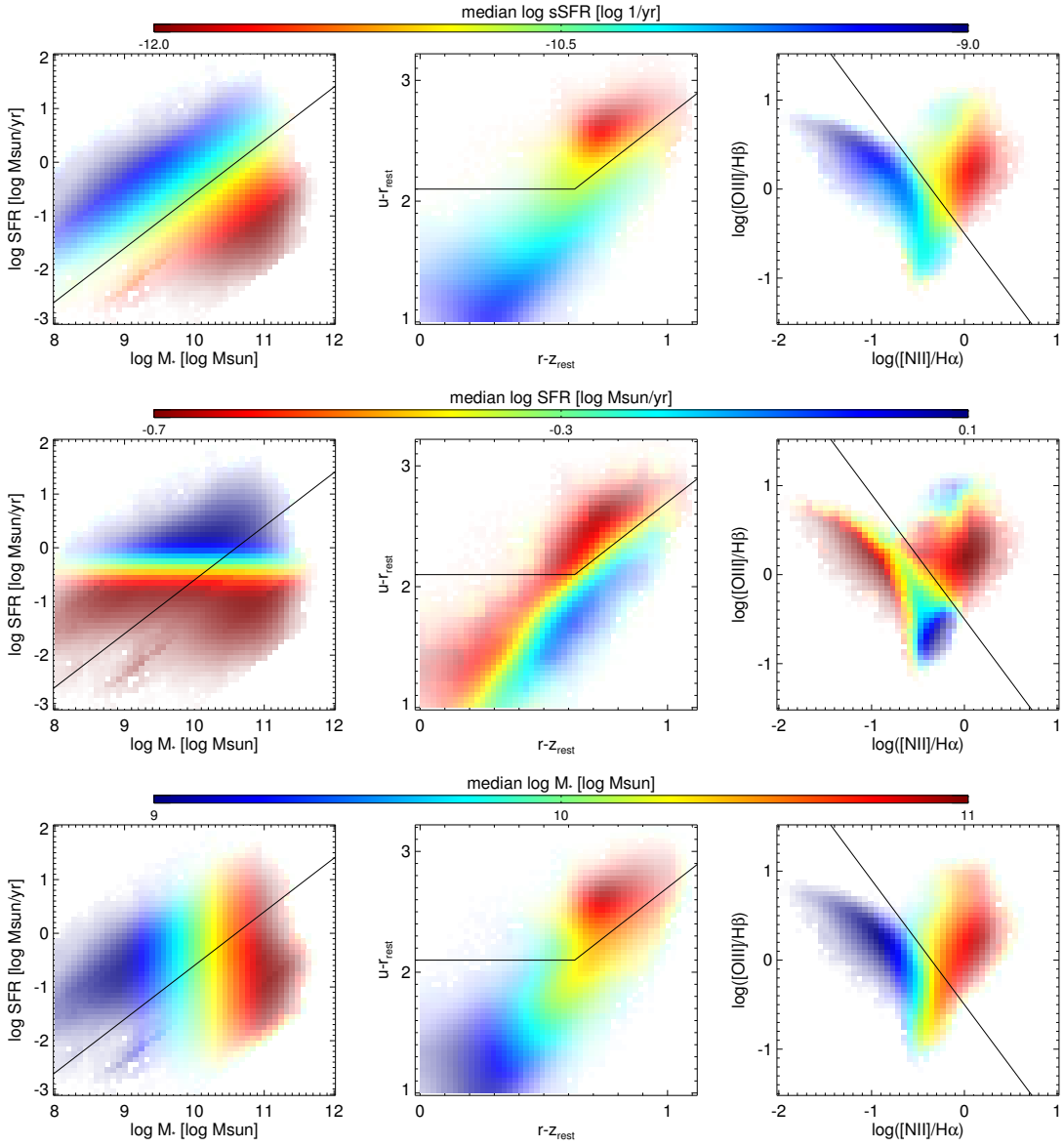

Figure 4.10: *The color coding is the median of sSFR, SFR, and stellar mass, within each bin. In the left plots, most low SFR/sSFR red galaxies are in the upper left part. In the right plot, most high SFR/sSFR blue galaxies are in the left part. As shown in the urz diagram, we decide a criterion of early-type and late-type galaxies:* $(u-r)_{rest} = 2.1$ *and* $(u-r)_{rest} = 1.6(r-z)_{rest} + 1.1$.

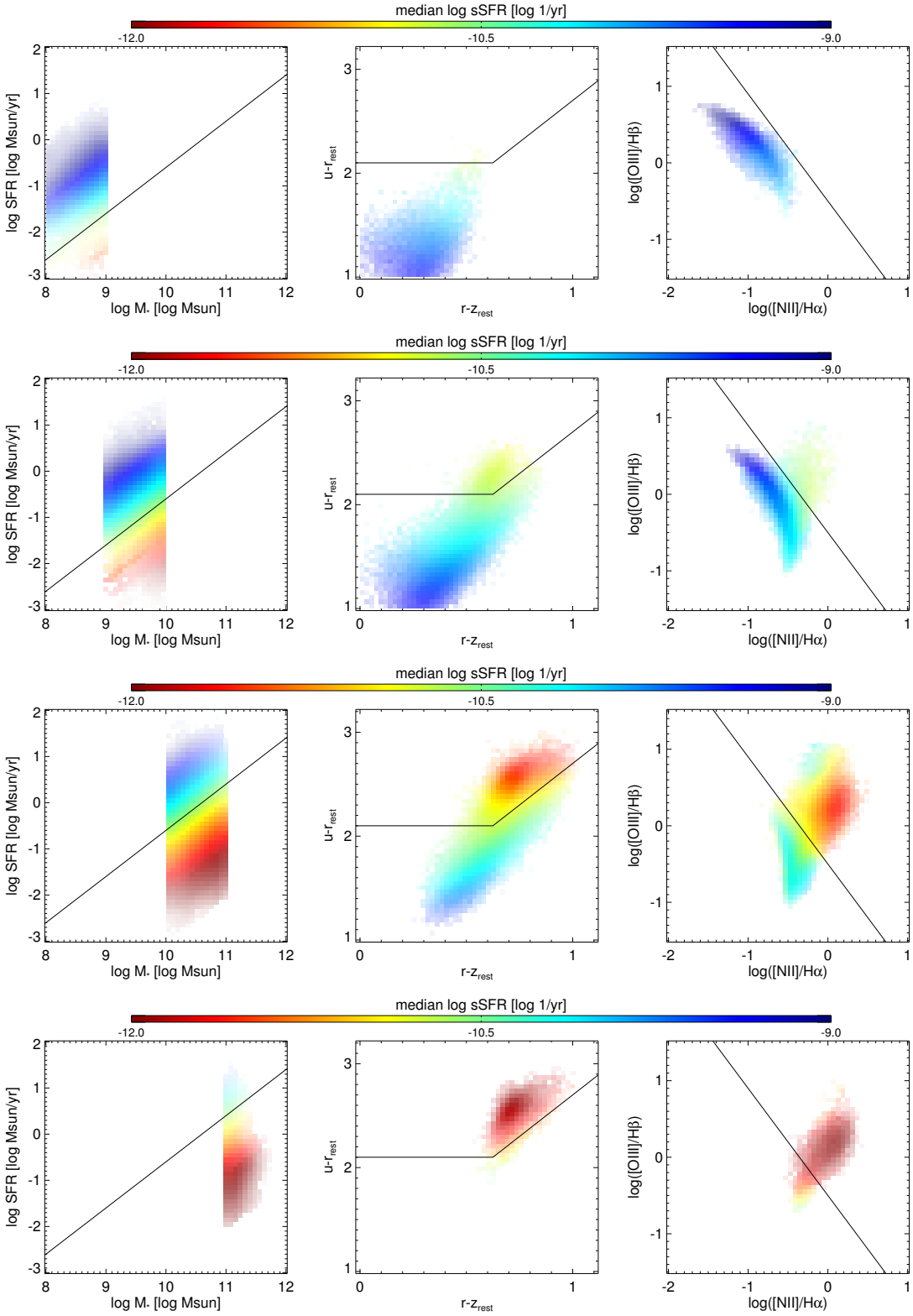

FIGURE 4.11: *Here we separate galaxies by stellar masses. The color coding is the sSFR within each bin.*

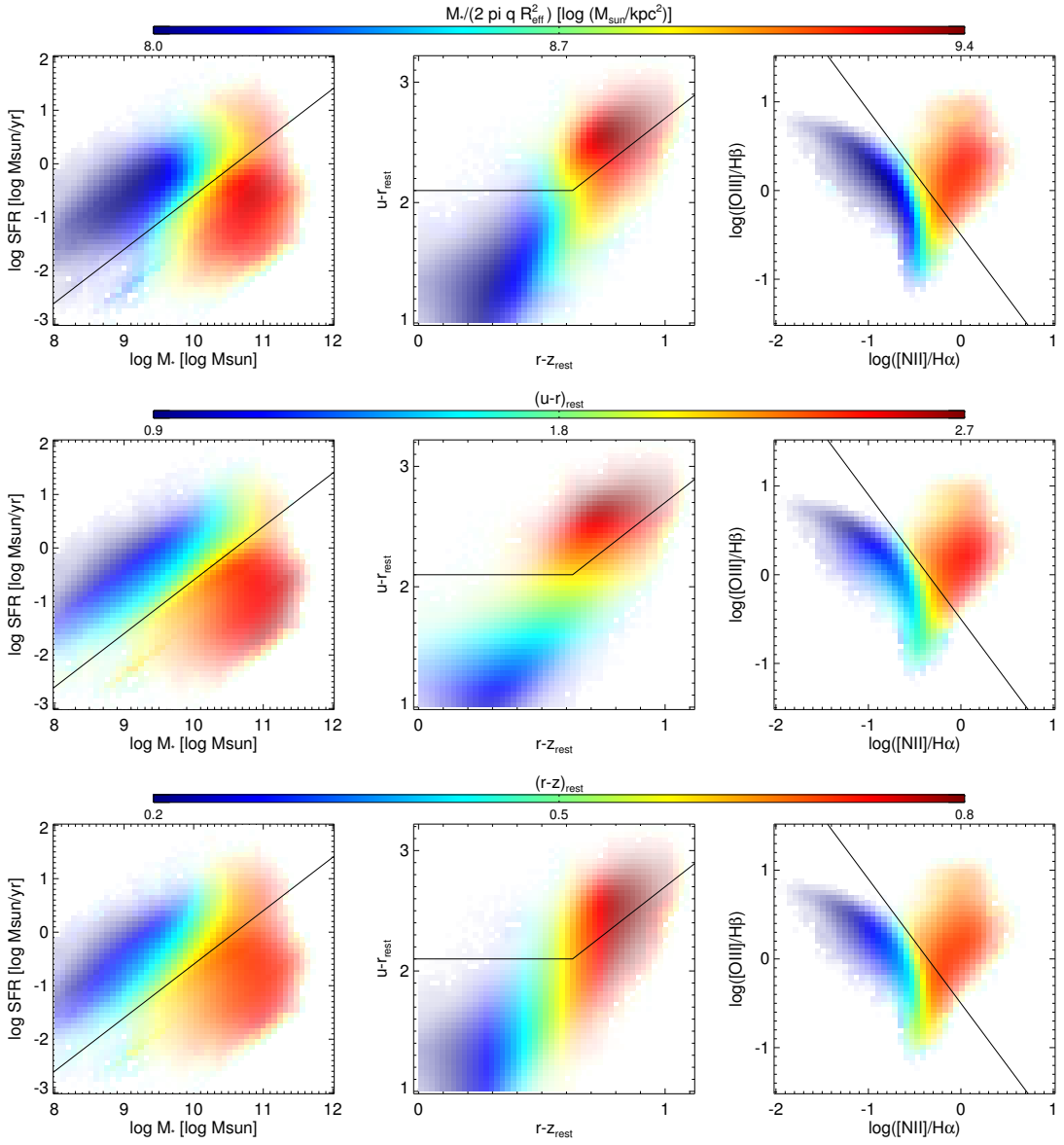

FIGURE 4.12: *The color coding is the median of surface mass density, rest-frame $u-r$ and rest-frame $r-z$ within each bin.*

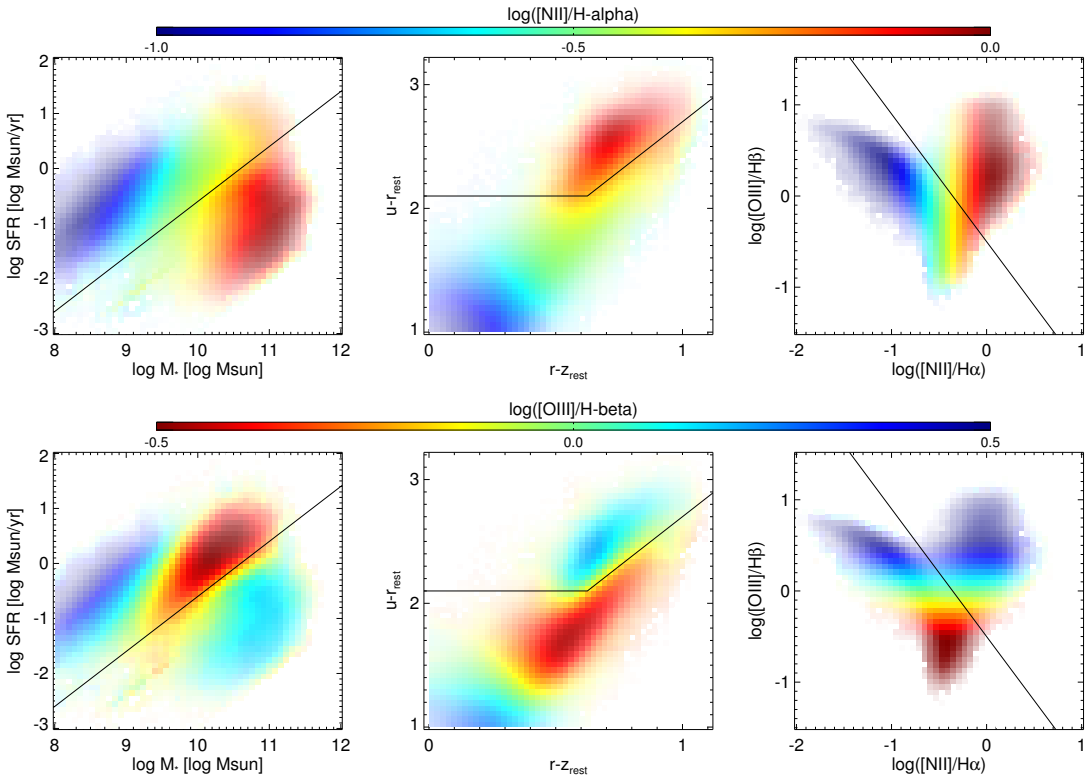

FIGURE 4.13: *The color coding is the median value of* log*([N*II*]/H*α*) and* log*([O*III*]/H*β*) within each bin. We only adopt galaxies with significant emission lines (SNR*> 2 *for H*α*, H*β*, [N*II*], and [O*III*]) in the right plots.*

a similar pattern as the surface mass density in the upper left panel in Figure 4.12. The diagonal lines of constant log([NII]/Hα) correspond to the so-called fundamental metallicity relation (Mannucci et al. 2010). The log([OIII]/Hβ) values are high for massive late-type galaxies and shows two peaks because of LINERS and low metallicity late-type galaxies. Massive late-type galaxies have relatively low log([OIII]/Hβ) values, and our classification of early- and late-type galaxies in both SFR versus stellar mass and *urz* plots shows a clear separation by log([OIII]/Hβ). The individual clear separation of these two ratio of emission lines in the first two columns proves again that the three methods to separate late-type from early-type galaxies are essentially interchangeable.

4.6.4 PROJECTED AXIS RATIO

Figure 4.14 shows the color coding for median of the *g*-band projected axis ratio. It is clear that massive early-type galaxies are roundest, and early-type galaxies are rounder

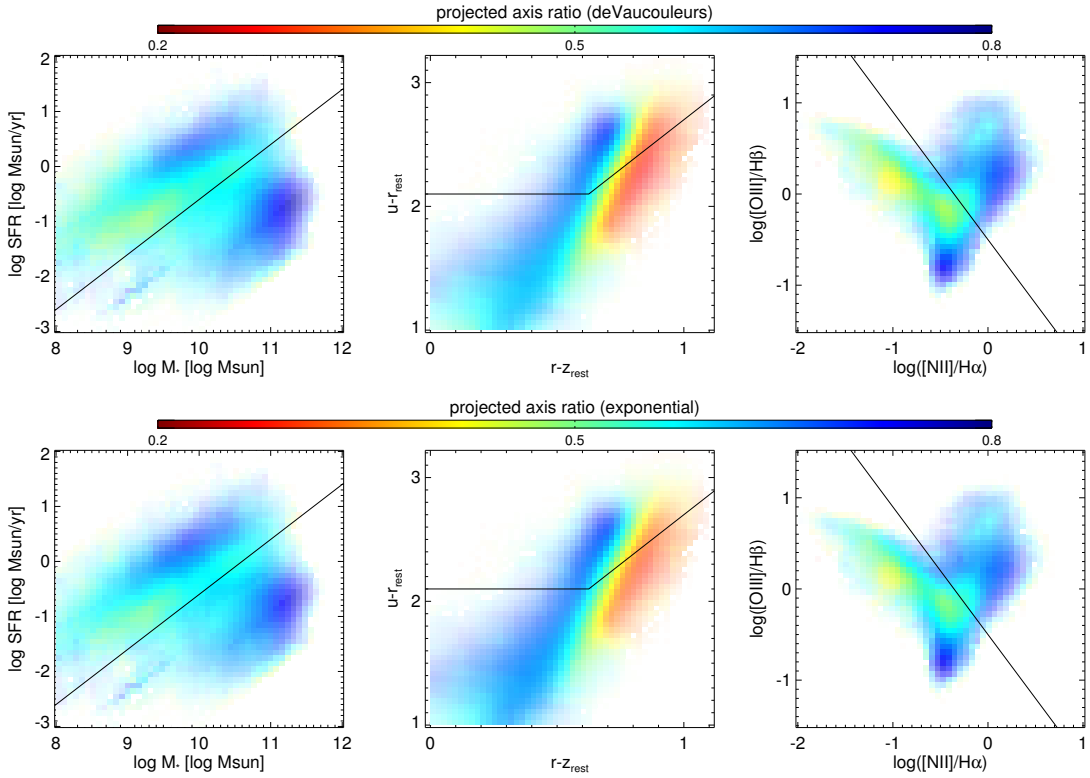

Figure 4.14: *The color coding is the g-band projected axis ratio of the pure de Vaucouleurs profile (upper) and the pure exponential profile (lower).*

than late-type galaxies. It also shows that massive and high SFR galaxies are rounder than other late-type galaxies, and low mass late-type galaxies are flattest. The strong variation of the axis ratio with color for a large part due to inclination: edge-on disks are more reddened than face-on disks. The upper right region of the BPT diagram that these are flatter on average, indicative of the disk-like nature of Seyfert galaxies.

The pure de Vaucouleurs profile (upper row) and pure exponential profile (lower row) in SDSS correspond to $n = 4$ and $n = 1$ of the Sérsic profile, respectively. The exponential profile tends to have slightly higher projected axis ratio for both early- and late- type galaxies. To investigate the structural parameters more, we will investigate the projected axis ratio, radius, and Sérsic index in the future.

4.7 CONCLUSIONS

We use a wide range of photometry, including optical to infrared information for updating mass and SFR estimates for the SDSS spectroscopic galaxy sample. Stellar masses are improved as a result of the inclusion of 2MASS and the 3.4 and 4.5 μm WISE bands, in addition to the SDSS optical photometry. The inclusion of the WISE 12 and 22 μm provide us with a infrared-based SFR estimate, which is complementary to the existing measurements based on emission line luminosities and UV flux.

This large sample at low redshift offers the best view to date of the bimodality of the galaxy population. We find that the color-color selection technique used in this thesis works as well to distinguish early-type (passive) galaxies from late-type (star-forming) galaxies as alternative methods, such as emission line ratios or 12 μm/3.4 μm luminosity ratio.

This rich data set serves as a new backbone for high-redshift galaxy studies and reveals many known and unknown trends for present-day galaxies, motivating a myriad of possibilities for exploration in the immediate future.

5 Summary and Outlook

In the course of this thesis, we have put together and modeled an unprecedented sample of shape measurements for galaxies at $z > 1$, in order to use the implied intrinsic shapes, and their dependence on redshift and galaxy mass as a constraint on the evolution of early-type galaxies. In this closing chapter, we summarize and provide an outlook.

5.1 The Way to Build Large Ellipticals

In Chapter 2, we show that massive early-type galaxies were significantly flatter at $z \sim 2$ compared to $z \sim 0$ by measuring their projected axis ratios. Our assumption is that the viewing angle is random which is plausible for our large sample of ∼400 massive early-type galaxies from deep near-infrared high-resolution ground-based VLT/HAWK-I observations. This result confirms the result based on 14 galaxies in van der Wel et al. (2011) and makes it more convincing with a much larger sample size. Our result also shows that this shape evolution is only significant before $z \sim 0.8$, which is consistent with the previously reported lack of evolution up to $z = 1$ in both clusters and fields (Holden et al. 2009, 2012). Moreover, we show that at any redshift the most massive early-type galaxies are the roundest.

In Chapter 3, our study of the shape evolution extend to $z = 2.5$ by the deeper near-infrared high-resolution space-based HST/WFC3 data from CANDELS. We built a two-population (oblate+triaxial) model: the oblate component represents disk-shaped objects and the triaxial component represents spheroids. We found that the oblate fraction of massive early-type galaxies that were distinctly oblate (with an intrinsic thick-

ness of c/a ~0.3) was three times larger and triaxial fraction was two times smaller at $z \sim 2$ compared to the present day universe. Bruce et al. (2012) also used a bulge-disk decomposition to show that many of massive early-type galaxies host pronounced disks at high redshift. The disk-like structures of massive early-type galaxies show that these galaxies formed when gas had time to settle into disks.

The increasing co-moving number density of early-type galaxies between $z \sim 2$ and the present (e.g., Bell et al. 2004; Faber et al. 2007; Brammer et al. 2011) indicates that early-type galaxies continuously form. Combined with our new insights in structural evolution, this number density evolution implies that when most of the star formation in a (future) early-type galaxy ceases, it looks like a disk-like galaxy. It subsequently grows through the accretion of externally formed stars, growing larger (e.g., van Dokkum et al. 2008; van der Wel et al. 2008) and rounder (this thesis; van der Wel et al. 2011; Chang et al. 2013a,b) in this merging process. This continued evolution process and subsequent growth occurs at all redshifts $0 < z < 2.5$. At $z < 1$, the formation rate of new early-type galaxies and their structural evolution are essentially balanced such that the relative numbers of disk-like and round early-type galaxies remain the same even though the number density continues to increase.

5.2 Low Mass Early-type Galaxies

In Chapter 3, we extend the structural studies of early-type galaxies to lower stellar mass which was impossible before our deep CANDELS data. Remarkably, we find that at a stellar mass of $\sim 10^{10} M_{\odot}$ the typical early-type galaxy at $z \sim 2$ is rounder than its equally massive counterpart in the present-day universe. Applying the two-component (oblate+triaxial) model, we find that oblate, disk-like fraction declines from ~70% to ~30% from $z = 0$ to $z = 2$. It is not clear why the low-mass early-type galaxies at $z \sim 2$ are predominantly round, but one possible explanation is that their star-forming progenitors had not settled into stable disks, like is the case in the present-day Universe. The prominent, present-day population of disk-like, low-mass, early-type galaxies could be the result of a different evolutionary channel: gas stripping of star-forming galaxies that fall into massive halos is known to produce passive galaxies with a similarly disk-like structure as their progenitors. Thus, in this lower-mass regime the structural properties of the galaxies may reflect the existence of multiple evolutionary paths to passiveness. The disk-like population at high redshift is expected to be less prominent due to the absence of massive halos.

5.3 A Large Local Galaxies Catalog

Chapter 4 is a complementary study of the classification of early-type and late-type galaxies at low redshift. In the previous chapters, we used color-color diagrams and SFR to select early-type galaxies because visual classification is difficult in general and almost impossible at high redshift. We assemble multi-wavelength photometry for the full SDSS spectroscopic galaxy sample, drawing from the SDSS, 2MASS, and WISE surveys, covering the wavelength range 0.4-22 μm. We use the latest modeling techniques (MAGPHYS, da Cunha et al. 2008) to estimate stellar masses and star formation rates, which we will make available to the community upon completion. The addition of photometry at >1 μm improves these measurements as compared to previous SDSS-based estimates. The newly measured star formation rates allow us to test methods to separate early-type (passive) from late-type galaxies (star-forming) galaxies. Most importantly, we show that the scheme used in this thesis – using two rest-frame colors to separate the types – works well. Furthermore, we show that selection criteria based on emission line ratios (from SDSS) and 12 μm/3.4 μm luminosity ratios from WISE work equally well.

5.4 Outlook

In the future, we can extend the structure studies by near-infrared imaging over a larger area. We can construct large samples of rare, massive galaxies at $z \sim 2$ and start addressing the question whether the triaxial structure of massive early types originated recently or at early epochs, and whether the most massive galaxies already settled into stable disks at earlier time. Besides, the comparison between projected axis ratio and Sérsic index at all redshifts will be also helpful for structural studies.

We can also compare early-type galaxies with late-type galaxies and find the potential progenitors of the oblate massive early-type galaxies and the round low-mass early-type galaxies found at $z \sim 2$. Specifically, van der Wel et al. (2013b, in preparation) suggests that low-mass late-type galaxies at $z > 1$ have not yet attained stable rotational structures, like at later cosmic time. Because the transition from late-type to early-type galaxies is still unclear, it will be challenging to connect the structural evolution of different types of galaxies.

In the near future, we will publish the catalog described in Chapter 4. We have to find out what causes the systematic trends in Figure 4.4 and 4.5 by improving our priors, in particular by imposing a maximum dust mass on passive galaxies which currently skews our stellar mass and SFR estimates.

We can also include other surveys in an even wider range of wavelengths, such as the Galaxy Evolution Explorer (GALEX), Infrared Array Camera (IRAC), and the Herschel ATLAS, as additional UV and far-infrared inputs for MAGPHYS and compare the matched samples with our current results. There are also lots of physical parameters, such as dust masses, the total infrared luminosity, the fraction of total infrared luminosity contributed by dust in the ambient ISM, the total effective V-band absorption optical depth of the dust, the fraction of this contributed by dust in the ambient ISM, the fractional contributions by PAHs, the hot mid-infrared continuum and warm dust in thermal equilibrium to the infrared luminosity of stellar birth clouds, and equilibrium temperature of warm/cold dust in stellar birth clouds/ambient ISM, to investigate from the MAGPHYS output.

The properties of nearly one million galaxies from our upcoming catalog provide many possibilities to investigate our local Universe, in particular to provide an updated description of the mass function and the distribution of star formation across the mass function. The results at low redshift serve as the backbone of high redshift studies, and our work provides a large catalog from our local Universe to compare with high-redshift galaxies in order to investigate galaxy evolution.

The richness of the newly assembled data set is illustrated in Section 4.6. For instance, massive early-type galaxies with large 12 μm luminosities high SFR galaxies with increased 3.4 μm luminosities. The nearly one million galaxies from $z = 0$ to $z = 0.1$ will be useful to investigate the mass/redshift dependence for structural parameters. The projected axis ratios as shown in Figure 4.14 provide a direction to continue the projected axis ratio and shape model results of Chapter 2 and 3, as ground work for high redshift studies. Moreover, the projected axis ratio, Sérsic index, and radius from different models (exponential, de Vaucouleurs, Petrosian) in the SDSS can be also discussed.

Our structural work from high redshift to low redshift, and the up to date catalog of nearly one million local galaxies, will be the basis for future extragalactic studies, such as the new results from the Atacama Large Millimeter/submillimeter Array (ALMA), and new surveys from the next generation James Webb Space Telescope (JWST). Particularly, the infrared coverage (0.6 to 28 μm) of JWST will provide deep imaging to continue our studies of structure evolution to even higher redshift at $z > 2$. Both of new, large local catalog and our measurements from CANDELS of galaxies up to z~2.5 will serve as the backbone for the future observations.

A

Full Table 2.1

Table A.1: *Massive early-type galaxies:* $0.6 < z < 1.8$, $log(M/M_{\odot}) > 10.7$ *and* $sSFR < 1/3t_H(z)$. *ID is the same as Cardamone et al. (2010). Redshift* (z_{phot}) *and stellar mass* (M_*) *are from SED fitting. K-band magnitude(K), effective radius* (R_e) *and projected axis ratio* (q_{proj}) *are from the* GALFIT *results.*

ID	z_{phot}	M_* [$\log M_{\odot}$]	$K[mag]$	R_e	q_{proj}
4032	1.15	10.72	20.68	0.25	0.49
4213	1.11	10.73	20.25	0.35	0.83
4619	1.00	10.87	21.72	0.09	0.87
4844	1.59	10.94	20.94	0.35	0.56
5375	1.13	11.33	19.46	0.44	0.96
6197	1.36	10.84	21.12	0.20	0.87
6307	0.69	11.31	18.77	0.60	0.57
6490	1.09	10.95	20.35	0.17	0.81
7042	0.61	11.26	18.51	0.68	0.68
7268	0.99	10.78	20.58	0.17	0.92
7359	0.69	10.83	19.53	0.37	0.80
7453	0.93	11.32	18.93	0.74	0.78
7564	1.17	10.75	20.93	0.12	0.14
7968	0.63	10.82	19.93	0.30	0.65
8218	0.68	10.94	19.53	0.37	0.85
8319	0.93	10.96	20.05	0.33	0.52
8693	0.69	11.09	19.22	0.35	0.95
8939	1.24	10.76	20.90	0.18	0.88
9321	1.23	11.16	20.24	0.42	0.89
9391	1.33	11.07	20.46	0.13	0.41

9397	0.67	11.17	19.26	0.38	0.64
9426	1.38	11.05	21.04	0.12	0.53
9822	1.13	10.85	20.83	0.29	0.35
9825	1.40	11.28	20.20	0.32	0.97
9963	1.37	10.75	21.03	0.17	0.46
9992	1.37	10.82	21.02	0.40	0.54
10207	1.37	10.84	20.86	0.24	0.40
10658	1.39	10.83	20.93	0.34	0.79
10842	0.69	10.87	19.50	0.52	0.35
11103	0.63	10.81	19.34	0.47	0.51
11573	1.38	10.93	20.59	0.24	0.80
11756	0.69	11.46	18.65	0.38	0.88
11974	0.77	11.01	19.33	0.34	0.92
12238	0.76	10.90	19.48	0.36	0.76
12586	0.69	11.60	18.19	0.98	0.79
12700	0.67	11.08	18.75	2.90	0.81
12760	0.69	11.03	19.14	0.33	0.51
12781	0.73	11.01	19.70	0.21	0.55
12917	0.93	10.92	20.17	0.16	0.67
13322	1.24	11.04	20.40	0.43	0.52
13455	1.04	10.96	20.21	0.32	0.65
13781	0.82	11.08	19.81	0.22	0.63
14321	0.75	10.74	19.66	0.38	0.54
14758	1.38	10.70	21.20	0.15	0.52
15249	0.73	10.80	19.93	0.20	0.90
15654	0.69	11.50	18.43	1.03	0.45
15671	1.15	10.78	21.33	0.18	0.37
15823	0.70	11.41	18.69	0.49	0.71
16335	0.69	11.35	19.01	0.47	0.77
16406	0.73	11.44	18.64	0.48	0.37
16418	1.32	10.89	20.72	0.37	0.83
16946	0.63	10.93	19.02	0.30	0.53
17224	0.85	11.19	19.81	0.27	0.52
17293	0.66	10.78	20.21	0.11	0.82
17537	0.76	11.33	18.58	1.14	0.79
17755	0.78	10.91	19.86	0.19	0.33
17850	0.97	11.16	19.64	0.38	0.51
17950	1.10	10.73	21.13	0.19	0.55
18032	1.38	10.74	21.34	0.11	0.73
18268	1.03	11.33	19.34	0.50	0.87
18388	1.40	11.02	20.65	0.20	0.48
18461	1.57	11.70	19.41	0.40	0.79

18516	1.41	11.35	20.43	0.48	0.72
18656	1.38	10.97	20.98	0.15	0.35
18685	1.63	11.07	20.39	0.70	0.71
18829	0.72	10.90	19.53	0.28	0.79
18891	0.62	10.74	20.15	0.21	0.10
19011	0.62	11.57	17.67	1.43	0.61
19761	0.73	11.85	17.60	2.22	0.84
20149	0.68	10.73	19.98	0.33	0.78
20490	0.69	10.96	19.37	0.42	0.20
20628	0.69	10.70	19.96	0.41	0.70
20808	0.73	11.13	19.14	0.59	0.58
21329	1.54	11.16	20.50	0.29	0.94
21383	1.34	10.76	21.63	0.19	0.64
22036	0.71	11.05	19.09	0.58	0.73
22063	1.31	10.96	20.98	0.40	0.55
22261	0.69	10.86	19.77	0.24	0.39
22451	0.75	10.89	20.34	0.08	0.19
22458	1.40	10.76	21.90	0.17	0.22
22467	0.73	11.35	18.77	0.65	0.83
22664	1.35	11.07	20.65	0.26	0.85
22839	1.38	10.99	21.16	0.09	0.80
22875	0.69	11.34	18.84	0.54	0.80
22980	0.68	10.72	19.97	0.25	0.41
23246	0.63	10.76	19.70	0.20	0.27
23278	1.11	11.23	19.65	0.43	0.68
23584	0.69	11.09	19.44	0.28	0.37
24086	0.73	10.77	20.05	0.33	0.91
24413	0.73	10.74	20.12	0.24	0.23
24462	0.68	11.46	18.60	0.78	0.92
24551	0.69	11.54	18.78	0.43	0.62
24591	0.96	11.43	18.97	0.59	0.92
25186	0.74	10.86	19.84	0.27	0.93
25417	1.34	10.96	20.79	0.33	0.39
25489	0.74	10.89	19.82	0.31	0.91
25609	1.04	11.01	20.27	0.17	0.26
25613	1.22	10.71	21.18	0.14	0.58
25904	0.69	10.76	20.02	0.36	0.80
26005	0.99	10.77	20.56	0.14	0.17
26199	0.68	10.78	19.77	0.27	0.69
26284	0.68	10.73	19.99	0.28	0.43
26460	0.68	10.78	19.45	0.44	0.74
26855	0.62	10.80	19.24	0.41	0.38

26900	0.68	11.13	18.96	0.31	0.86
27039	1.38	10.77	21.28	0.11	0.36
27098	0.67	10.76	19.98	0.27	0.58
27354	0.67	10.88	19.39	0.17	0.92
27497	1.38	10.74	21.31	0.29	0.46
27654	1.13	11.05	20.43	0.22	0.84
27703	1.54	10.98	21.01	0.22	0.56
27755	1.11	10.87	20.65	0.22	0.58
27772	1.13	11.57	19.06	0.79	0.79
27854	1.12	10.94	20.49	0.17	0.42
28210	1.13	10.80	20.54	0.37	0.62
28574	1.13	11.19	20.46	0.30	0.51
28617	1.19	10.74	21.47	0.16	0.20
28668	1.07	10.73	20.78	0.21	0.59
28752	1.24	11.16	21.29	0.24	0.49
28837	1.09	11.23	20.04	0.30	0.21
29275	1.10	11.00	20.22	0.24	0.41
29392	1.12	10.87	20.59	0.11	0.21
29472	1.21	10.78	20.85	0.25	0.79
29720	0.63	10.70	19.66	0.29	0.77
29802	1.22	11.62	19.01	0.55	0.89
29868	1.39	11.14	20.35	0.49	0.66
29942	1.22	11.12	20.18	0.66	0.47
30122	1.10	11.20	19.57	1.22	0.61
30480	1.22	10.70	21.15	0.22	0.42
30776	1.23	11.01	20.51	0.17	0.26
30940	1.17	10.80	19.72	2.46	0.60
31391	1.09	11.74	18.95	0.65	0.92
31740	1.12	11.08	19.82	0.57	0.86
31786	1.47	11.23	20.34	0.44	0.21
32274	1.11	11.13	19.87	0.55	0.90
32336	1.25	10.84	20.90	0.20	0.60
32911	1.35	11.12	20.33	0.18	0.62
33181	1.26	11.04	20.46	0.26	0.15
33402	0.96	10.79	20.45	0.17	0.80
33645	1.24	10.78	20.75	0.31	0.70
33707	1.11	10.89	20.47	0.31	0.77
33959	0.95	11.06	19.91	0.21	0.35
34275	0.73	11.21	19.30	0.47	0.88
34388	1.09	10.74	20.27	1.85	0.73
35023	1.24	11.33	19.85	0.38	0.33
35105	0.66	10.83	19.33	0.63	0.81

35311	0.62	10.76	19.62	0.35	0.93
35316	0.74	10.94	19.47	0.34	0.87
35376	1.23	11.52	19.05	0.83	0.83
35496	1.40	11.41	19.62	0.45	0.88
35691	1.59	10.94	21.02	0.27	0.76
35756	1.23	10.99	20.34	0.28	0.60
35882	1.61	10.96	21.10	0.25	0.72
36103	1.33	10.71	21.15	0.22	0.38
36340	0.96	10.82	20.67	0.13	0.11
36601	0.67	10.86	19.39	0.37	0.84
37158	0.91	10.78	20.78	0.15	0.92
37233	0.95	10.75	20.47	0.10	0.69
37269	1.64	10.82	21.51	0.21	0.69
37604	1.20	10.97	20.95	0.29	0.48
37767	0.67	11.08	18.98	0.64	0.21
37796	1.16	10.75	21.20	0.15	0.79
37845	1.36	10.77	21.55	0.32	0.89
37929	1.22	10.78	21.39	0.12	0.45
37956	1.05	10.98	20.17	0.25	0.95
37959	0.73	10.96	19.37	0.44	0.50
38026	0.69	11.45	18.55	0.97	0.59
38032	0.67	10.71	19.86	0.35	0.72
38047	1.23	11.15	20.39	0.31	0.82
38109	1.58	11.21	20.58	0.31	0.99
38226	1.22	11.13	20.69	0.22	0.91
38235	0.68	11.21	18.66	0.65	0.83
38388	1.38	11.06	20.79	0.21	0.65
38418	1.26	10.92	21.01	0.21	0.75
38540	1.57	10.91	20.98	0.19	0.66
38788	0.69	11.55	18.99	0.35	0.61
38866	1.22	10.72	21.15	0.19	0.71
38869	0.97	11.06	19.78	0.37	0.64
38922	0.98	11.33	19.16	0.49	0.66
39157	0.69	11.17	18.94	0.60	0.84
39371	1.76	11.00	21.28	0.17	0.80
39578	0.74	11.14	19.06	0.29	0.29
39611	0.69	10.71	19.97	0.09	0.34
39635	0.68	10.72	20.15	0.21	0.83
39794	1.63	11.18	20.99	0.20	0.55
39940	1.63	11.16	20.79	0.24	0.77
40050	1.07	10.90	20.53	0.21	0.86
40124	0.69	11.25	19.33	0.31	0.36

40251	0.83	11.57	18.78	0.95	0.83
40458	1.78	11.07	21.15	0.34	0.71
41010	0.68	10.75	19.90	0.25	0.60
41080	0.61	11.07	18.83	0.34	0.78
41135	1.11	10.74	21.08	0.18	0.71
41167	0.69	11.75	17.86	1.05	0.80
41362	0.73	10.76	20.20	0.25	0.64
41756	0.67	11.13	19.24	0.26	0.80
41853	1.71	11.07	20.90	0.19	0.61
41859	0.67	11.21	18.96	0.36	0.90
41900	1.31	10.80	20.90	0.18	0.51
42213	1.11	11.07	20.36	0.20	0.45
42252	0.95	10.80	20.55	0.20	0.55
42747	1.16	10.95	20.49	0.20	0.95
42991	1.02	10.86	20.56	0.16	0.78
43092	1.04	10.98	20.24	0.22	0.66
43195	0.95	11.14	19.41	0.48	0.42
43404	1.32	10.89	20.80	0.26	0.48
43600	0.73	11.42	18.72	0.68	0.78
43621	0.67	11.57	18.36	0.51	0.88
43849	1.32	10.98	20.55	0.40	0.87
43953	0.73	11.00	20.00	0.28	0.82
43971	0.74	11.08	19.12	0.41	0.85
44122	0.63	11.11	19.25	0.43	0.62
44301	0.68	10.97	19.09	0.59	0.33
44319	0.67	11.05	19.11	0.36	0.86
44619	0.67	10.93	19.47	0.42	0.53
44631	0.85	10.98	20.11	0.22	0.84
44803	0.68	11.10	18.74	0.87	0.41
45172	1.15	10.84	20.80	0.35	0.43
45538	1.60	11.23	20.71	0.31	0.55
45585	1.11	11.59	19.03	0.51	0.60
45697	0.74	10.90	19.49	0.25	0.77
46156	1.52	11.09	20.98	0.19	0.74
46245	1.36	10.89	21.43	0.16	0.44
46248	1.31	11.03	20.69	0.21	0.76
46628	0.73	11.20	19.58	0.25	0.89
46643	0.73	10.76	19.92	0.41	0.22
46691	0.73	11.04	18.91	0.58	0.82
46835	1.10	11.48	18.88	0.65	0.65
46838	1.60	10.76	21.48	0.00	0.29
46934	0.83	11.38	18.66	0.73	0.88

47126	1.15	10.71	21.28	0.48	0.73
47184	0.97	10.77	20.34	0.21	0.68
47423	1.07	11.04	20.05	0.30	0.64
47488	1.04	11.07	20.17	0.21	0.54
47522	0.69	10.95	19.32	0.33	0.41
47536	1.22	10.81	20.51	0.47	0.81
47792	1.06	10.92	20.34	0.41	0.47
47878	1.58	11.08	20.77	0.21	0.31
48095	1.05	10.71	20.22	0.66	0.82
48282	1.22	10.86	20.76	0.17	0.49
48310	0.97	10.90	20.28	0.26	0.63
48554	0.75	11.27	19.01	0.34	0.56
49068	0.68	10.98	19.20	0.28	0.38
49077	0.68	10.80	19.46	0.38	0.97
49079	1.59	11.10	20.81	0.32	0.24
49788	1.30	10.80	21.09	0.16	0.43
49897	1.71	11.12	21.36	0.39	0.65
49994	0.87	10.94	19.81	0.17	0.73
50337	1.32	10.95	20.78	0.15	0.81
50639	0.83	10.91	20.23	0.17	0.40
50664	0.68	11.09	19.56	0.36	0.28
50946	0.68	10.84	19.77	0.31	0.40
50967	0.90	10.75	20.21	0.22	0.34
51112	1.06	10.86	20.73	0.00	0.69
51172	0.69	10.92	19.13	0.41	0.66
51271	0.60	10.89	19.24	0.35	0.69
51633	0.97	10.71	20.69	0.15	0.55
51813	1.31	11.11	20.52	0.14	0.40
52265	1.60	11.29	20.67	0.19	0.22
52913	1.24	10.75	21.06	0.32	0.79
53140	0.96	10.79	20.49	0.17	0.85
53831	1.58	10.78	21.89	0.13	0.72
53939	1.18	10.89	20.52	0.51	0.69
54028	0.95	10.83	20.41	0.14	0.16
54078	1.33	11.04	20.78	0.41	0.33
54088	1.24	10.89	20.69	0.18	0.32
54126	1.31	11.14	20.31	0.09	0.19
54127	1.48	10.83	21.53	0.23	0.51
54177	1.02	11.53	21.02	0.16	0.59
54556	1.42	10.79	21.23	0.18	0.97
54725	0.67	11.30	18.54	0.60	0.94
54896	0.68	11.29	18.61	0.74	0.27

54977	0.84	10.70	20.27	0.15	0.91
55023	1.22	11.15	20.08	0.24	0.51
55389	1.22	10.89	20.77	0.30	0.97
55408	1.34	10.82	21.17	0.15	0.47
55806	1.07	10.76	20.67	0.19	0.49
55942	0.80	10.73	20.19	0.20	0.76
55959	0.71	10.74	19.83	0.18	0.87
56035	0.74	10.93	20.11	0.24	0.71
56082	1.59	11.02	21.14	0.20	0.66
56358	1.41	11.04	20.78	0.39	0.57
56481	0.95	11.31	19.13	0.32	0.74
56615	1.08	11.20	19.90	0.48	0.84
56637	1.41	11.44	20.05	0.36	0.57
56653	0.74	11.54	18.77	0.65	0.93
57022	0.85	10.80	20.70	0.36	0.21
57237	0.66	11.37	18.70	0.88	0.85
57443	1.53	11.08	21.02	0.19	0.82
57588	1.04	10.96	20.37	0.30	0.51
57715	1.31	10.95	21.06	0.12	0.68
57827	0.96	10.83	20.63	0.26	0.38
58268	0.73	11.07	19.62	0.35	0.39
58376	1.58	11.09	21.61	0.20	0.56
58477	0.68	11.11	19.11	0.29	0.91
58682	0.74	11.20	19.55	0.29	0.89
58995	0.82	10.75	20.45	0.21	0.52
59002	1.30	10.92	21.20	0.21	0.49
59219	1.30	10.84	20.71	0.29	0.90
59302	1.04	10.83	20.13	0.93	0.60
59366	1.08	10.81	20.78	0.25	0.39
59418	0.92	10.91	20.46	0.21	0.53
59512	0.95	10.75	20.56	0.16	0.68
59606	0.78	10.84	20.05	0.23	0.84
59903	1.04	10.88	20.51	0.22	0.94
59967	0.67	11.02	19.58	0.42	0.66
60026	0.73	11.22	19.22	0.34	0.93
60041	1.33	10.96	20.83	0.27	0.66
60083	1.03	10.87	20.46	0.26	0.87
60108	0.97	11.11	19.75	0.46	0.71
60243	0.69	11.43	18.29	0.67	0.97
60379	0.66	10.71	20.36	0.19	0.72
60465	0.73	10.81	19.61	0.34	0.32
60548	1.33	11.31	20.04	0.28	0.72

60628	0.67	11.88	18.26	0.50	0.81
60795	1.06	11.32	19.72	0.39	0.68
61157	0.68	10.83	20.11	0.20	0.90
61226	1.11	11.34	19.54	0.37	0.33
61314	0.73	10.98	19.83	0.32	0.90
61345	0.95	11.06	19.89	0.22	0.58
61477	0.73	10.74	20.66	0.23	0.26
61710	0.97	10.94	20.09	0.20	0.40
61826	0.75	11.49	18.92	0.74	0.82
61941	1.28	10.94	20.96	0.22	0.46
62106	1.13	11.63	19.07	0.94	0.81
62811	1.07	10.92	20.38	0.31	0.66
62833	1.13	10.82	20.32	0.62	0.91
63398	1.71	10.99	21.53	0.31	0.35
63517	1.06	10.81	20.65	0.29	0.67
63952	1.59	10.83	21.52	0.13	0.60
63962	0.60	11.06	18.93	0.55	0.75
64252	1.19	10.78	20.94	0.34	0.33
64266	1.04	11.24	20.19	0.25	0.73
64309	1.06	10.74	20.73	0.30	0.80
64333	1.04	10.80	20.29	0.46	0.80
64839	0.68	10.78	19.81	0.21	0.82
65158	1.64	10.85	21.22	0.36	0.34
65251	0.82	11.08	19.74	0.00	0.11
65553	1.13	11.40	19.43	0.57	0.75
65590	1.09	11.10	20.75	0.23	0.45
65813	0.73	11.05	19.62	0.36	0.35
66086	1.06	11.05	20.14	0.20	0.16
66261	0.93	10.77	20.11	0.62	0.60
66680	0.95	10.80	20.56	0.27	0.71
66758	0.71	11.00	19.00	0.36	0.64
67072	0.80	10.83	19.81	0.23	0.78
67145	1.55	11.22	20.14	0.97	0.63
67774	1.11	10.83	21.11	0.20	0.69
67888	1.36	10.95	21.13	0.24	0.70
67950	0.97	11.56	19.27	0.40	0.83
68027	1.11	10.79	20.59	0.26	0.56
68046	1.07	11.56	19.06	0.64	0.91
68455	0.83	10.97	19.89	0.27	0.68
68467	1.13	11.19	20.00	0.36	0.48
68556	1.38	10.87	20.88	0.24	0.27
69478	1.31	11.01	21.17	0.17	0.59

69543	1.13	10.86	20.44	0.39	0.80
69607	1.30	10.93	21.06	0.26	0.61
69677	1.31	11.33	19.79	0.51	0.80
69805	0.95	10.80	20.72	0.27	0.57
69853	0.99	10.78	20.93	0.14	0.68
69909	1.41	11.08	20.74	0.12	0.78
69999	0.97	11.20	19.77	0.26	0.83
71156	1.15	10.71	21.16	0.10	0.70
71198	0.90	10.99	19.89	0.30	0.59
71220	1.25	11.53	20.36	0.30	0.44
71513	1.30	11.17	20.52	0.34	0.73
71689	1.36	11.38	19.71	1.16	0.60
72383	1.46	10.95	21.32	0.15	0.79
72767	1.36	10.70	21.34	0.29	0.92
72858	1.19	11.26	20.02	0.33	0.73
72949	0.68	11.00	19.44	0.37	0.80
72956	0.75	10.83	20.00	0.21	0.77
73022	0.69	11.45	19.04	0.40	0.58
73188	1.33	10.72	21.51	0.12	0.68
73205	0.78	10.89	19.65	0.32	0.50
73315	1.29	10.92	20.67	0.37	0.28
74091	1.43	11.06	20.81	0.15	0.38
74152	1.56	10.89	20.88	0.68	0.86
74239	0.68	11.58	18.18	1.10	0.73
74771	1.23	10.71	21.02	0.30	0.67
74984	1.33	11.00	20.63	0.31	0.33
75881	1.33	11.11	20.45	0.42	0.63
76554	0.69	11.10	19.10	0.64	0.22
76713	0.97	10.95	20.29	0.25	0.59
76870	1.14	10.70	21.02	0.15	0.50
76971	0.94	10.70	20.78	0.34	0.69
77163	1.60	11.05	21.08	0.22	0.77
77232	1.34	11.25	20.04	0.48	0.49
77787	1.52	10.87	20.68	0.72	0.79
78018	1.09	11.14	19.94	0.23	0.25
78136	0.75	10.75	20.02	0.35	0.85
78346	0.74	11.45	18.63	0.52	0.74
78536	0.71	10.79	19.21	0.94	0.58

List of Figures

List of Tables

ABBREVIATIONS

ΛCDM	Cold Dark Matter Model with Dark Energy
2MASS	Two Micron All Sky Survey
ACS	Advanced Camera for Surveys
AGB	Asymptotic Giant Branch
BPT	Baldwin, Phillips & Telervich
CANDELS	Cosmic Assembly Near-infrared Deep Extragalactic Legacy Survey
CMB	Cosmic Microwave Background
COBE	Cosmic Background Explorer
ECDFS	Extended Chandra Deep Field-South Survey
ESO	European Southern Observatory
FWHM	Full Width at Half Maximum
GALAPAGOS	Galaxy Analysis over Large Areas: Parameter Assessment by GALFITting Objects from SExtractor
GEMS	Galaxy Evolution from Morphologies and SEDs
GOODS-S	Great Observatories Origins Deep Survey-South
HAWK-I	High Acuity Wide field K-band Imager

HST	Hubble Space Telescope
IR	Infrared
ISM	Interstellar Medium
K-S	Kolmogorov-Smirnov
M-W	Mann-Whitney
MAGPHYS	Multi-wavelength Analysis of Galaxy Physical Propertie
NIR	Near Infrared
NYU-VAGC	New York University Value-Added Galaxy Catalog
PAH	Polycyclic Aromatic Hydrocarbon
PSF	Point Spread Function
SDSS	Sloan Digital Sky Survey
SED	Spectral Energy Distribution
SExtractor	Software for Source Extraction
SFR	Star Formation Rates
SNR	Signal-to-noise Ratio
sSFR	Specific Star Formation Rates
UDS	Ultra Deep Survey
VLT	Very Large Telescope
WFC3	Wide Field Camera 3
WISE	Wide-field Infrared Survey Explorer
WMAP	Wilkinson Microwave Anisotropy Probe

BIBLIOGRAPHY

Adelman-McCarthy, J. K., Agüeros, M. A., Allam, S. S., et al. 2008, ApJS, 175, 297
Alpher, R. A., & Herman, R. 1948, Nature, 162, 774
Ashby, M. L. N., Willner, S. P., Fazio, G. G., et al. 2013, ApJ, 769, 80
Baldwin, J. A., Phillips, M. M., & Terlevich, R. 1981, PASP, 93, 5
Barden, M., Häußler, B., Peng, C. Y., McIntosh, D. H., & Guo, Y. 2012, MNRAS, 422, 449
Bell, E. F. 2008, ApJ, 682, 355
Bell, E. F., Wolf, C., Meisenheimer, K., et al. 2004, ApJ, 608, 752
Bell, E. F., van der Wel, A., Papovich, C., et al. 2012, ApJ, 753, 167
Bennett, C. L., Halpern, M., Hinshaw, G., et al. 2003, ApJS, 148, 1
Benson, A. J., Džanović, D., Frenk, C. S., & Sharples, R. 2007, MNRAS, 379, 841
Bernardi, M., Roche, N., Shankar, F., & Sheth, R. K. 2011, MNRAS, 412, 684
Bertin, E., & Arnouts, S. 1996, A&AS, 117, 393
Bezanson, R., van Dokkum, P. G., Tal, T., et al. 2009, ApJ, 697, 1290
Binney, J. 1978, MNRAS, 183, 501
—. 1985, MNRAS, 212, 767
Blanton, M. R., Schlegel, D. J., Strauss, M. A., et al. 2005, AJ, 129, 2562
Bosma, A. 1978, PhD thesis, PhD Thesis, Groningen Univ., (1978)
Brammer, G. B., van Dokkum, P. G., & Coppi, P. 2008, ApJ, 686, 1503
Brammer, G. B., Whitaker, K. E., van Dokkum, P. G., et al. 2011, ApJ, 739, 24
Brinchmann, J., Charlot, S., White, S. D. M., et al. 2004, MNRAS, 351, 1151
Bruce, V. A., Dunlop, J. S., Cirasuolo, M., et al. 2012, MNRAS, 427, 1666
Bruzual, G., & Charlot, S. 2003, MNRAS, 344, 1000
Buitrago, F., Trujillo, I., Conselice, C. J., & Häußler, B. 2013, MNRAS, 428, 1460

Caon, N., Capaccioli, M., & D'Onofrio, M. 1993, MNRAS, 265, 1013
Cardamone, C. N., van Dokkum, P. G., Urry, C. M., et al. 2010, ApJS, 189, 270
Cassata, P., Giavalisco, M., Guo, Y., et al. 2011, ApJ, 743, 96
Cassata, P., Giavalisco, M., Williams, C. C., et al. 2013, ApJ, 775, 106
Ceverino, D., Dekel, A., & Bournaud, F. 2010, MNRAS, 404, 2151
Ceverino, D., Dekel, A., Mandelker, N., et al. 2012, MNRAS, 420, 3490
Chabrier, G. 2003, PASP, 115, 763
Chang, Y.-Y., van der Wel, A., Rix, H.-W., et al. 2013a, ApJ, 762, 83
—. 2013b, ApJ, 773, 149
Cheng, J. Y., Faber, S. M., Simard, L., et al. 2011, MNRAS, 412, 727
Chevance, M., Weijmans, A.-M., Damjanov, I., et al. 2012, ApJ, 754, L24
Copernicus, N. 1543, D revolutionibus orbium coelestium (Norimbergae, Apud J. Petreium, 1543; [Bruxelles, Culture et Civilisation, 1966])
da Cunha, E., Charlot, S., Dunne, L., Smith, D., & Rowlands, K. 2012, in IAU Symposium, Vol. 284, IAU Symposium, ed. R. J. Tuffs & C. C. Popescu, 292–296
da Cunha, E., Charlot, S., & Elbaz, D. 2008, MNRAS, 388, 1595
de Bernardis, P., Ade, P. A. R., Bock, J. J., et al. 2000, Nature, 404, 955
de Sitter, W. 1917, MNRAS, 78, 3
de Vaucouleurs, G. 1959, Handbuch der Physik, 53, 275
de Vaucouleurs, G. 1974, in IAU Symposium, Vol. 58, The Formation and Dynamics of Galaxies, ed. J. R. Shakeshaft, 1–52
Dekel, A., Sari, R., & Ceverino, D. 2009, ApJ, 703, 785
Dicke, R. H., Beringer, R., Kyhl, R. L., & Vane, A. B. 1946, Phys. Rev., 70, 340
Dressler, A. 1980, ApJ, 236, 351
Dreyer, J. L. E. 1888, MmRAS, 49, 1
—. 1895, MmRAS, 51, 185
—. 1910, MmRAS, 59, 105
Duncan, J. C. 1922, PASP, 34, 290
Einstein, A. 1916, Annalen der Physik, 354, 769
Emsellem, E., Cappellari, M., Krajnović, D., et al. 2011, MNRAS, 414, 888
Faber, S. M., Willmer, C. N. A., Wolf, C., et al. 2007, ApJ, 665, 265
Fall, S. M., & Efstathiou, G. 1980, MNRAS, 193, 189
Fall, S. M., & Frenk, C. S. 1983, AJ, 88, 1626
Franx, M., Illingworth, G., & de Zeeuw, T. 1991, ApJ, 383, 112
Friedmann, A. 1922, Zeitschrift fur Physik, 10, 377
Galametz, A., Grazian, A., Fontana, A., et al. 2013, ApJS, 206, 10
Galilei, G. 1610, Sidereus Nuncius. (Thomas Baglioni)
—. 1632, Dialogo DI Galileo Galilei Linceo matematico spraordinario dello stvdio DI Pisa. (Fiorenza, Per Gio: Batista Landini, 1632.)
Gamow, G. 1948, Nature, 162, 680

Giavalisco, M., Ferguson, H. C., Koekemoer, A. M., et al. 2004, ApJ, 600, L93
Graham, A. W., Erwin, P., Trujillo, I., & Asensio Ramos, A. 2003, AJ, 125, 2951
Grogin, N. A., Kocevski, D. D., Faber, S. M., et al. 2011, ApJS, 197, 35
Guo, Y., Giavalisco, M., Ferguson, H. C., Cassata, P., & Koekemoer, A. M. 2012, ApJ, 757, 120
Häussler, B., McIntosh, D. H., Barden, M., et al. 2007, ApJS, 172, 615
Herschel, J. F. W. 1864, Royal Society of London Philosophical Transactions Series I, 154, 1
Herschel, W. 1785, Royal Society of London Philosophical Transactions Series I, 75, 213
Hinshaw, G., Weiland, J. L., Hill, R. S., et al. 2009, ApJS, 180, 225
Holden, B. P., van der Wel, A., Rix, H.-W., & Franx, M. 2012, ApJ, 749, 96
Holden, B. P., Franx, M., Illingworth, G. D., et al. 2009, ApJ, 693, 617
Hopkins, P. F., Bundy, K., Hernquist, L., Wuyts, S., & Cox, T. J. 2010, MNRAS, 401, 1099
Hopkins, P. F., Cox, T. J., Kereš, D., & Hernquist, L. 2008, ApJS, 175, 390
Hubble, E. 1929, Proceedings of the National Academy of Science, 15, 168
—. 1936, The Realm of the Nebulae, 1st edn. (Yale University Press)
Hubble, E. P. 1925, ApJ, 62, 409
—. 1926, ApJ, 64, 321
Huertas-Company, M., Mei, S., Shankar, F., et al. 2013, MNRAS, 428, 1715
Jorgensen, I., & Franx, M. 1994, ApJ, 433, 553
Joseph, R. D., & Wright, G. S. 1985, MNRAS, 214, 87
Kauffmann, G., White, S. D. M., & Guiderdoni, B. 1993, MNRAS, 264, 201
Kauffmann, G., Heckman, T. M., White, S. D. M., et al. 2003a, MNRAS, 341, 33
Kauffmann, G., Heckman, T. M., Tremonti, C., et al. 2003b, MNRAS, 346, 1055
Kepler, J. 1609, Astronomia nova. ((Pragae) 1609)
Kewley, L. J., Dopita, M. A., Sutherland, R. S., Heisler, C. A., & Trevena, J. 2001, ApJ, 556, 121
Kewley, L. J., Groves, B., Kauffmann, G., & Heckman, T. 2006, MNRAS, 372, 961
Khochfar, S., & Silk, J. 2006a, ApJ, 648, L21
—. 2006b, MNRAS, 370, 902
Kimm, T., & Yi, S. K. 2007, ApJ, 670, 1048
Koekemoer, A. M., Faber, S. M., Ferguson, H. C., et al. 2011, ApJS, 197, 36
Kormendy, J. 1979, ApJ, 227, 714
Kormendy, J., & Bender, R. 1996, ApJ, 464, L119
Kormendy, J., & Djorgovski, S. 1989, ARA&A, 27, 235
Krajnović, D., Bacon, R., Cappellari, M., et al. 2008, MNRAS, 390, 93
Kriek, M., van Dokkum, P. G., Labbé, I., et al. 2009, ApJ, 700, 221
Lambas, D. G., Maddox, S. J., & Loveday, J. 1992, MNRAS, 258, 404

Lawrence, A., Warren, S. J., Almaini, O., et al. 2007, MNRAS, 379, 1599
Leavitt, H. S. 1908, Annals of Harvard College Observatory, 60, 87
Leavitt, H. S., & Pickering, E. C. 1912, Harvard College Observatory Circular, 173, 1
Lee, J. C., Hwang, H. S., & Ko, J. 2013, ApJ, 774, 62
Lemaître, G. 1927, Annales de la Societe Scietifique de Bruxelles, 47, 49
Magnelli, B., Elbaz, D., Chary, R. R., et al. 2009, A&A, 496, 57
Man, A. W. S., Toft, S., Zirm, A. W., Wuyts, S., & van der Wel, A. 2012, ApJ, 744, 85
Mannucci, F., Cresci, G., Maiolino, R., Marconi, A., & Gnerucci, A. 2010, MNRAS, 408, 2115
Marinoni, C., Monaco, P., Giuricin, G., & Costantini, B. 1999, ApJ, 521, 50
Martig, M., Bournaud, F., Teyssier, R., & Dekel, A. 2009, ApJ, 707, 250
McGrath, E. J., Stockton, A., Canalizo, G., Iye, M., & Maihara, T. 2008, ApJ, 682, 303
McLure, R. J., Pearce, H. J., Dunlop, J. S., et al. 2013, MNRAS, 428, 1088
Méndez-Abreu, J., Simonneau, E., Aguerri, J. A. L., & Corsini, E. M. 2010, A&A, 521, A71
Messier, C. 1781, Catalogue des Nébuleuses & des amas d'Étoiles (Catalog of Nebulae and Star Clusters), Tech. rep.
Naab, T., Johansson, P. H., & Ostriker, J. P. 2009, ApJ, 699, L178
Newman, A. B., Ellis, R. S., Bundy, K., & Treu, T. 2012, ApJ, 746, 162
Newton, I. 1760, Philosophiae naturalis principia mathematica, vol. 1 - 4 (Colonia : A. Philibert; 548 p. ; in 8.; DCC.4.221 I through IV)
Opik, E. 1922, ApJ, 55, 406
Oser, L., Naab, T., Ostriker, J. P., & Johansson, P. H. 2012, ApJ, 744, 63
Padilla, N. D., & Strauss, M. A. 2008, MNRAS, 388, 1321
Padmanabhan, N., Schlegel, D. J., Finkbeiner, D. P., et al. 2008, ApJ, 674, 1217
Patel, S. G., Holden, B. P., Kelson, D. D., et al. 2012, ApJ, 748, L27
Patel, S. G., van Dokkum, P. G., Franx, M., et al. 2013, ApJ, 766, 15
Peng, C. Y., Ho, L. C., Impey, C. D., & Rix, H.-W. 2002, AJ, 124, 266
—. 2010a, AJ, 139, 2097
Peng, Y.-j., Lilly, S. J., Kovač, K., et al. 2010b, ApJ, 721, 193
Penzias, A. A., & Wilson, R. W. 1965, ApJ, 142, 419
Perlmutter, S., Aldering, G., Goldhaber, G., et al. 1999, ApJ, 517, 565
Press, W. H., & Schechter, P. 1974, ApJ, 187, 425
Riess, A. G., Filippenko, A. V., Challis, P., et al. 1998, AJ, 116, 1009
Rix, H.-W., & Zaritsky, D. 1995, ApJ, 447, 82
Rix, H.-W., Barden, M., Beckwith, S. V. W., et al. 2004, ApJS, 152, 163
Robaina, A. R., Bell, E. F., van der Wel, A., et al. 2010, ApJ, 719, 844
Rubin, V. C., Burstein, D., Ford, Jr., W. K., & Thonnard, N. 1985, ApJ, 289, 81
Rubin, V. C., Ford, W. K. J., & . Thonnard, N. 1980, ApJ, 238, 471
Rubin, V. C., Thonnard, N., & Ford, Jr., W. K. 1978, ApJ, 225, L107

Ryden, B. 1992, ApJ, 396, 445
Ryden, B. S. 1996a, ApJ, 461, 146
—. 1996b, ApJ, 471, 822
—. 2004, ApJ, 601, 214
Salim, S., Rich, R. M., Charlot, S., et al. 2007, ApJS, 173, 267
Sandage, A., Freeman, K. C., & Stokes, N. R. 1970, ApJ, 160, 831
Scheiner, J. 1899, ApJ, 9, 149
Schlafly, E. F., & Finkbeiner, D. P. 2011, ApJ, 737, 103
Schlafly, E. F., Finkbeiner, D. P., Schlegel, D. J., et al. 2010, ApJ, 725, 1175
Schlegel, D. J., Finkbeiner, D. P., & Davis, M. 1998, ApJ, 500, 525
Schweizer, F., Seitzer, P., Faber, S. M., et al. 1990, ApJ, 364, L33
Skrutskie, M. F., Cutri, R. M., Stiening, R., et al. 2006, AJ, 131, 1163
Slipher, V. M. 1913, Lowell Observatory Bulletin, 2, 56
—. 1915, Popular Astronomy, 23, 21
Smoot, G. F., Bennett, C. L., Kogut, A., et al. 1992, ApJ, 396, L1
Stark, A. A. 1977, ApJ, 213, 368
Steinmetz, M., & Navarro, J. F. 2002, New Astronomy, 7, 155
Stockton, A., McGrath, E., & Canalizo, G. 2006, ApJ, 650, 706
Stockton, A., McGrath, E., Canalizo, G., Iye, M., & Maihara, T. 2008, ApJ, 672, 146
Szomoru, D., Franx, M., Bouwens, R. J., et al. 2011, ApJ, 735, L22
Targett, T. A., Dunlop, J. S., McLure, R. J., et al. 2011, MNRAS, 412, 295
Taylor, E. N., Franx, M., van Dokkum, P. G., et al. 2009, ApJS, 183, 295
Toft, S., Franx, M., van Dokkum, P., et al. 2009, ApJ, 705, 255
Toft, S., van Dokkum, P., Franx, M., et al. 2007, ApJ, 671, 285
Toomre, A. 1977, ARA&A, 15, 437
Tremblay, B., & Merritt, D. 1995, AJ, 110, 1039
—. 1996, AJ, 111, 2243
Trujillo, I., Erwin, P., Asensio Ramos, A., & Graham, A. W. 2004, AJ, 127, 1917
Unterborn, C. T., & Ryden, B. S. 2008, ApJ, 687, 976
van den Bosch, F. C., Aquino, D., Yang, X., et al. 2008, MNRAS, 387, 79
van der Wel, A., Bell, E. F., Holden, B. P., Skibba, R. A., & Rix, H.-W. 2010, ApJ, 714, 1779
van der Wel, A., Bell, E. F., van den Bosch, F. C., Gallazzi, A., & Rix, H.-W. 2009a, ApJ, 698, 1232
van der Wel, A., Franx, M., Wuyts, S., et al. 2006, ApJ, 652, 97
van der Wel, A., Holden, B. P., Zirm, A. W., et al. 2008, ApJ, 688, 48
van der Wel, A., Rix, H.-W., Holden, B. P., Bell, E. F., & Robaina, A. R. 2009b, ApJ, 706, L120
van der Wel, A., & van der Marel, R. P. 2008, ApJ, 684, 260
van der Wel, A., Rix, H.-W., Wuyts, S., et al. 2011, ApJ, 730, 38

van der Wel, A., Bell, E. F., Häussler, B., et al. 2012, ApJS, 203, 24
van Dokkum, P. G., Franx, M., Kriek, M., et al. 2008, ApJ, 677, L5
Vincent, R. A., & Ryden, B. S. 2005, ApJ, 623, 137
Vulcani, B., Poggianti, B. M., Dressler, A., et al. 2011, MNRAS, 413, 921
Whitaker, K. E., Kriek, M., van Dokkum, P. G., et al. 2012, ApJ, 745, 179
Whitaker, K. E., Labbé, I., van Dokkum, P. G., et al. 2011, ApJ, 735, 86
White, S. D. M., & Rees, M. J. 1978, MNRAS, 183, 341
Williams, R. J., Quadri, R. F., Franx, M., van Dokkum, P., & Labbé, I. 2009, ApJ, 691, 1879
Windhorst, R. A., Cohen, S. H., Hathi, N. P., et al. 2011, ApJS, 193, 27
Wright, E. L., Eisenhardt, P. R. M., Mainzer, A. K., et al. 2010, AJ, 140, 1868
Wuyts, S., Labbé, I., Schreiber, N. M. F., et al. 2008, ApJ, 682, 985
Wuyts, S., Labbé, I., Franx, M., et al. 2007, ApJ, 655, 51
Wuyts, S., Förster Schreiber, N. M., van der Wel, A., et al. 2011a, ApJ, 742, 96
Wuyts, S., Förster Schreiber, N. M., Lutz, D., et al. 2011b, ApJ, 738, 106
Wuyts, S., Förster Schreiber, N. M., Genzel, R., et al. 2012, ApJ, 753, 114
Yuan, H. B., Liu, X. W., & Xiang, M. S. 2013, MNRAS, 430, 2188
Zirm, A. W., van der Wel, A., Franx, M., et al. 2007, ApJ, 656, 66
Zwicky, F. 1933, Helvetica Physica Acta, 6, 110

ACKNOWLEDGEMENTS

First of all, it is with great gratitude that I acknowledge the support of Hans-Walter Rix, who let me start my fantastic adventure in MPIA. He always gave important direction and showed much interest for my work. He also gave me many opportunities to train in different ways and encouraged me positively. His passion for astronomy and life inspired me to work delightfully all the time.

I am extremely grateful to Arjen van der Wel, who provided day-to-day supervision for me. His door was always open to discuss with me, even if I asked trivial questions and bothered him endlessly. He was always kind to give me advice, and replied to anything in a short time. His bright thoughts and talents pushed my work to a higher level. It was lucky and pleasant to have such a nice adviser.

I would like to thank Thorsten Lisker for being my thesis committee and giving useful suggestions. Many thanks for Hans-Walter and Eva Grebel for being the referees for my thesis, and Thorsten Lisker and Luca Amendola for being the examiners of my defense.

Thank a lot to Kasper Borello Schmidt for providing the MCKBS (Mauricio Cisternas + Kasper Borello Schmidt style) for the thesis, Michael Maseda for correcting my English writing and grammar of the thesis, and Karsten Dittrich, Ronald Läsker, and Alex Buedenbender for translating and helping my German abstract.

Throughout my work, I would like to acknowledge all the collaborators for my published papers: Arjen van der Wel, Hans-Walter Rix, Stijn Wuyts, Stefano Zibetti, Balasubramanian Ramkumar, Bradford Holden, Eric F. Bell, Elizabeth J. McGrath, Boris Häussler, Marco Barden, S. M. Faber, Mark Mozena, Henry C. Ferguson, Yicheng Guo, Audrey Galametz, Norman A. Grogin, Dale D. Kocevski, Anton M. Koekemoer, Kuang-Han Huang, Nimish P. Hathi, Jennifer Donley, and the CANDELS team. Many thanks for the help from Elisabete da Cunha to implement MAGPHYS for the last part of my thesis.

The life in MPIA was joyous because of my cool office mates: Tobias Albertsson, Simon Bihr, Jian Chang, Karsten Dittrich, Maren Mohler-Fischer, Thomas Gerner, Mathias Jaeger, Alex Karim, and Bernhard Sturm.

I would like to express my sincere gratitude to Christian Fendt for his contribution to IMPRS-HD. It is fun to be part of this lovely program with: Tobias Albertsson, Gabriele Cologna, Dario Colombo, Karsten Dittrich, Stephan Henke, Veselina Kalinova, Angelos Kaloviduris, Rahul Kannan, Lukas Konstandin, Ronald Läsker, Lei Liu, Nils Lippok, Gabriele Maier, Maren Mohler-Fischer, Sladjana Nikolic, Paola Pinilla Ortiz, Alberto Rorai, Trifon Trifonov, and Fredrik Windmark.

It was joyful to meet ELIXIR fellows time by time: Enrica Bellocchi, Mariana Cano, Caruana, Joseph Cazzoli, Jacopo Chevallard, Bernhard Dorner, Silvio Lorenzoni, Moein Mosleh, Camilla Pacifici, Rosdahl, Kasper Borello Schmidt, and Paulina Troncoso.

During the stay in MPIA, I would like to thank: Ingrid Apfel, Ina Beckmann, Uli Hiller, Thu Huong Witte-Nguy, Marco Piroth, Heide Seifert, and Frank Witzel.

Special thanks for the support from Wen-Te Liao, who made my life in Heidelberg colorful and cheerful. Many thanks for his patience and encouragement at all times.

Last but not least, I would like to thank my dear Mom, Jen-Ni Chang. I receive maximum and wonderful support from her every moment and her only rule for me is: be happy. She is the best teacher, friend, sister, and mother. If I have any success, it is all because of her. Many thanks for my sister, Jing-Yu Tsou, who is always generous and happy to share good things and play with me since I was a baby. My deepest gratitude is for my dear Dad, Jian-San Tsou: we all love you forever.

Thank you all!!!